UNIVERSIDADE DE BRASILIA
INSTITUTO DE CIÊNCIAS HUMANAS
DEPARTAMENTO DE GEOGRAFIA
PROGRAMA DE PÓS-GRADUAÇÃO EM GEOGRAFIA

INTELIGÊNCIA ARTIFICIAL E SISTEMAS DE IRRIGAÇÃO POR PIVÔ CENTRAL: DESENVOLVIMENTO DE ESTRATÉGIAS E TÉCNICAS PARA O APRIMORAMENTO DO MAPEAMENTO AUTOMÁTICO

Tese de Doutorado

Anesmar Olino de Albuquerque

Brasília, fevereiro de 2022

UNIVERSIDADE DE BRASILIA
INSTITUTO DE CIÊNCIAS HUMANAS
DEPARTAMENTO DE GEOGRAFIA
PROGRAMA DE PÓS-GRADUAÇÃO EM GEOGRAFIA

INTELIGÊNCIA ARTIFICIAL E SISTEMAS DE IRRIGAÇÃO POR PIVÔ CENTRAL: DESENVOLVIMENTO DE ESTRATÉGIAS E TÉCNICAS PARA O APRIMORAMENTO DO MAPEAMENTO AUTOMÁTICO

Anesmar Olino de Albuquerque

Orientador: Prof. Dr. Osmar Abílio de Carvalho Júnior
Coorientador: Prof. Dr. Renato Fontes Guimarães

Tese de Doutorado

Brasília/DF, fevereiro de 2022

UNIVERSIDADE DE BRASILIA
INSTITUTO DE CIÊNCIAS HUMANAS
DEPARTAMENTO DE GEOGRAFIA
PROGRAMA DE PÓS-GRADUAÇÃO EM GEOGRAFIA

INTELIGÊNCIA ARTIFICIAL E SISTEMAS DE IRRIGAÇÃO POR PIVÔ CENTRAL: DESENVOLVIMENTO DE ESTRATÉGIAS E TÉCNICAS PARA O APRIMORAMENTO DO MAPEAMENTO AUTOMÁTICO

Anesmar Olino de Albuquerque

Tese de Doutorado submetida ao Departamento de Geografia da Universidade de Brasília, como parte dos requisitos necessários para a obtenção do Grau de Doutor em Geografia na área de concentração: Gestão Ambiental e Territorial

Aprovado por:

_____

Prof. Dr. Osmar Abílio de Carvalho Júnior (UnB)
(Orientador)

_____

Prof. Dr. Renato Fontes Guimarães (UnB)
(Coorientador)

_____

Prof. Dr. Yosio Edemir Shimabukuro (INPE)
(Membro Externo)

_____

Prof. Dr. Lineu Neiva Rodrigues (EMBRAPA)
(Membro Externo)

_____

Prof. Dr. Lindon Fonseca Matias (UNICAMP)
(Membro Externo)

_____

Prof. Dra. Potira Meirelles Hermuche (UnB)
(Suplente)

Brasília/DF, 11 de fevereiro de 2022

FICHA CATALOGRÁFICA

ALBUQUERQUE, ANESMAR OLINO DE.

Inteligência artificial e Sistemas de Irrigação por Pivô Central: desenvolvimento de estratégias e técnicas para o aprimoramento do mapeamento automático, 118p., (UnB-GEA, Gestão Ambiental e Territorial, 2022).

Tese de Doutorado – Universidade de Brasília. Departamento de Geografia.

1. Deep learning
2. Sensoriamento remoto
3. Convolutional neural network
4. Reconstrução de mosaicos

1. UnB-IH-GEA
II. Título (série)

REFERÊNCIA BIBLIOGRÁFICA

ALBUQUERQUE, A. O. **Inteligência artificial e Sistemas de Irrigação por Pivô Central: desenvolvimento de estratégias e técnicas para o aprimoramento do mapeamento automático**. 2020. 118p. Tese (Doutorado em Geografia) – Instituto de Ciências Humanas, Universidade de Brasília, Distrito Federal, 2022.

_____

Anesmar Olino de Albuquerque

DEDICATÓRIA

Dedico esse trabalho a minha querida mãe, a meus filhos e aos meus familiares

AGRADECIMENTOS

Agradeço primeiramente a Deus, pela minha vida e por me proporcionar incríveis oportunidades.

Aos meus pais, em especial a minha querida mãe, Guilhermina, que sempre foi minha maior inspiração, aos meus irmãos: Antônio, Célia e Selma, pelo carinho e aos meus filhos Maurício Padilha e Geovanna Acsa.

À Saiaka que, mesmo com as dificuldades de desenvolver seu próprio trabalho, sempre me incentivou e me ajudou de maneira especial.

Ao meu orientador, Prof. Dr. Osmar Abílio de Carvalho Júnior, que me motivou e me inspirou na proposta de *Deep Learning* e por ser um grande mestre. Agradeço imensamente pelos ensinamentos e por acreditar em mim.

Ao meu coorientador, Prof. Dr. Renato Fontes Guimarães, pelas contribuições diretas e indiretas, agradeço pela amizade e pela competência.

Ao Prof. Dr. Roberto Arnaldo Trancoso Gomes, que colaborou ao longo do trabalho e esclareceu diversas dúvidas, agradeço pela amizade e consideração.

Ao queridíssimo Osmar Luiz Ferreira de Carvalho, pela amizade construída e pelas incríveis trocas de conhecimento.

Aos amigos e amigas do Laboratório de Sistemas e Informações Espaciais – LSIE: Nathalia Costa, Hugo, Felipe Barbosa, Luciana, Maria, Diandra, Gabi, Núbia, Marcos, Ivo, Thiago, que de uma forma ou outra também puderam contribuir para a realização desse trabalho.

RESUMO

A irrigação é o principal responsável pelo aumento da produtividade dos cultivos. Os sistemas de irrigação por pivô central (SIPC) são líderes em irrigação mecanizada no Brasil, com expressivo crescimento nas últimas décadas e projeção de aumento de mais de 134% de área até 2040. O método mais utilizado para identificação de SIPC é baseado na interpretação visual e mapeamento manual das feições circulares, tornando a tarefa demorada e trabalhosa. Nesse contexto, métodos baseados em *Deep Learning* (DL) apresentam grande potencial na classificação de imagens de sensoriamento remoto, utilizando *Convolutional Neural Networks* (CNN's). O uso de DL provoca uma revolução na classificação de imagens, superando métodos tradicionais e alcançando maior precisão e eficiência, permitindo monitoramento regional e contínuo com baixo custo e agilidade. Essa pesquisa teve como objetivo aplicação de técnicas de DL utilizando algoritmos baseados em CNN's para identificação de SIPC em imagens de sensoriamento remoto. O presente trabalho foi dividido em três capítulos principais: (a) identificação de SIPC em imagens Landsat-8/OLI, utilizando segmentação semântica com três algoritmos de CNN (*U-Net, Deep ResUnet* e *SharpMask*); (b) detecção de SIPC usando segmentação de instâncias de imagens multitemporais Sentinel-1/SAR (duas polarizações, VV e VH) utilizando o algoritmo *Mask-RCNN*, com o *backbone* ResNeXt-101-32x8d; e (c) detecção de SIPC utilizando imagens multitemporais Sentinel-2/MSI com diferentes percentuais de nuvens e segmentação de instâncias utilizando *Mask-RCNN*, com o *backbone* ResNext-101. As etapas metodológicas foram distintas entre os capítulos e todas apresentaram altos valores de métricas e grande capacidade de detecção de SIPC. As classificações utilizando imagens Landsat-8/OLI, e os algoritmos *U-Net, Depp ResUnet e SharpMask* tiveram respectivamente 0,96, 0,95 e 0,92 de coeficientes Kappa. As classificações usando imagens Sentinel-1/SAR apresentaram melhores métricas na combinação das duas polarizações VV+VH (75%AP, 91%AP50 e 86%AP75). A classificação de imagens Sentinel-2/MSI com nuvens apresentou métricas no conjunto de 6 imagens sem nuvens (80%AP e 93%AP50) bem próximas aos valores do conjunto de imagens com cenário extremo de nuvens (74%AP e 88%AP50), demonstrando que a utilização de imagens multitemporais, aumenta o poder preditivo no aprendizado. Uma contribuição significativa da pesquisa foi a proposição de reconstrução de imagens de grandes áreas, utilizando o algoritmo de janela deslizante, permitindo várias sobreposições de imagens classificadas e uma melhor estimativa de pivô por pixel. O presente estudo possibilitou o estabelecimento de metodologia adequada para detecção automática de pivô central utilizando três tipos diferentes de imagens de sensoriamento remoto, que estão

disponíveis gratuitamente, além de um banco de dados com vetores de SIPC no Brasil Central.
Palavras – chave: *Deep learning*; *convolutional neural network*; sensoriamento remoto; reconstrução de mosaicos.

ABSTRACT

Irrigation is primarily responsible for increasing crop productivity. Center pivot irrigation systems (CPIS) are leaders in mechanized irrigation in Brazil, with significant growth in recent decades and a projected increase of more than 134% in area by 2040. The most used method for identifying CPIS is based on the interpretation visual and manual mapping of circular features, making the task time-consuming and laborious. In this context, methods based on Deep Learning (DL) have great potential in the classification of remote sensing images, using Convolutional Neural Networks (CNN's). The use of Deep Learning causes a revolution in image classification, surpassing traditional methods and achieving greater precision and efficiency, allowing regional and continuous monitoring with low cost and agility. This research aimed to apply DL techniques using algorithms based on CNN's to identify CIPS in remote sensing images. The present work was divided into three main chapters: (a) identification of CIPS in Landsat-8/OLI images, using semantic segmentation with three CNN algorithms (U-Net, Deep ResUnet and SharpMask); (b) CPIS detection using Sentinel-1/SAR multitemporal image instance segmentation (two polarizations, VV and VH) using the Mask-RCNN algorithm, with the ResNeXt-101-32x8d backbone; and (c) SIPC detection using Sentinel-2/MSI multitemporal images with different percentages of clouds and instance segmentation using Mask-RCNN, with the ResNext-101 backbone. The methodological steps were different between the chapters and all presented high metric values and great CPIS detection capacity. The classifications using Landsat-8/OLI images, and the U-Net, Depp ResUnet and SharpMask algorithms had respectively 0.96, 0.95 and 0.92 of Kappa coefficients. Classifications using Sentinel-1/SAR images showed better metrics in the combination of the two VV+VH polarizations (75%AP, 91%AP50 and 86%AP75). The classification of Sentinel-2/MSI images with clouds presented metrics in the set of 6 images without clouds (80%AP and 93%AP50) very close to the values of the set of images with extreme cloud scenario (74%AP and 88%AP50), demonstrating that the use of multitemporal images increases the predictive power in learning. A significant contribution of the research was the proposition of reconstruction of images of large areas, using the sliding window algorithm, allowing several overlaps of classified images and a better estimation of pivot per pixel. The present study made it possible to establish an adequate methodology for automatic center pivot detection using three different types of remote sensing images, which are freely available, in addition to a database with CPIS vectors in Central Brazil.

Keywords: Deep learning; convolutional neural networks; remote sensing; mosaic reconstruction.

Sumário

LISTA DE FIGURAS

LISTA DE TABELAS

LISTA DE ABREVIATURAS E SIGLAS

ANA. Agência Nacional de Águas e Saneamento Básico

AP. Aprendizagem Profunda

AP. Average Precision

AUC. Area Under the Curve

CBERS2B. China-Brazil Earth-Resources Satellite 2B

CCD. Couple Charged Device

CNN. Convolutional Neural Network

COCO. Commom Objects in COntext

CPIS. Center Pivot Irrigation System

CPU. Central Processing Unit

dB. Decibels

DL. Deep Learning

ESA. European Space Agency

FAIR. Facebook Artificial Intelligence Research

FN. False Negative

FP. False Positive

FPR. False Positive Rate

GB. GigaByte

GEOBIA. Geographic Object-Based Image Analysis

GHz. GigaHertz

GO. Goiás

GPU. Graphics Processing Units

GRD. Ground Range Detected

GT. Ground Truth

HT. Hough Transform

IEEE. Institute of Electrical and Electronic Engineers

IOU. Intersection Over Union

JSON. JavaScript Object Notation

Km. Quilômetro

LANDSAT. Land Satellite

MG. Minas Gerais

NDVI. Normalized Difference Vegetation Index

OLI. Operational Land Imager

ONU. Organização das Nações Unidas

R. Recall

RAM. Random Access Memory

RGB. Red, Green and Blue

RNC. Redes Neurais Convolucionais

ROC. Receiver Operating Characteristic curve

ROI. Region Of Interest

RPN. Region Proposal Network

P. Precision

SAR. Synthetic Aperture Radar

SIPC. Sistemas de Irrigação por Pivô Central

SRTM. Shuttle Radar Topography Mission

TA. Total Accuracy

TCI. True Color Image

TIFF. Tagged Image File Format

TM. Thematic Mapper

TN. True Negative

TP. True Positive

TPR. True Positive Rate

VH. Vertical transmitting, Horizontal receiving

VV. Vertical transmitting, Vertical receiving

CAPÍTULO

I. APRESENTAÇÃO

I.1 Introdução

Recentemente, a população mundial ultrapassou 7,7 bilhões de habitantes e as projeções indicam que até 2100, essa marca atinja 11,6 bilhões (ONU Department of Economic and Social Affairs., 2019), isso torna as estratégias de produção agrícola fundamentais para garantir a segurança alimentar (Godfray et al., 2010; Pollice et al., 2018; Tilman & Clark, 2015)

No setor agrícola, o aumento da produção deve estar associado ao uso de técnicas e tecnologias capazes de tornar o uso dos recursos hídricos na agricultura eficiente e assim garantir o desenvolvimento sustentável (Beltran-Pea et al., 2020; Foley et al., 2011; Siebert & Döll, 2010). Os sistemas de irrigação são tecnologias fundamentais na intensificação da produção agrícola, podendo melhorar o rendimento da maioria das culturas de 100% à 400% (Alexandridis et al., 2008).

O Sistema de Irrigação por Pivô Central (SIPC) é uma das técnicas mais avançadas de irrigação, com capacidade de distribuição uniforme de água e de diferentes tipos de fertilizantes, além disso, utilizam alto grau de automação dos processos e podem ser instalados em diferentes tipos de solos e em grandes áreas. As áreas irrigadas por SIPC no Brasil tiveram aumento significativo nas últimas décadas, saltando de 30.852 hectares em 1985, para 1,556 milhão de hectares em 2019, e as projeções indicam que em 2040 o país atinja 3,654 milhões de hectares, além disso, os estados de Minas Gerais, Goiás, Bahia e São Paulo concentram 76% desse total (ANA - Agência Nacional de Águas e Saneamento Básico, 2021).

O monitoramento de áreas irrigadas é crucial para o desenvolvimento de políticas públicas relacionadas a gestão dos recursos hídricos, entretanto, em áreas com dimensões continentais como o Brasil a sua realização se torna um grande desafio. Nesse sentido, o sensoriamento remoto surge como uma poderosa ferramenta pois permite que grandes áreas possam ser monitoradas com rapidez, periodicidade, custo-efetividade e com considerável confiabilidade dos dados.

Desde a década de 70 e 80 até atualmente, os estudos de monitoramento de sistemas de irrigação são baseados principalmente na interpretação visual de imagens de sensoriamento remoto, e as digitalizações de cada feição são realizadas manualmente (ANA - Agência

Nacional de Águas e Saneamento Básico, 2021; Ferreira et al., 2011; Rundquist et al., 1989; Sano et al., 2005; Schmidt et al., 2004). Esses estudos normalmente são demorados e apresentam alto custo, devido a necessidade de uma equipe de especialistas para vetorizarem as feições individualmente. Por conterem variados tipos de cultivos agrícola, com cores, texturas e resposta espectral distintas, os SIPC nem sempre tem um comportamento semelhante, o que dificulta sua identificação utilizando os métodos de classificação automática com base na resposta espectral de pixels ou índices de vegetação.

Um método muito utilizado para a detecção automática de círculos é o *Hough Transform* (HT) (Duda & Hart, 1972), nele, cada ponto de característica é transformado em um espaço de parâmetros tridimensional, uma imagem de contorno binária expressa por votação, a possibilidade de haver um círculo, com as informações de coordenadas (x, y) e do raio (r) do objeto, porém, o uso desse método em imagens de satélite apresenta precisão limitada e grande custo computacional (Chiu et al., 2010). Yanqing Wang et al. (2004), aplicaram o método para identificação automática de tanques de óleos circulares, e constatou que em imagens com mais complexidade do espaço paramétrico 3d, a tarefa se torna mais difícil e a identificação de semicírculos ou círculos irregulares se torna deficitária.

Os pivôs centrais apresentam feições bem características em imagens aéreas e de satélite. Os pivôs tem formas circulares, porém com características espectrais que podem variar dependendo do cultivo a ser explorado. Dessa forma, a utilização de métodos de inteligência artificial tem um grande potencial para esse alvo. Entretanto, a escolha do método é uma etapa crucial. Modelos clássicos como árvores de decisão, floresta randômicas ou vizinhos mais próximos tendem a ser muito limitados para esse alvo, uma vez que a análise é feita por pixel, um pixel por vez (Ma et al., 2019). Nesse contexto, as técnicas de *Deep Learning* (DL) juntamente com arquiteturas conhecidas como *Convolutional Neural Network* (CNN) ou redes neurais convolucionais, têm apresentado grande potencial para detecção automática em imagens, uma vez que o aprendizado considera diferentes níveis de abstrações em arquiteturas hierárquicas com inúmeras camadas ocultas (Guo et al., 2016). O DL permite o entendimento não só de pixels isolados, mas também de interações por processar recursos de baixo nível (cantos e bordas) e alto nível (cenas completas) em matrizes multidimensionais (Lecun et al., 2015). O DL é uma subárea da aprendizagem de máquina que utiliza algoritmos para processar dados com alto grau de complexidade, além disso, usa camadas de neurônios matemáticos para processar dados, onde a informação é processada e passada de uma camada para outra, com a saída da camada anterior fornecendo o dado de entrada para a próxima camada (Schmidhuber,

2015).

O DL promoveu avanços notáveis no campo da visão computacional e seus modelos são utilizados na solução de problemas em diversas áreas do conhecimento, como reconhecimento de padrões, reconhecimento de fala, processamento de linguagem natural, sistemas de recomendações, entre outras (Liu et al., 2017; Ma et al., 2019). As técnicas de DL tiveram extraordinário progresso na comunidade de sensoriamento remoto, especialmente a partir de 2014 (Cheng et al., 2020), e os modelos mais utilizados são baseados em arquiteturas de CNN's, que conduzem trabalhos em diversas aplicações, como: classificação de imagens (Scott et al., 2017; Zhan et al., 2017), detecção de objetos (Ammour et al., 2017; Dong & Lin, 2020; Yu et al., 2017), segmentação semântica (Saraiva et al., 2020; Wang et al., 2020; Zhao et al., 2017) e segmentação de instâncias (Carvalho et al., 2021; Mou et al., 2019; Su et al., 2019).

A segmentação semântica profunda é uma das tarefas de alto nível comumente utilizada para compreensão completa da cena, diferentemente da classificação de imagens, nela todas as partes do objeto interagem com mais precisão, de forma a identificar e agrupar os pixels da imagem que estão semanticamente juntos (Garcia-Garcia et al., 2017; Guo et al., 2016). A segmentação de instâncias é considerada uma etapa evolutiva da segmentação semântica, seu objetivo principal é representar objetos de uma mesma classe separados em diferentes instâncias, permitindo uma compreensão individualizada de cada objeto, além disso, o resultado do processamento são caixas delimitadoras e as máscaras de segmentação (Carvalho et al., 2021).

Zhang et al. (2018) foram precursores na utilização de CNN para detecção automática de SIPC, utilizando as bandas RGB (*Red, Green e Blue)* de imagens Landsat 5-TM do período de seca. O método utilizado identifica o centro do pivô baseado em variação, onde o pixel de menor valor é considerado o ponto central do SIPC, e a partir desse pixel, um quadrado de tamanho fixo pré-definido é aplicado para demarcação da área do pivô. Além de não identificar pivôs grandes, maiores que a área pré-definida, a área demarcada pode não necessariamente representar a área do pivô, uma vez que eles apresentam grande variação de tamanho.

I.2 Objetivos

A presente tese possui como objetivo geral propor um aprimoramento das técnicas de identificação de sistemas de irrigação por pivô central em áreas localizadas na região central do Brasil a partir de dados de sensoriamento remoto, utilizando classificação automática com técnicas de *Deep Learning*.

Os objetivos específicos desta tese estão elucidados separadamente por cada capítulo a

seguir:

Capítulo 2

- Avaliar técnicas de segmentação semântica profunda para detecção de SIPC utilizando imagens Landsat-8/OLI;

Capítulo 3

- Avaliar técnicas de segmentação de instâncias para detecção de SIPC utilizando séries temporais de imagens Sentinel-1/SAR;

Capítulo 4

- Avaliar técnicas de segmentação de instâncias para detecção de SIPC utilizando séries temporais de imagens Sentinel-2/MSI;

I.3 Estrutura da Tese

Este trabalho está subdividido em quatro capítulos baseados na identificação de SIPC utilizando *Deep Learning* com diferentes imagens e metodologias. Os capítulos 2, 3 e 4 são relativos a artigos científicos elaborados com o objetivo geral da tese, considerando algumas particularidades, como área de estudos, metodologia, resultados e conclusões.

No primeiro capítulo, é apresentado uma contextualização geral sobre do tema, utilização de dados de sensoriamento remoto, além do aprendizado profundo usando *Deep Learning*.

O artigo do capítulo 2, ***Deep Semantic Segmentation of Center Pivot Irrigation Systems from Remotely Sensed Data,*** foi publicado em 06 de julho de 2020 na revista *Remote Sensing* (MDPI), nele foram aplicadas técnicas de segmentação semântica profunda a partir de algoritmos baseados em CNN, utilizando imagens Landsat-8/OLI em dois períodos distintos, considerando a sazonalidade. Foram analisadas três arquiteturas de redes de *Deep Learning*, comumente utilizadas para detecção de objetos em sensoriamento remoto (*U-Net, Deep ResUnet e SharpMark*). Além disso, no capítulo foi apresentado uma técnica de janela deslizante para a classificação de imagens de grandes áreas.

O artigo do capítulo 3, ***Instance Segmentation of Center Pivot Irrigation Systems Using Multi-Temporal Sentinel-1 Sar Images,*** foi publicado em 06 de maio de 2021 na revista *Remote Sensing Applications: Society and Environment* (Elsevier), e foram aplicadas técnicas de segmentação de instâncias de imagens multitemporais do Radar de Abertura Sintética (SAR) Sentinel-1, para detecção automática de SIPC. O uso de imagens de radar supera limitações das imagens óticas, como a presença de nuvens e sombra.

Já o artigo do capítulo 4, ***Dealing with Clouds and Seasonal Changes for Center Pivot Irrigation Systems Detection Using Instance Segmentation in Sentinel-2 Time Series,*** foi publicado em 13 de agosto de 2021 na revista *Journal of Selected Topics in Applied Earth Observations and Remote Sensing* (IEEE), foi aplicado uma metodologia de identificação automática de SIPC em imagens óticas multitemporais (Sentinel-2/MSI) com diferentes percentuais de nuvens.

Referências

Alexandridis, T. K., Zalidis, G. C., & Silleos, N. G. (2008). Mapping irrigated area in Mediterranean basins using low cost satellite Earth Observation. *Computers and*

Electronics in Agriculture, *64*(2), 93–103. https://doi.org/10.1016/j.compag.2008.04.001

Ammour, N., Alhichri, H., Bazi, Y., Benjdira, B., Alajlan, N., & Zuair, M. (2017). Deep Learning Approach for Car Detection in UAV Imagery. *Remote Sensing*, *9*(4), 312. https://doi.org/10.3390/rs9040312

ANA - Agência Nacional de Águas e Saneamento Básico. (2021). Atlas Irrigação. Uso da água na agricultura irrigada. In *Agência Nacional de Águas e Saneamento Básico*.

Beltran-Pea, A., Rosa, L., & D'Odorico, P. (2020). Global food self-sufficiency in the 21st century under sustainable intensification of agriculture. *Environmental Research Letters*, *15*(9). https://doi.org/10.1088/1748-9326/ab9388

Cai, X., & Rosegrant, M. W. (2002). Global Water Demand and Supply Projections. *Water International*, *27*(2), 159–169. https://doi.org/10.1080/02508060208686989

Carvalho, O. L. F. de, de Carvalho Júnior, O. A., Albuquerque, A. O. de, Bem, P. P. de, Silva, C. R., Ferreira, P. H. G., Moura, R. dos S. de, Gomes, R. A. T., Guimarães, R. F., & Borges, D. L. (2021). Instance Segmentation for Large, Multi-Channel Remote Sensing Imagery Using Mask-RCNN and a Mosaicking Approach. *Remote Sensing*, *13*(1), 39. https://doi.org/10.3390/rs13010039

Cheng, G., Xie, X., Han, J., Guo, L., & Xia, G.-S. (2020). Remote Sensing Image Scene Classification Meets Deep Learning: Challenges, Methods, Benchmarks, and Opportunities. *IEEE Journal of Selected Topics in Applied Earth Observations and Remote Sensing*, *13*, 3735–3756. https://doi.org/10.1109/JSTARS.2020.3005403

CHIU, S.-H., LIAW, J.-J., & LIN, K.-H. (2010). A FAST RANDOMIZED HOUGH TRANSFORM FOR CIRCLE/CIRCULAR ARC RECOGNITION. *International Journal of Pattern Recognition and Artificial Intelligence*, *24*(03), 457–474. https://doi.org/10.1142/S0218001410007956

Dong, Z., & Lin, B. (2020). Learning a robust CNN-based rotation insensitive model for ship detection in VHR remote sensing images. *International Journal of Remote Sensing*, *41*(9), 3614–3626. https://doi.org/10.1080/01431161.2019.1706781

Duda, R. O., & Hart, P. E. (1972). Use of the Hough transformation to detect lines and curves in pictures. *Communications of the ACM*, *15*(1), 11–15. https://doi.org/10.1145/361237.361242

Fereres, E., & Soriano, M. A. (2006). Deficit irrigation for reducing agricultural water use. *Journal of Experimental Botany*, *58*(2), 147–159. https://doi.org/10.1093/jxb/erl165

Ferreira, E., Toledo, J. H. D. E., Dantas, A. A. A., & Pereira, R. M. (2011). Cadastral Maps of

Irrigated Areas By Center Pivots in the State of. *Engenharia Agrícola*, *31*(4), 771–780.

Foley, J. A., Ramankutty, N., Brauman, K. A., Cassidy, E. S., Gerber, J. S., Johnston, M., Mueller, N. D., O'Connell, C., Ray, D. K., West, P. C., Balzer, C., Bennett, E. M., Carpenter, S. R., Hill, J., Monfreda, C., Polasky, S., Rockström, J., Sheehan, J., Siebert, S., … Zaks, D. P. M. (2011). Solutions for a cultivated planet. *Nature*, *478*(7369), 337–342. https://doi.org/10.1038/nature10452

Garcia-Garcia, A., Orts-Escolano, S., Oprea, S., Villena-Martinez, V., & Garcia-Rodriguez, J. (2017). A Review on Deep Learning Techniques Applied to Semantic Segmentation. *ArXiv*, 1–23. http://arxiv.org/abs/1704.06857

Godfray, H. C. J., Beddington, J. R., Crute, I. R., Haddad, L., Lawrence, D., Muir, J. F., Pretty, J., Robinson, S., Thomas, S. M., & Toulmin, C. (2010). Food Security: The Challenge of Feeding 9 Billion People. *Science*, *327*(5967), 812–818. https://doi.org/10.1126/science.1185383

Guo, Y., Liu, Y., Oerlemans, A., Lao, S., Wu, S., & Lew, M. S. (2016). Deep learning for visual understanding: A review. *Neurocomputing*, *187*, 27–48. https://doi.org/10.1016/j.neucom.2015.09.116

Kopittke, P. M., Menzies, N. W., Wang, P., McKenna, B. A., & Lombi, E. (2019). Soil and the intensification of agriculture for global food security. *Environment International*, *132*(May), 105078. https://doi.org/10.1016/j.envint.2019.105078

Lecun, Y., Bengio, Y., & Hinton, G. (2015). Deep learning. *Nature*, *521*(7553), 436–444. https://doi.org/10.1038/nature14539

Liu, W., Wang, Z., Liu, X., Zeng, N., Liu, Y., & Alsaadi, F. E. (2017). A survey of deep neural network architectures and their applications. *Neurocomputing*, *234*, 11–26. https://doi.org/10.1016/j.neucom.2016.12.038

Ma, L., Liu, Y., Zhang, X., Ye, Y., Yin, G., & Johnson, B. A. (2019). Deep learning in remote sensing applications: A meta-analysis and review. *ISPRS Journal of Photogrammetry and Remote Sensing*, *152*(November 2018), 166–177. https://doi.org/10.1016/j.isprsjprs.2019.04.015

Mou, L., Bruzzone, L., & Zhu, X. X. (2019). Learning spectral-spatialoral features via a recurrent convolutional neural network for change detection in multispectral imagery. *IEEE Transactions on Geoscience and Remote Sensing*, *57*(2), 924–935. https://doi.org/10.1109/TGRS.2018.2863224

ONU Department of Economic and Social Affairs. (2019). World population prospects 2019.

In *World Population Prospects 2019: Highlights 2019 (ST/ESA/SER.A/423)*. (Issue 141). United Nations, Department of Economic and Social Affairs, Population Division. http://www.ncbi.nlm.nih.gov/pubmed/12283219

Pollice, F., Albanese, V., & Urso, G. (2018). Food Security: A Challenge for a Global Governance. In A. Isoni, M. Troisi, & M. Pierri (Eds.), *Food Diversity Between Rights, Duties and Autonomies* (pp. 217–227). Springer Cham. https://doi.org/10.1007/978-3-319-75196-2_13

Rundquist, D. C., Hoffman, R. O., Carlson, M. P., & Cook, A. E. (1989). Nebraska center-pivot inventory: An example of operational satellite remote sensing on a long-term basis. *Photogrammetric Engineering and Remote Sensing*, *55*(5 pt 1), 587–590.

Sano, E. E., Lima, J. E. F. W., Silva, E. M., & Oliveira, E. C. (2005). Estimativa da variação na demanda de água para irrigação por pivô-central no Distrito Federal entre 1992 e 2002. *Engenharia Agrícola*, *25*(2), 508–515. https://doi.org/10.1590/S0100-69162005000200025

Saraiva, M., Protas, É., Salgado, M., & Souza, C. (2020). Automatic Mapping of Center Pivot Irrigation Systems from Satellite Images Using Deep Learning. *Remote Sensing*, *12*(3), 558. https://doi.org/10.3390/rs12030558

Schmidhuber, J. (2015). Deep learning in neural networks: An overview. *Neural Networks*, *61*, 85–117. https://doi.org/10.1016/j.neunet.2014.09.003

Schmidt, W., Coelho, R. D., Jacomazzi, M. A., & Antunes, M. A. H. (2004). Distribuição espacial de pivôs centrais no Brasil: I - região sudeste. *Revista Brasileira de Engenharia Agrícola e Ambiental*, *8*(2–3), 330–333. https://doi.org/10.1590/S1415-43662004000200026

Scott, G. J., England, M. R., Starms, W. A., Marcum, R. A., & Davis, C. H. (2017). Training Deep Convolutional Neural Networks for Land–Cover Classification of High-Resolution Imagery. *IEEE Geoscience and Remote Sensing Letters*, *14*(4), 549–553. https://doi.org/10.1109/LGRS.2017.2657778

Siebert, S., & Döll, P. (2010). Quantifying blue and green virtual water contents in global crop production as well as potential production losses without irrigation. *Journal of Hydrology*, *384*(3–4), 198–217. https://doi.org/10.1016/j.jhydrol.2009.07.031

Su, H., Wei, S., Yan, M., Wang, C., Shi, J., & Zhang, X. (2019). Object Detection and Instance Segmentation in Remote Sensing Imagery Based on Precise Mask R-CNN. *IGARSS 2019 - 2019 IEEE International Geoscience and Remote Sensing Symposium*, 1454–1457.

https://doi.org/10.1109/IGARSS.2019.8898573

Tilman, D., & Clark, M. (2015). Food, Agriculture & the Environment: Can We Feed the World & Save the Earth? *Daedalus*, *144*(4), 8–23. https://doi.org/10.1162/DAED_a_00350

Wang, S., Chen, W., Xie, S. M., Azzari, G., & Lobell, D. B. (2020). Weakly supervised deep learning for segmentation of remote sensing imagery. *Remote Sensing*, *12*(2), 207. https://doi.org/10.3390/rs12020207

Yanqing Wang, Ming Tang, Tieniu Tan, & Xianqing Tai. (n.d.). Detection of Circular Oil Tanks Based on the Fusion of SAR and Optical Images. *Third International Conference on Image and Graphics (ICIG'04)*, 524–527. https://doi.org/10.1109/ICIG.2004.54

Yu, L., Wang, Z., Tian, S., Ye, F., Ding, J., & Kong, J. (2017). Convolutional Neural Networks for Water Body Extraction from Landsat Imagery. *International Journal of Computational Intelligence and Applications*, *16*(01), 1750001. https://doi.org/10.1142/S1469026817500018

Zhan, Y., Wang, J., Shi, J., Cheng, G., Yao, L., & Sun, W. (2017). Distinguishing Cloud and Snow in Satellite Images via Deep Convolutional Network. *IEEE Geoscience and Remote Sensing Letters*, *14*(10), 1785–1789. https://doi.org/10.1109/LGRS.2017.2735801

Zhang, C., Yue, P., Di, L., & Wu, Z. (2018). Automatic Identification of Center Pivot Irrigation Systems from Landsat Images Using Convolutional Neural Networks. *Agriculture*, *8*(10), 147. https://doi.org/10.3390/agriculture8100147

Zhao, W., Du, S., Wang, Q., & Emery, W. J. (2017). Contextually guided very-high-resolution imagery classification with semantic segments. *ISPRS Journal of Photogrammetry and Remote Sensing*, *132*, 48–60. https://doi.org/10.1016/j.isprsjprs.2017.08.011

CAPÍTULO

II. DEEP SEMANTIC SEGMENTATION OF CENTER PIVOT IRRIGATION SYSTEMS FROM REMOTELY SENSED DATA

Resumo

O sistema de irrigação por pivô central (SIPC) é uma técnica de irrigação moderna amplamente utilizada na agricultura de precisão devido a sua alta eficiência no consumo de água e baixo trabalho em comparação aos métodos tradicionais de irrigação. O SIPC é líder em irrigação mecanizada no Brasil, com previsão de crescimento para os próximos anos. Portanto, o mapeamento das áreas dos pivôs centrais é um fator estratégico para a estimativa da produção agrícola, garantindo a segurança alimentar, a gestão dos recursos hídricos e a preservação do meio ambiente. Nesse sentido, o processamento digital de imagens de satélite é a principal ferramenta que permite o monitoramento regional e contínuo com baixo custo e agilidade. No entanto, a detecção automática do SIPC usando imagens de sensoriamento remoto continua sendo um desafio e muitas pesquisas adotaram a interpretação visual. Embora o SIPC apresente uma forma circular consistente na paisagem, essas áreas podem ter uma alta variação interna com diferentes plantações que variam ao longo do tempo, o que é difícil apenas com o comportamento espectral. O *Deep Learning* usando *Convolutional Neural Networks* (CNNs) é uma abordagem emergente que provoca uma revolução na segmentação de imagens, superando os métodos tradicionais e alcançando maior precisão e eficiência. Esta pesquisa teve como objetivo avaliar o uso de segmentação semântica profunda do SIPC a partir de algoritmos baseados em CNN usando imagens de refletância de superfície Landsat-8 (sete bandas). A metodologia desenvolvida pode ser subdividida nas seguintes etapas: (a) Definição de três áreas de estudo com alta concentração de CPIS no Brasil Central; (b) aquisição de imagens Landsat-8 considerando as variações sazonais dos períodos de chuva e estiagem; (c) definição de conjuntos de dados SIPC contendo imagens Landsat e máscara de verdade do solo de 256x256 pixels; (d) treinamento usando três arquiteturas CNN (*U-net, Deep ResUnet e SharpMask*); (e) análise de precisão; e (f) reconstrução de imagem grande usando seis valores de passada (8, 16, 32, 64, 128 e 256). Os três métodos alcançaram resultados de última geração com uma ligeira prevalência de *U-net* sobre *Deep ResUnet e SharpMask* (0,96, 0,95 e 0,92 coeficientes *Kappa*, respectivamente). Uma novidade nesta pesquisa foi a análise de pixels sobrepostos na reconstrução de imagens grandes. Os valores de passada mais baixos tiveram melhorias quantificadas pela curva *Receiver Operating Characteristic* (curva ROC) e *Kappa*, e menos erros nas bordas do quadro também foram perceptíveis. As imagens sobrepostas melhoraram significativamente a precisão e reduziram o erro presente nas bordas dos quadros classificados. Além disso, obtivemos resultados de maior precisão no início da estação seca. O presente estudo possibilitou o estabelecimento de um banco de dados de imagens do pivô central e uma metodologia adequada para o mapeamento do pivô central no Brasil Central.

Palavras-chave: irrigação; aprendizagem profunda; *U-net; ResUnet; SharpMask*; Landsat-8

Artigo publicado na revista *Remote Sensing*, 2020. DOI: 10.3390/rs12132159

Abstract

The center pivot irrigation system (CPIS) is a modern irrigation technique widely used in precision agriculture due to its high efficiency in water consumption and low labor compared to traditional irrigation methods. The CPIS is a leader in mechanized irrigation in Brazil, with growth forecast for the coming years. Therefore, the mapping of center pivot areas is a strategic factor for the estimation of agricultural production, ensuring food security, water resources management, and environmental conservation. In this regard, digital processing of satellite images is the primary tool allowing regional and continuous monitoring with low costs and agility. However, the automatic detection of CPIS using remote sensing images remains a challenge, and much research has adopted visual interpretation. Although CPIS presents a consistent circular shape in the landscape, these areas can have a high internal variation with different plantations that vary over time, which is difficult with just the spectral behavior. Deep learning using convolutional neural networks (CNNs) is an emerging approach that provokes a revolution in image segmentation, surpassing traditional methods, and achieving higher accuracy and efficiency. This research aimed to evaluate the use of deep semantic segmentation of CPIS from CNN-based algorithms using Landsat-8 surface reflectance images (seven bands). The developed methodology can be subdivided into the following steps: (a) Definition of three study areas with a high concentration of CPIS in Central Brazil; (b) acquisition of Landsat-8 images considering the seasonal variations of the rain and drought periods; (c) definition of CPIS datasets containing Landsat images and ground truth mask of 256×256 pixels; (d) training using three CNN architectures (U-net, Deep ResUnet, and SharpMask); (e) accuracy analysis; and (f) large image reconstruction using six stride values (8, 16, 32, 64, 128, and 256). The three methods achieved state-of-the-art results with a slight prevalence of U-net over Deep ResUnet and SharpMask (0.96, 0.95, and 0.92 Kappa coefficients, respectively). A novelty in this research was the overlapping pixel analysis in the large image reconstruction. Lower stride values had improvements quantified by the Receiver Operating Characteristic curve (ROC curve) and Kappa, and fewer errors in the frame edges were also perceptible. The overlapping images significantly improved the accuracy and reduced the error present in the edges of the classified frames. Additionally, we obtained greater accuracy results during the beginning of the dry season. The present study enabled the establishment of a database of center pivot images and an adequate methodology for mapping the center pivot in central Brazil.

Keywords: irrigation; deep learning; U-net; ResUnet; SharpMask; Landsat-8.

II.1 Introduction

Irrigation is one of the leading technologies for increasing agricultural productivity, improving the yield of most crops by 100% to 400% [1]. Besides, irrigation promotes several benefits: Mitigation of the seasonal climatic factor and agricultural risk, agricultural expansion in arid and semi-arid regions, plantation diversity, a higher commercial value of products, reduction of unit production costs, stabilization of production and food prices, and improvement of the socio-economic conditions of farmers.

In recent years, Brazil has shown significant annual growth in the irrigated area mainly in the Cerrado region. The Cerrado biome contains the largest proportion of areas irrigated by center pivots within Brazilian territory, ranging from 85.2% in 1985 to 78.3% in 2017 [2]. The irrigation areas expand to regions with a higher water deficit, requiring attention from water resources management. Regarding some types of irrigation, research has been developed to map the center pivot irrigation system (CPIS), which covers extensive areas. In Brazil, CPIS is the leader among mechanized irrigation, containing an average increase of 85,000 ha per year in the last five years, 1,04,000 ha per year in the previous three years, and has the most significant number of water concessions with 30.1% of the total [3].

Therefore, irrigated agriculture increases food supply regularly throughout the year and ensures food security. However, irrigation is the largest consumer of anthropic water with values well above any other use, reaching 70% of the global annual water withdrawal from watercourses and groundwater [4,5]. Moreover, projections for global agricultural water demand in 2050 may represent the need for a 19% increase in irrigation [5]. Irrigated agriculture also has a considerable impact on the environment, such as erosion, pollution, soil salinization, and lowered groundwater tables, among others. Consequently, the continued population growth represents a challenge to adjust the demand for food production with the management of water resources and the protection of biodiversity [6,7]. Furthermore, the availability of freshwater in the irrigation sector is expected to decrease due to increasing competition with other multiple uses of water. Many surveys approach the problem of overexploitation of freshwater resources and the threat to food security [8–11]. An aggravating factor for the future scenario is the effect of climate change, which should demand an increase in the use of irrigation to maintain agricultural production [12,13].

Regional monitoring of irrigated areas with the acquisition of accurate information on their extent, spatial pattern, production, and productivity is essential to ensure food security, better water resources management, territorial planning, and economic development [14–16].

Davis et al. [17] point out that the reformulation of agricultural landscape configurations based on location and total water consumption would provide higher food production and better water use efficiency. Thus, remote sensing is a tool to monitor and plan spatiotemporal changes in crops, seeking to establish rules to minimize current and potential conflicts over water use. Mapping irrigated areas using remote sensing data has been extensively used since 1970–1980 [18,19]. Different remote sensing data have been applied for the detection of irrigated areas, including optical data [20–23], radar data [24–27], or the combined use of the two types of data [28–30]. However, most CPIS mappings use the visual interpretation of circular features [3,19,31–34]. Center pivots do not always have similar behavior and may contain different plantations, making classification based on the spectral response of pixels or vegetation indices difficult. Therefore, the consistent automatic detection of center pivots from remote sensing data remains a challenge, enabling greater speed and avoiding widespread labor consumption.

In this approach, a method that has great potential for automated detection is the deep semantic segmentation. Semantic segmentation belongs to the field of computer vision, being a high-level task that seeks a complete understanding of the scene, including information of the object category, location, and shape [35,36]. According to Guo et al. [37], there are differences between semantic segmentation and image classification, because they do not need to know in advance what are the concepts of visual Remote Sens. 2020, 12, 2159 3 of 25 objects. Semantic-level segmentation allows all parts of the object to interact more precisely, identifying and grouping the pixels of the image that are semantically together. The aggregation of different parts that make up a whole requires a deep semantic understanding [37].

Several traditional computer vision and machine learning techniques have been overcome by deep semantic segmentation, a method that achieves greater accuracy and efficiency. Deep learning is an emerging approach that belongs to a subfield of machine learning and seeks to learn high-level abstractions in data using hierarchical architectures [38]. Different types of digital image processing using deep learning have obtained relevant results, for example, image fusion, image registration, scene classification, object detection, land use and land cover classification, segmentation, and object-based image analysis [39]. Classifications of remote sensing images using deep learning produced superior results in different types of mapping: Land-use and land-cover classification [40–43], urban features [44–47], change detection [48–51], and cloud detection [52–55], among others.

In this approach, Zhang et al. [56] was a pioneer in the use of CNNs for automatic identification of CPIS. The research [56] presents the following steps: (a) Collection of Red-

Green-Blue (RGB) image training data with a size of 34 × 34 pixels for CPISs and non-CPISs, where each CPIS has 25 images with a small position difference to the central; (b) application of CNNs and identification of the center of each CPIS using a variation-based approach, where the pixel with the lowest variation value within the local area is detected as the central point; and (c) demarcation of CPIS using a fixed-size square in the center. However, the authors did not segment the entire field. Instead, they identified only the central point of CPIS. The square demarcated from the center of the CPIS has a predetermined size and is not necessarily in accordance with the circumference of the CPIS. The survey also did not consider the seasonal variation of the plantations.

Changes in dry and rainy seasons in the Cerrado biome cause a significant variation in the phenology of CPIS agricultural cultivation and the surrounding natural vegetation. Therefore, this research sought to consider these seasonal differences in recognition of CPIS patterns. Another critical issue analyzed is the process of reconstructing the entire image. In sizeable remote sensing images, the segmentation is made by a sliding window with a lateral overlay for later image reconstruction. However, there is a knowledge gap of the effects of different overlapping intervals on reconstructed image quality, which the study sought to analyze. To compare the results with other surveys, we used CNN architectures used in other investigations with satellite images, such as De Bem et al. [48] and Yi et al. [57].

The present research aimed to evaluate deep sematic segmentation techniques for CPIS detection in central Brazil using Landsat 8 images. In this regard, the study assessed the following factors: (a) Different environments in central Brazil and seasonal changes (drought and rain); (b) three models based on CNN architecture (U-net, Deep ResUnet, and SharpMask); and (c) image reconstruction considering different overlapping ranges between 256 × 256 frames.

II.2 Materials and Methods

The image processing included the following steps (**Figure II.1**): (a) Definition of three study areas with a high concentration of CPIS in central Brazil; (b) acquisition of Landsat-8 Operational Land Imager (OLI) images (30-m resolution) considering the seasonal variations of the rain and drought periods; (b) definition of CPIS datasets containing Landsat images and ground truth mask of 256×256 pixels; (c) training stage using three popular CNN architectures (U-net, Deep ResUnet, and SharpMask); (d) large image reconstruction using a sliding window

algorithm; (e) analysis of seasonal effects in the detection of CPIS; and (f) accuracy analysis.

In general, object detection is challenging in large remote sensing images, which requires the establishment of reasonable dimensions of the training sample to obtain performance in processing and memory management. The definition of the sample size must consider the characteristics of the object, such as the format, locations, and scales. Thus, a strategy for the classification of a large remote sensing image is to subdivide it into patches with the same size as the training samples and to use a sliding window algorithm with a determined stride (overlap interval between patches). In this context, the present research performs numerous stride length comparisons to identify the optimal parameters to image reconstruction for center-pivot mapping. In addition, the research assesses the effects of phenological variations of natural vegetation and plantations during the rainy and dry period in the CPIS detection process.

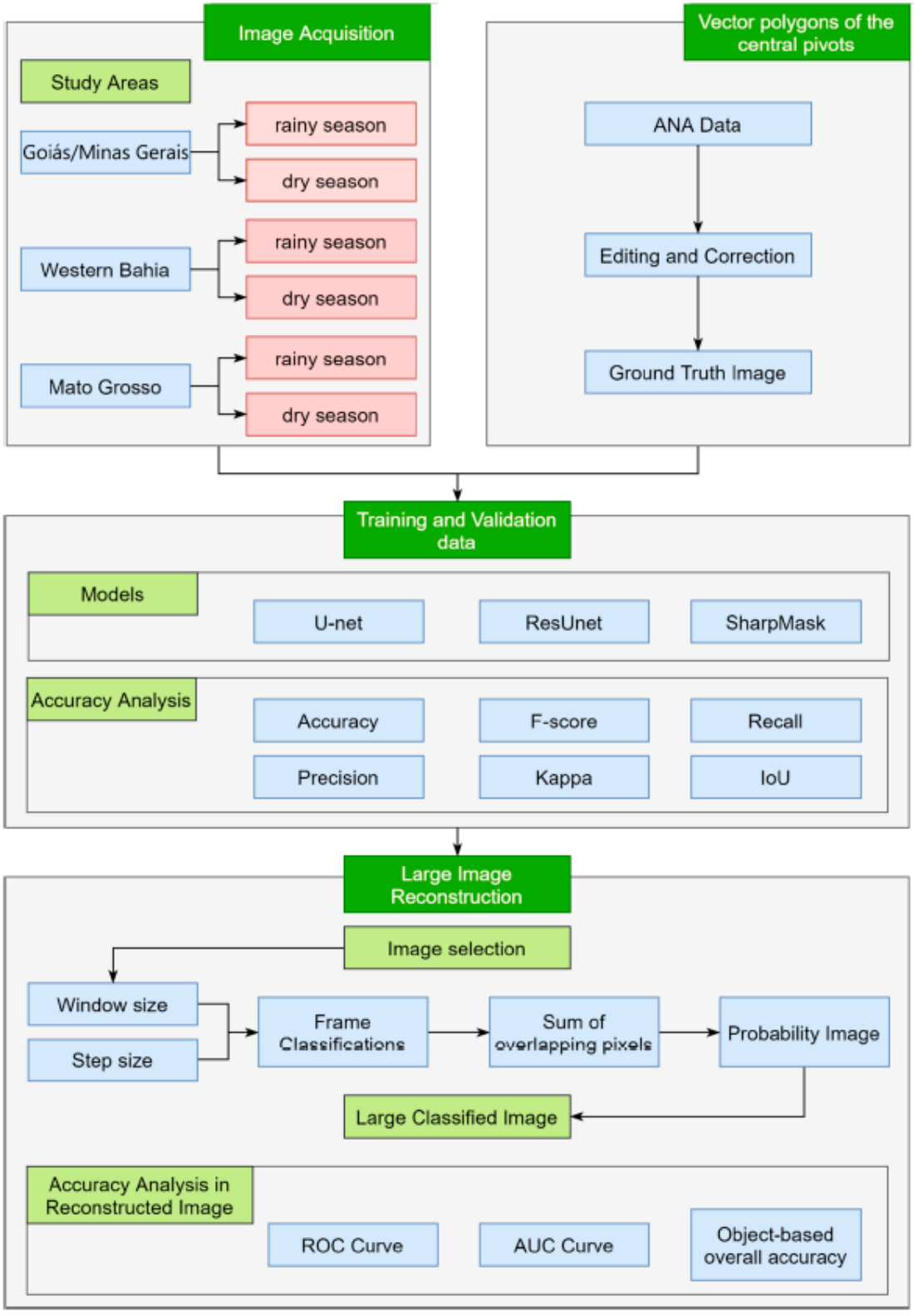

Figure II.1 Methodological flowchart of deep semantic segmentation of center pivots.

II.*2.1 Study Area*

The study sites cover three regions of central Brazil, presenting a high concentration of

center pivots favored by the flat terrain that allows mechanization: (a) Western Bahia (835 center pivots); (b) Goiás/Minas Gerais (2672 center pivots); and (c) Mato Grosso (224 center pivots) (**Figure II.2**). In these regions, water scarcity between May and September prevents the cultivation of several crops, requiring the need for additional irrigation water.

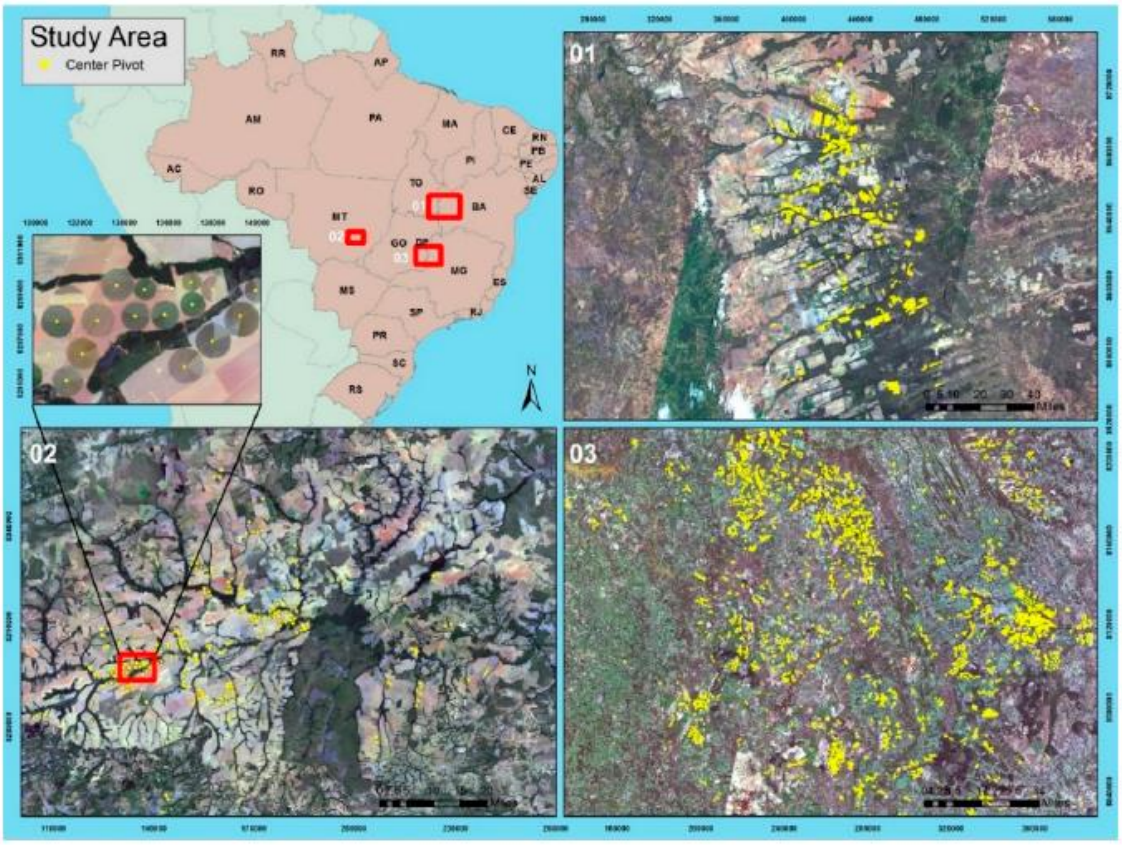

Figure II.2 Location map of the study areas: (1) Western Bahia; (2) Mato Grosso; and (3) Goiás/Minas.

The Western Bahia region with flat topography and water availability (from the rainfall, rivers, and groundwater) shows an increasing expansion of mechanized farming that replaced traditional agriculture [2,58–61] and an intensification of the implantation of center pivots [62]. Western Bahia had a significant increase in the irrigated area, ranging from 9 center pivots in 1985 to 1550 center pivots in 2016, which has caused water conflicts since 2010 [63].

The Goiás/Minas Gerais region has one of the highest concentrations of center pivots in Brazil, reaching the number of hundreds. In this region, there is a conflict over the use of water between the sectors of irrigated agriculture, human consumption, and hydroelectric power generation. Several types of research have already been carried out in the mapping of center pivot areas, analysis of areas suitable for the expansion of irrigation, demand for water for irrigation, and conflicts arising from competition for multiple water use [64–67].

The state of Mato Grosso has favorable environmental factors for agriculture, being one of the leading agricultural producers of soy and corn [68–71]. Besides, Mato Grosso had the most significant center pivot increase in the 2010–2017 period (175% growth), consolidating itself as an essential Brazilian irrigation center that still has considerable expansion potential [72].

II.*2.2 Dataset and Training Samples*

In deep learning techniques, extensive and qualified datasets are critical for object recognition success and meaningful performance comparisons between different algorithms. Satellite images allow the creation of extensive datasets in space and time that capture the vast richness and diversity of objects present on the land surface, which results in high-performance object recognition. The challenge is to establish a dataset contending the satellite images alongside with the corresponding ground truth image. The present research used data from the "Center Pivots in Brazil Irrigated Agriculture Survey," developed by the National Water Agency (ANA) [3], which contains all the vector data of the center-pivot polygons of the Brazilian territory in 2013/2014. The ANA survey extracted the vector polygons of CPIS from the visual interpretation of Landsat-8 OLI images. The preparation of ground truth images used this ANA database with some minor corrections when necessary.

For data compatibility with the ANA survey, we also used Landsat-8 surface reflectance images [73] from the same year 2014 or 2015 for the training and validation data. In central Brazil, the climate has well-defined rainy and dry seasons, with distinct phenological behaviors [74,75]. This climatic variability is responsible for differences within the same type of vegetation or planting, such as regeneration, vegetative growth, flowering, fruiting, and seed dispersal. Therefore, the image acquisition covered dry and rainy months with the different responses of vegetation and crop. **Table II.1** lists the set of images used in the three study areas. In the analyzed temporal images, we observed changes in the presence of center pivots in specific locations, even in short periods (**Figure II.3**). Thus, we checked and corrected the center pivot polygons to elaborate on the ground truth images.

This research considered two classes of interest (center pivots and non-pivots). The dataset had 5000 frames of each 256 × 256 pixel (4200 with center pivots and 800 without center pivots) with an 80%–20% train-test split (4000 frames for training and 1000 for validation). We evaluated three different neural network architectures (Deep ResUnet, U-net, and Sharpmask) with the following hyperparameter configurations: (a) 200 epoch training with

callbacks, (b) batch size of 8, (c) Adam optimizer, and (d) dice coefficient as the loss function. Additionally, each model's input layer was adjusted to support seven-channel Landsat images with 256 × 256 dimensions, resulting in a 256 × 256 × 7 input shape. For data processing, we used a computer equipped with a Nvidia GeForce RTX 2080 TI graphic card with 11 GB of GPU memory, 16 GB RAM, and an Intel Core i7–4770K CPU processor with a 3.5 GHz processing speed.

Table II-1 Landsat-8 Operational Terra Imager (OLI) images used in the training and validation stages.

Region	Date	Path/Row
Western Bahia	7 June 2014	220/068
Western Bahia	7 June 2014	220/069
Western Bahia	30 November 2014	220/068
Western Bahia	30 November 2014	220/069
Mato Grosso	10 June 2014	225/070
Mato Grosso	10 June 2014	225/071
Mato Grosso	16 November 2014	225/070
Mato Grosso	16 November 2014	225/071
Goiás/Minas Gerais	22 May 2014	220/071
Goiás/Minas Gerais	22 May 2014	220/072
Goiás/Minas Gerais	13 May 2014	221/071
Goiás/Minas Gerais	13 May 2014	221/072
Goiás/Minas Gerais	10 June 2015	220/071
Goiás/Minas Gerais	28 July 2015	220/072
Goiás/Minas Gerais	04 August 2015	221/071
Goiás/Minas Gerais	04 August 2015	221/072

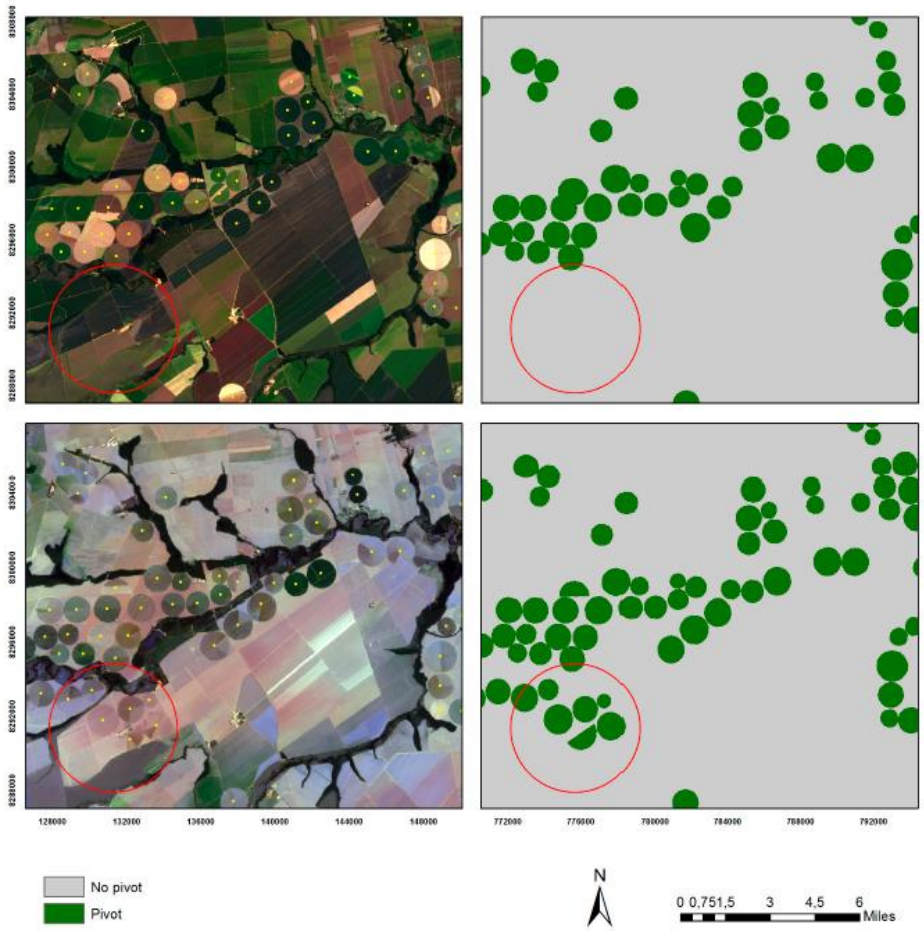

Figure II.3 Change of center pivots in short time, requiring adjustments and corrections in the database

for the elaboration of terrestrial truth images.

II.*2.3 Deep Learning Models*

In present research, we used three deep learning architectures: U-net [76], Deep ResUnet [77], and SharpMask [78]. U-net achieves significant results in the semantic segmentation, because of its ability to preserve essential features in the image, having two main parts: Contraction and expansion [76]. The name U-net comes from the symmetrical trajectory between both model parts (contraction and expansion) that describes a U-shape architecture. Thus, the U-net model has a series of kernels that act as filters that map specific features. The contraction (encoder) stage of the architecture consists of cascade downsampling, which reduces the image size and increasing the number of filters. The expansive (decoder) stage consists of a symmetrical number of up samples, returning the image to its original size, and decreasing the number of filters to the number of outputs. Each downsampling stage has two Conv2D layers, two batch normalization layers, and two ReLu activation functions, ending with the MaxPooling layer. The upsampling stage has the same format, but instead of the MaxPooling layer at the end, there is an upsampling layer at the beginning. There are five downsamples, which means the image gets to 1/32 of its original size, and five upsamples. The architecture ends with a sigmoid activation function. U-net has been used for the semantic segmentation of targets in remote sensing images: Road network [79], water body [80], building extraction [46,81], raft aquaculture areas [82], and edge-feature-based perceptual hash [83].

The deep residual U-Net (Deep ResUnet) combines the strengths of deep residual learning and the U-Net architecture [77] (https://github.com/nikhilroxtomar/Deep-Residual-Unet). The main advantages of the model are (a) replacement of plain neural units by residual units as a basic block, and (b) removal of cropping operation, allowing better performance because it is unnecessary. The architecture consists of encoder and decoder blocks. The decoder block has three sets of batch normalization, ReLu activation function, padding, and convolutional block. The encoder block has the same structure, but with strides, so the image is downsampled. The architecture ends with a sigmoid activation function. The Deep ResUnet and its variation have been investigated for satellite image segmentation [77,84,85].

Facebook's SharpMask is a network that enhances the sharpness of segmentation masks to object classification [78], which can be very satisfactory for our case, which deals with geometric objects. The architecture consists of convolutional and refinement blocks composed of three sets of Lambda, Conv2D, batch normalization, and ReLu activation functions. However, the refinement stage also adds activation functions. Every convolutional block is

connected to a MaxPooling layer, and every refinement block is connected to an upsampling layer. We performed four convolutional and refinement blocks that connect to a dense layer with 64 neurons and a ReLu activation function, and at the end, the sigmoid activation function. De Bem et al. [48] used SharpMask to detect changes in the Amazon region.

II.*2.4 Classified Image Reconstruction for Large Scenes*

We developed a sliding window with the same training image dimension that slides over the image for entire scene classification. Window movement can use different stride values in the horizontal and vertical directions. **Figure II.4** demonstrates the process of classifying large images from a sliding window. In the example, an 8 × 8 window slides over an image with a stride of two pixels. This process generates an overlap between consecutive frames considering stripe dimensions smaller than the window size (**Figure II.5**). Thus, a set of values may be produced for a pixel that can be used to improve target detection.

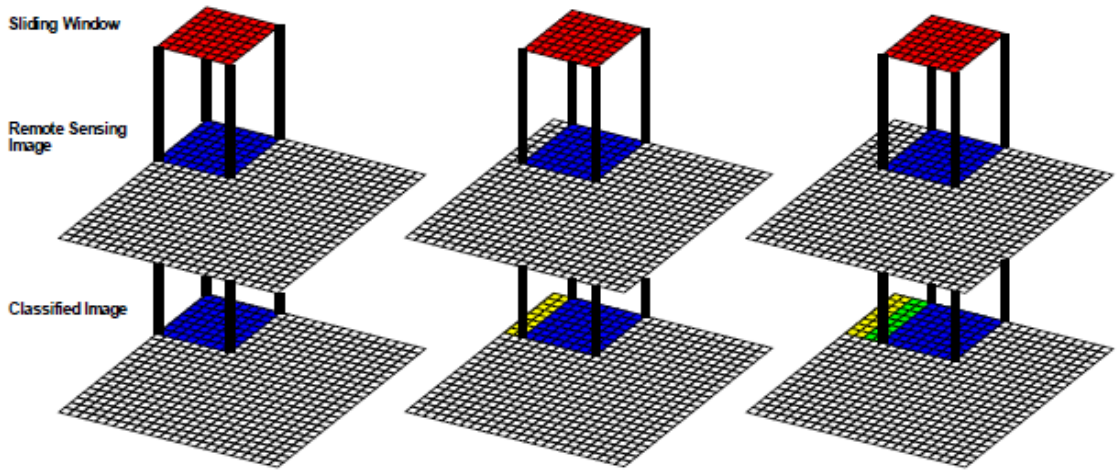

Figure II.4 Classification of large images based on their subdivision into frames. The method uses a sliding window that runs the image with a certain stride. In the example, the classification uses an 8x8 window that slides over an image with a two-pixel step.

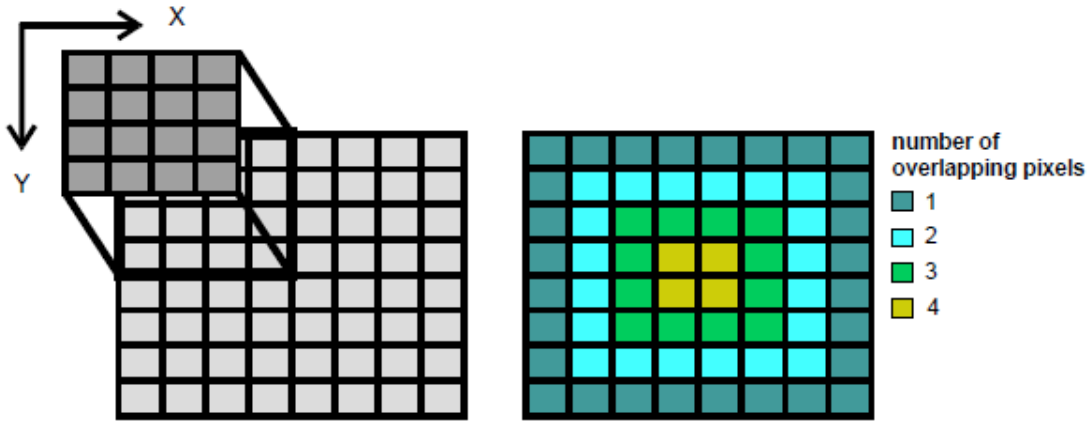

Figure II.5 Edge effect caused by window classification. The number of pixels at the edges of the large image is less than the center due to the smaller overlapping range.

The tests conducted in this research considered different stride values between two successive windows. Algorithms to reconstruct large images based on a sliding window with overlapping pixels were applied for remote sensing data. Previous studies used the average values of overlapping pixels to reduce the impact of frame boundaries, which tend to have more errors [48,57]. Instead of using the average, we established a proportionality index of the number of times the pixel was classified as a center pivot. Thus, we increased the pixel counter by one when the result value was greater than 0.7, which means a high probability of having a center pivot. In the end, for each pixel, we had a ratio of the number of times the method identified the pivot divided by the number of overlapping data, restricting the range of values between 0 and 1. The proportionality calculation considers the edge effect in the total image as necessary (**Figure II.5**). A threshold value defines the center pivot and non-center pivot binary image.

II.*2.5 Season Analysis*

The central Brazil region presents a substantial phenological variation throughout the year. In the Cerrado biome, water scarcity is the primary climatic determinant of leaf phenology, establishing the period to produce dry leaves and the sprouting of new leaves. The Cerrado vegetation has herbaceous and arboreal strata. Herbaceous plants lose their leaves in the dry season and produce new leaves at the beginning of the rains. Woody plants have different strategies, in which the brevideciduous and deciduous species completely lose their foliage during the dry period, and the evergreen species keep their leaves throughout the year. Besides, the stages of planting cycles also interfere with the detection of CPIS. Therefore, we chose images with different photosynthetic responses from water stress, as shown in **Table II.2** and

Figure II.6. The area analyzed was the Goiás/Minas Gerais region, which has the highest concentration of CPIS, encompassing three Landsat scenes. The image with the highest percentage of photosynthetic vegetation was from May 2019, representing the end of the rainy season (**Figure II.6A**). In contrast, the image from the critical dry period (August 2019) has a few areas with photosynthetically active vegetation, limited to some CPIS and riparian forest (**Figure II.6C**). Additionally, we added an image from the beginning of the dry season with intermediate behavior from June 2018 **(Figure II.6B**). One of the most considerable difficulties in obtaining rainy season imagery is the presence of clouds, especially when analyzing large areas

Table II-2 Landsat-8 OLI Operational Terra Imager images used to analyze different season behaviors.

Region	Date	Path/Row
Goiás/Minas Gerais	18 June 2018	220/071
Goiás/Minas Gerais	18 June 2018	220/072
Goiás/Minas Gerais	25 June 2018	221/071
Goiás/Minas Gerais	20 May 2019	221/071
Goiás/Minas Gerais	20 May 2019	220/072
Goiás/Minas Gerais	27 May 2019	221/071
Goiás/Minas Gerais	24 August 2019	220/071
Goiás/Minas Gerais	24 August 2019	220/072
Goiás/Minas Gerais	31 August 2019	221/071

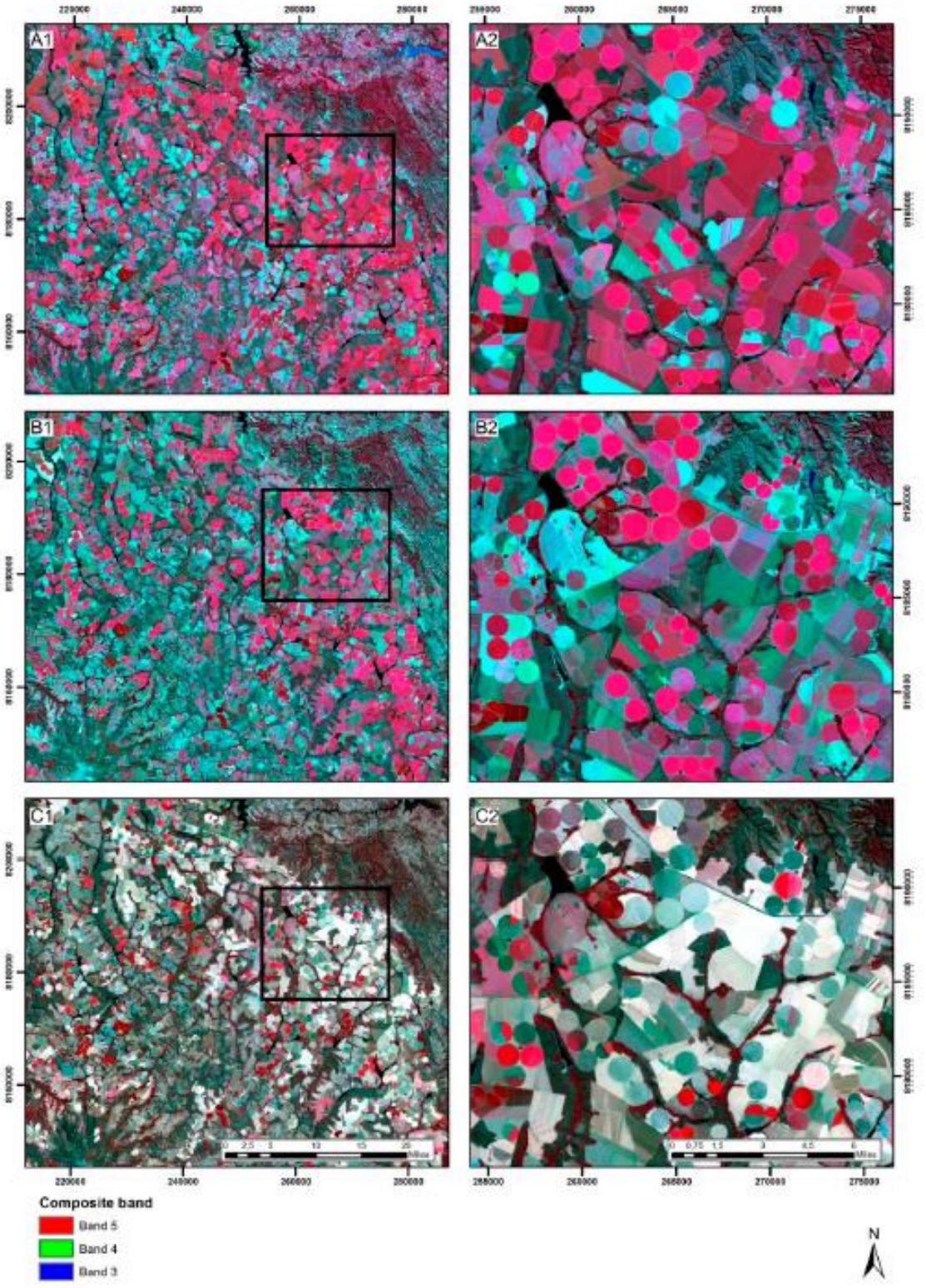

Figure II.6 Landsat images from the three different periods with different percentages of photosynthetic vegetation: (A1) rainy period (May 2019), (A2) zoomed image from the rainy period (B1) beginning of the dry period (June 2018), (B2) zoomed image from the begin of the dry period (June 2018), (B2) zoomed image from the beginning of the dry period (C1) critical dry season (August 2019), and (C2) zoomed image from the critical dry season. With the following composition, the red areas represent the photosynthetically active regions.

II.*2.6 Accuracy Assessment*

The accuracy analysis is crucial to establish the product quality and to compare classification algorithms. The accuracy assessment for the different methodological approaches adopted 1000 validation samples. We used the metrics commonly used for object detection: Total accuracy, precision, recall, F1, Kappa coefficient, and IoU [86,87,88,89,90]. **Table II.3** lists the equations for accuracy metrics. Besides, in the evaluation of the image reconstruction with different overlays, we used a new Landsat image (2018) and the ROC-curve analysis.

Table II-3 Summary of accuracy metrics used in the object detection, where TP is true positive, TN is true negative, FP is false positive, and FN is false negative.

Accuracy Metric	Equation
Total Accuracy (TA)	$\frac{TP+TN}{TP+FP+TN+FN}$
Precision (P)	$\frac{TP}{TP+FP}$
Recall (R)	$\frac{TP}{TP+FN}$
F1	$2 \times \frac{P \times R}{P+R}$
Kappa	$\frac{TA-p_e}{1-p_e}$, where $p_e = \frac{(TP+FN)*(TP+FP)+(FP+TN)*(FN+TN)}{(TP+FN+TF+FP)^2}$
IoU	$\frac{TP}{TN+FP+FN}$

Finally, we performed an object-based precision analysis to assess the correctness of the number of center pivots, crucial information for public managers [91,92].

II.3 Results

II.*3.1. Comparison between CNN architectures from the validation samples*

The training stage obtained low values for losses (< 0.05) and high values for Dice coefficients (> 0.99) for all the three methods, which was very satisfactory, demonstrating a high CPIS detection capacity. The CNN architecture efficiency is due to the great diversity of selected samples. This result indicates that all methods had an excellent ability to perform semantic segmentation for center pivots on multispectral data, considering different crops, shapes, and dimensions.

The accuracy scores had a pixel-wise analysis in the validation set (1000 images), totaling a pixel count of 65,536,000 (256×256×1000). The results demonstrated that the U-net had the best performance within the three networks (**Table II.4**, **Figure II.7**). Even though the results were very similar, the residual blocks present in Deep ResUnet did not improve the performance in comparison to U-net, probably because the target has a constant geometric

shape, varying only in size. Therefore, this result shows that simpler structures are sufficient for our analysis.

Table II-4 Quantitative comparison of accuracy metrics obtained from the segmentation results using Deep ResUnet, U-Net, and SharpMask, where the highest values for each metric are in bold.

	Accuracy	F-Score	Recall	Precision	Kappa	IoU
Deep ResUnet	0.9871	0.9610	**0.9484**	0.9739	0.9532	0.9249
U-net	**0.9880**	**0.9638**	0.9457	**0.9826**	**0.9638**	**0.9301**
SharpMask	0.97585	0.9342	0.9095	0.9603	0.9214	0.8765

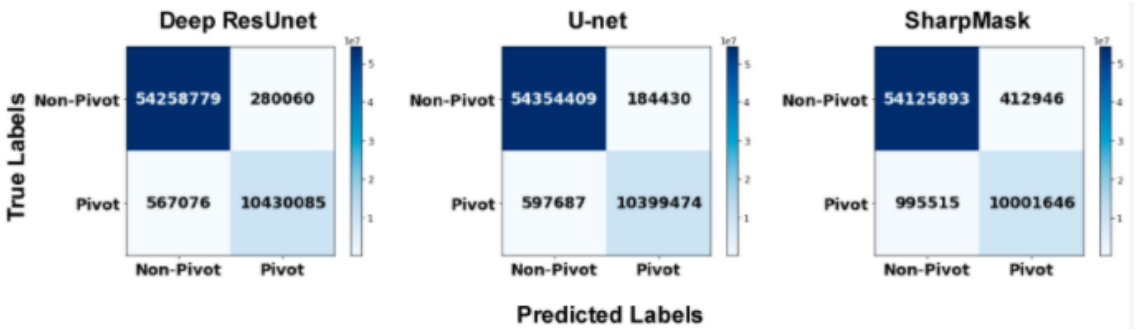

Figure II.7 Deep ResUnet, U-net, and SharpMask confusion matrices, considering a pixel-wise analysis.

II.3.2 Results of Entire Classified Image in Different Seasons

Segmentation within independent frames tends to have more errors at their edges [57]. Therefore, the image reconstruction from the classified frames with overlapping pixels can minimize these errors. To assess the overlap effect on the result, we selected our best model (U-net) and six different stride values (8, 16, 32, 64, 128, 256). This procedure used three independent Landsat images with 2560 × 2560-pixel dimensions from the Goiás/Minas Gerais region on 18 June 2018, 20 May 2019, and 24 August 2019. As expected, images with fewer overlapping pixels had a lot of errors at the frame edges, while increasing the number of overlapping pixels resulted in well-marked pivots, significantly minimizing errors.

The image reconstruction from the sliding windows with overlapping pixels had a significant improvement in classification (**Figure II.8**). The probability image became much closer to the ground truth image, with the stride value decreasing. Another interesting point is the precision of the method when analyzing the variety of spectral behaviors, texture, and internal arrangement within each center pivot.

These nuances are complicated even for human recognition, evidencing the importance and precision in the automatic classification of CPIS. Despite all the benefits with stride reduction, a considerable disadvantage of the overlapping windows technique is the longer processing time. Reducing the stride value by half on the x and y axes increased the classification time by four times. Image classification with no overlapping pixels is a fast task while using low stride values is a long process. The classification in a 2560 × 2560-pixel image

with no overlapping pixels took about 30 s to complete, while using a stride value of eight took about nine hours. **Figure II.8** shows the procedures to generate the classified binary image from the probability image.

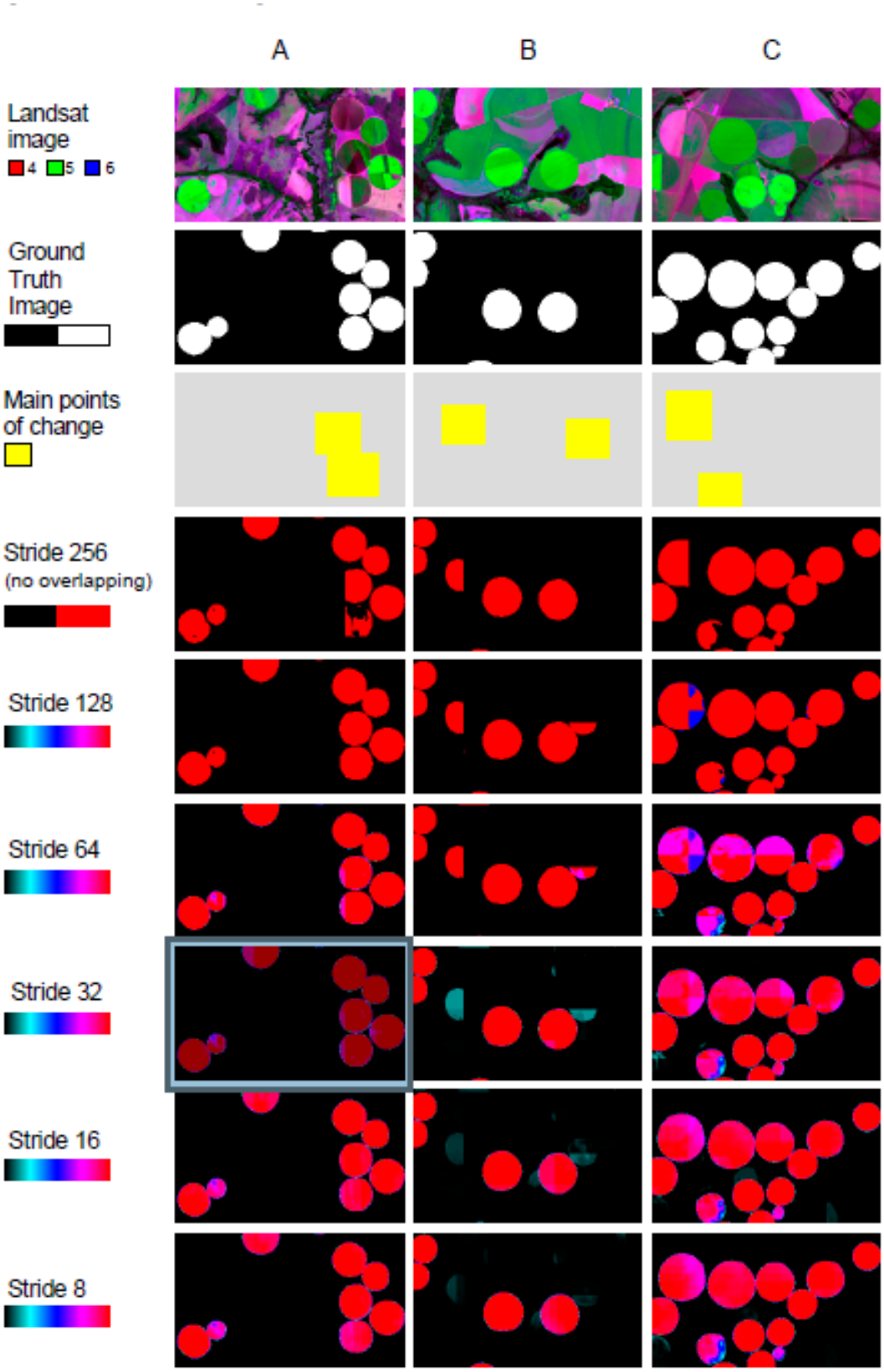

Figure II.8 Minimization of errors by increasing the sliding window overlap. Three examples of sub-images (A–C) represented by the following images: Landsat image, ground truth, the positions of the changes between the reconstructed images, and the result of the image reconstruction with stride values of 256, 128, 64, 32, 16 and 8.

We obtained the optimal threshold for CPIS detection by testing a succession of threshold values and chose the one with the greater Kappa coefficient when compared to its ground truth image [93]. These successive comparisons generated a graphical overview of Kappa's trajectory with threshold values from 0 to 1 (**Figure II.9A1,B1,C1**). This quantitative method reduces subjectivity in defining the optimal threshold value. The low optimal thresholds are due to the high selectivity of the index, weighing in favor of high activation pixels, and demonstrating a good likelihood to be a center pivot. The low threshold value reveals that the index produces a reduction of noisy points in the image, bringing a lower rate of false negatives.

To evaluate the different stride values in the three distinct dates, we used the receiving operating characteristic curve (ROC) in a pixel-wise analysis presented in **Figure II.10**. The ROC curve is a graphical representation of how well the model can differentiate two classes, by comparing two axes: (a) False positive rate (FPR) and (b) true positive rate (TPR). The closer to 1 in the area under the curve (AUC), the better the model performs. Additionally, the comparison of ROC curves from different periods is an interesting analysis because it shows how well the models can differentiate classes with different inputs. As expected, the areas with more significant photosynthetically active vegetation had better results (rainy and beginning of the dry season), while the critical dry period had weaker results. Stride value reduction increased the AUC scores in all three scenarios, achieving the highest value in the intermediate period (B) (0.984). In the rainy season (A), the results had a similar behavior compared to the intermediate period, with slightly lower values. The critical dry season (C) had the most different response since the reconstruction without overlapping pixels had significantly worse outcomes than the other two periods, but stride reduction significantly increased the ability to differentiate classes in a pixel-wise analysis.

The pixel-wise accuracy analysis presented similar results for the three dates. To make a better differentiation, we performed an object-based accuracy approach for the three Landsat images (2560 × 2560 pixels). This information is vital for public managers who seek to estimate the number of CPIS and evaluate the best scenarios to identify the center pivots. **Table II.5** lists the confusion matrix of the three dates. We identified: (a) 937 from 974 center pivots at the beginning of the dry season (96% OA); (b) 902 from 974 center pivots at the end of the rainy season (92% OA); and (c) 860 from 974 center pivots at the end of the dry season (88% OA). Even though the pixel-wise analysis had similar results, the object-based analysis shows a great difference within the three periods.

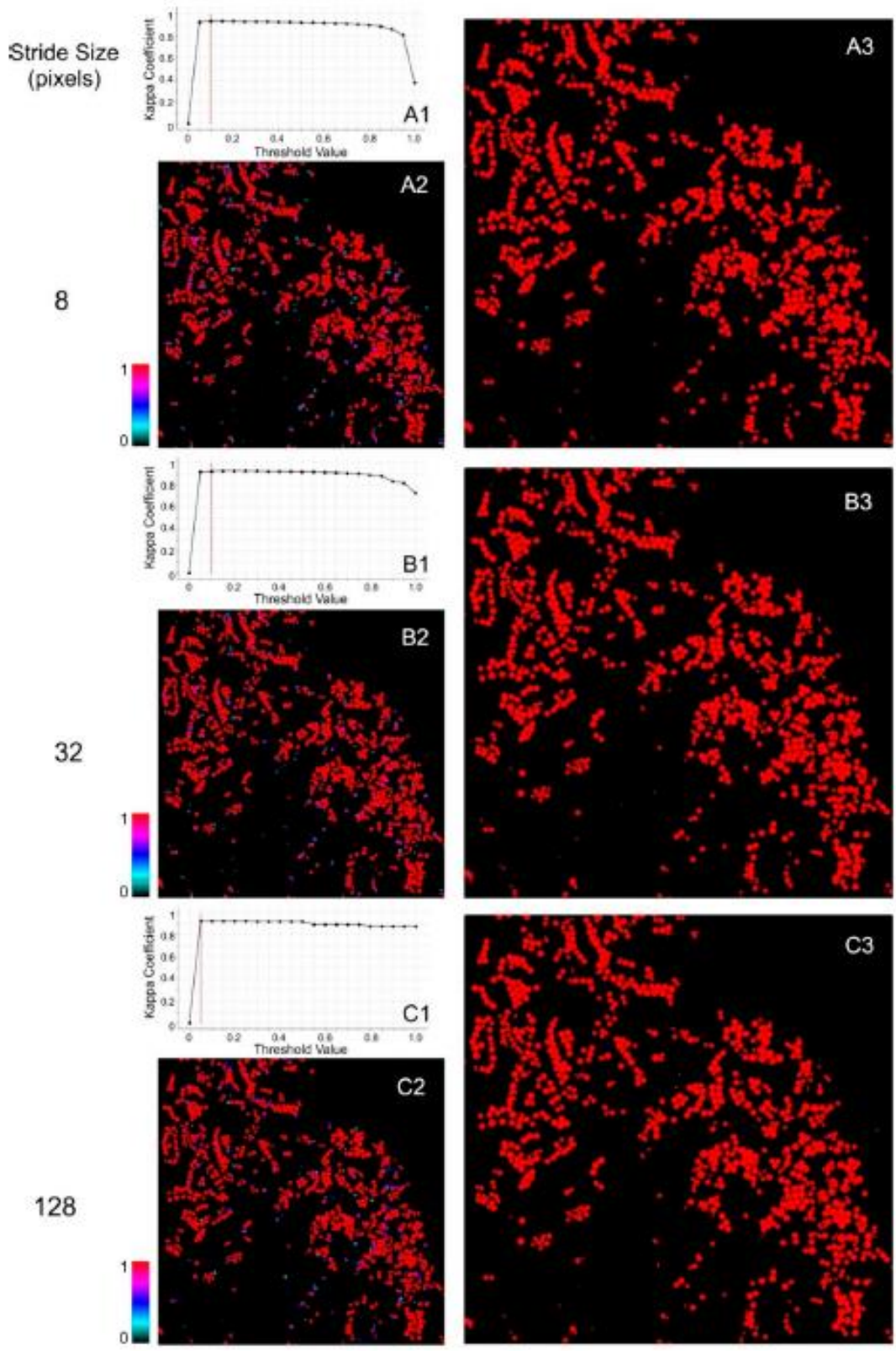

Figure II.9 Classification procedures from the sliding windows with strides 8 (A), 32 (B), and 128 (C), considering the following components: Graphs with the Kappa coefficients for the different threshold values, where the red line shows the optimum point (A1, A2, and A3), probability images (B1, B2, and B3), and binary images with center pivots (red) and non-pivot center (black) (A3, B3, and C3

images).

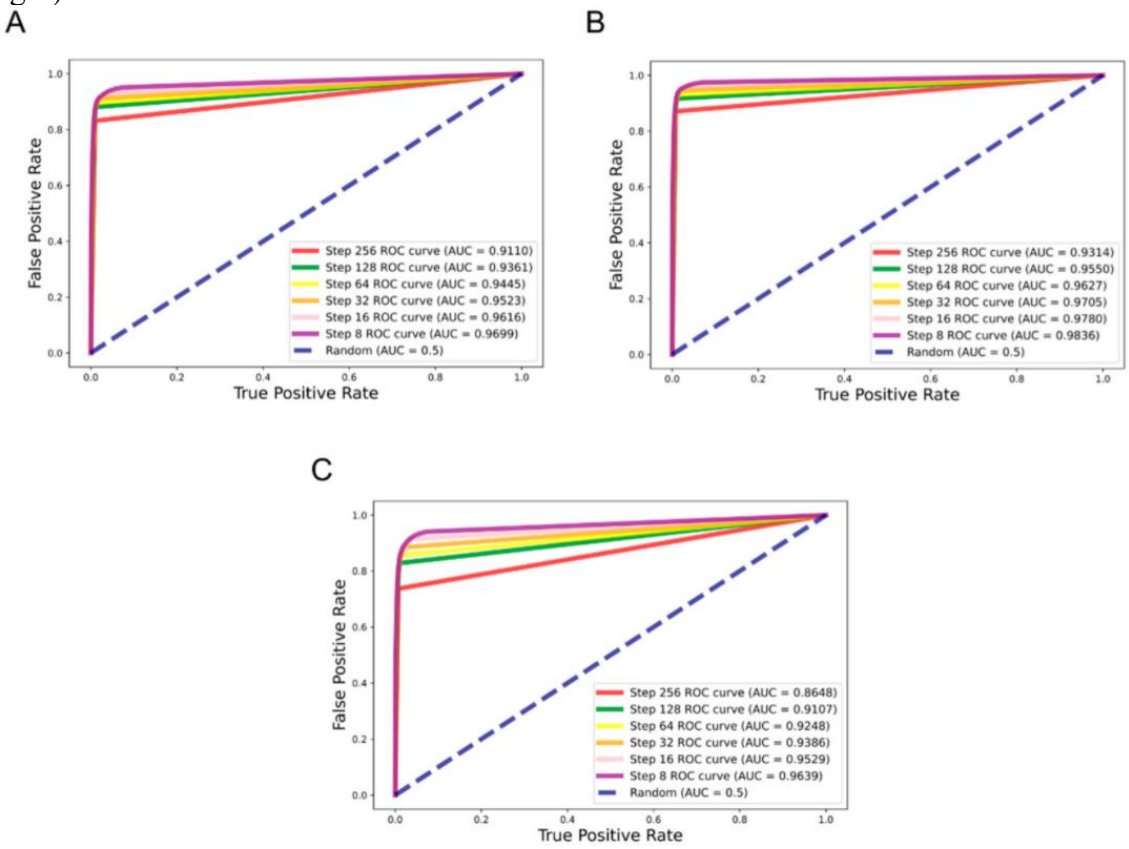

Figure II.10 Receiver Operating Characteristic Curve comparison of the large image reconstruction for: (A) the end of the rainy season (May 2019); (B) the beginning of the dry season (June 2018); and (C) the critical dry season (August 2019), using a sliding window (256 × 256) and U-net with different image overlapping areas (stride values of 8, 16, 32, 64, 128, and 256).

Table II-5 Confusion matrix containing the number correctly and incorrectly classified targets from the reconstructed image of the three periods using a stride of 8.

		Predicted Labels					
		Rainy Season (May 2019)		Beginning of the Dry Season (June 2018)		Critical Dry Period (August 2019)	
		Pivot	Non-Pivot	Pivot	Non-Pivot	Pivot	Non-Pivot
True Label	Pivot	902 (18 partially identified)	72	937 (25 partially identified)	37	860 (68 partially identified)	114
	Non-pivot	8	Does not apply	19 (total or pivot fractions)	Does not apply	2	Does not apply

Results from the beginning of the dry season had significantly better results than the rainy and critical dry period. Although the errors encountered in the classification of center pivots are due to their similarity with the surroundings, the source of the error is different. In the rainy season, the vegetation's photosynthetically active areas became very similar to the center pivots that have crop development. In contrast, in the critical dry period, harvesting associated with the conservation tillage practice in reducing runoff and erosion has a similar reflectance with the dry vegetation. **Figure II.11** shows zoomed areas from the Goiás/Minas

Gerais region within the three different dates showing areas that had correct classifications only in the beginning of the dry period. In the rainy season, the red color associated with the photosynthetically active vegetation shows that the center pivot and its surroundings had similar spectral behaviors. Likewise, in the critical dry period, non-photosynthetically active vegetation takes on a white color, homogenizing the CPIS with adjacent areas.

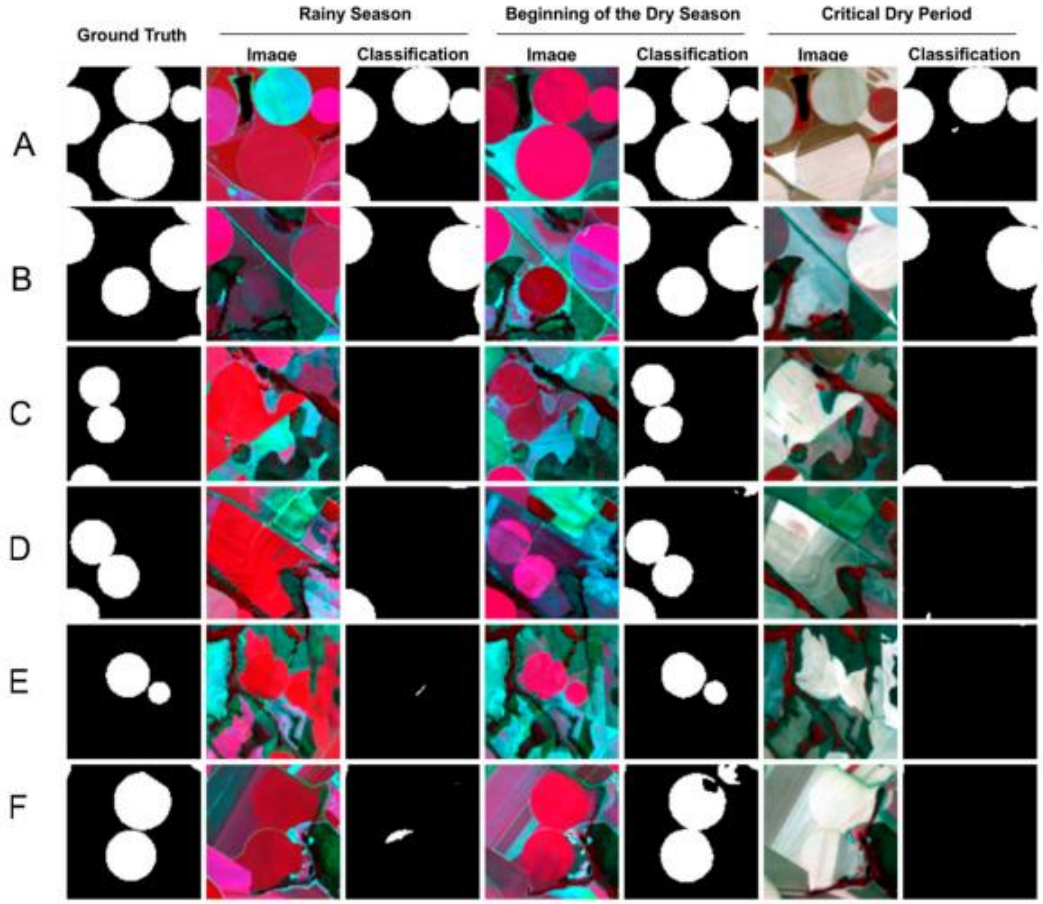

Figure II.11 Comparison of zoomed areas (A–F) at different times of the year (rainy season, early dry, and critical dry seasons). The examples demonstrate that only images from the beginning of the dry season detect the center pivots.

Figure II.12 shows locations where only the images of the beginning of the dry season detected CPIS. The photosynthetically active vegetation is now gone, and the center pivots have very similar behavior with its dry surrounding. Additionally, this kind of error is much more common than rainy season errors. The present research shows that the identification in the intermediate season is optimal since it has the advantage of photosynthetically active regions inside the pivots, but without the similarity with the vegetation surroundings.

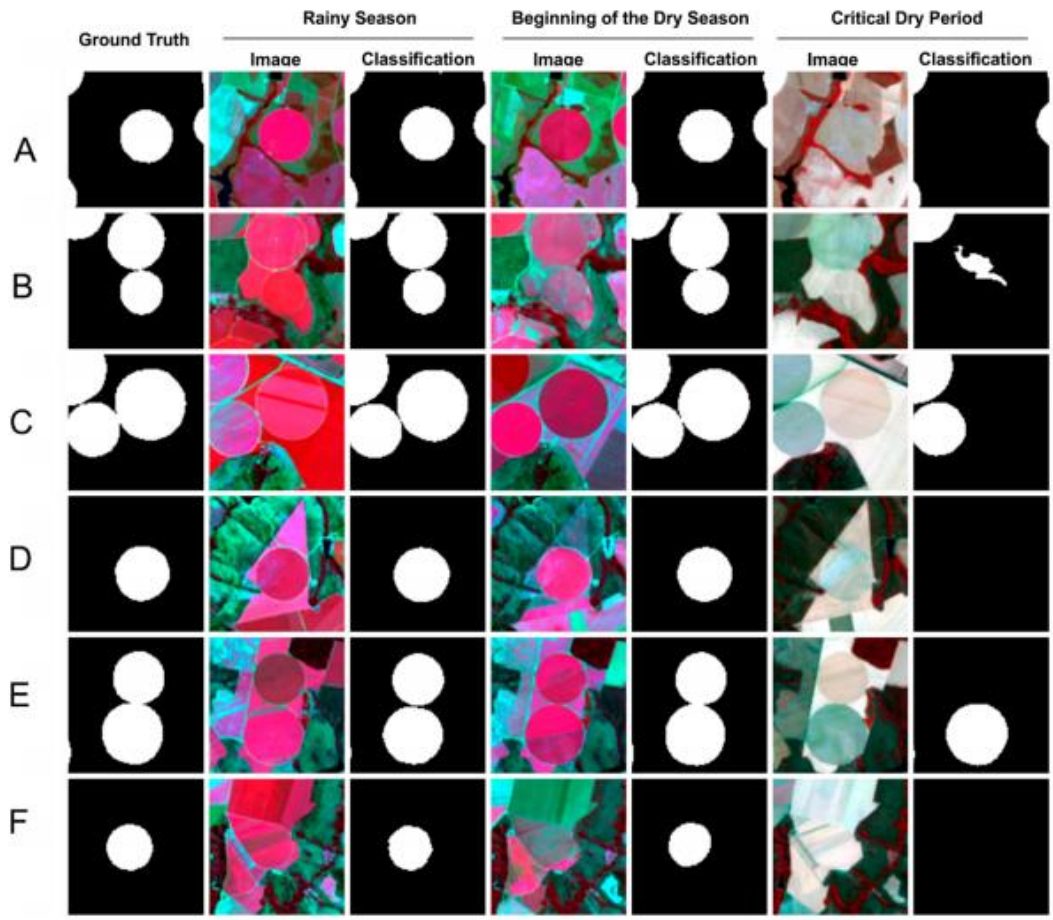

Figure II.12 Comparison of zoomed areas (A–F) at different times of the year (rainy, early dry, and critical dry seasons). The examples demonstrate that the images from the rainy season and the beginning of the dry season detect the center pivots.

Figure II.13 shows a rare situation where only the center pivots present in the rainy season image were correctly identified. The pattern of non-recognition was the same as the previous ones, having very similar environments around it. Figure 13B also presents a center pivot that was not identified in any of the periods. **Figure II.14** shows that most center pivots classified as false positives had significant similarities with the class of interest, being a controversial detection task even to specialized professionals. **Figures II.14A, B, and C** present a possible case of abandoned center pivots, due to the lack of planting area within the circular shape. **Figure II.14D** illustrates a polygon that was erroneously mapped but has a similar center pivot shape. We can observe that even the errors obtained from the predictions are very hard to determine, ensuring state-of-the-art results to this classification problem. Besides, the error images (**Figure II.12**) also demonstrate an increase in errors along the circumference of the CPIS, being a predictable result, since the manual classification hardly achieves

standardization, such as automatic classification. Therefore, this type of effect should not be considered an incorrect classification.

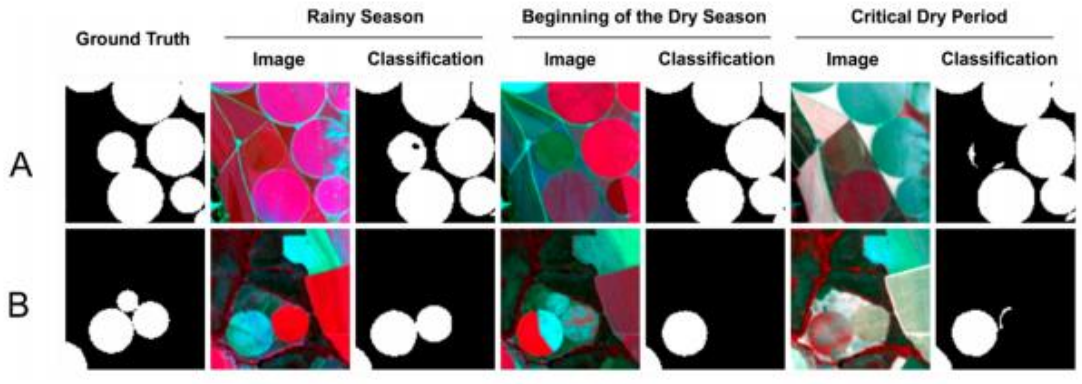

Figure II.13 Comparison of zoomed areas at different times of the year (rainy, early dry, and critical dry seasons). (A) Only the classified image from the rainy season detects the center pivots. (B)) The image contains three pivots where the rainy season classification detects two, while the others detect only one.

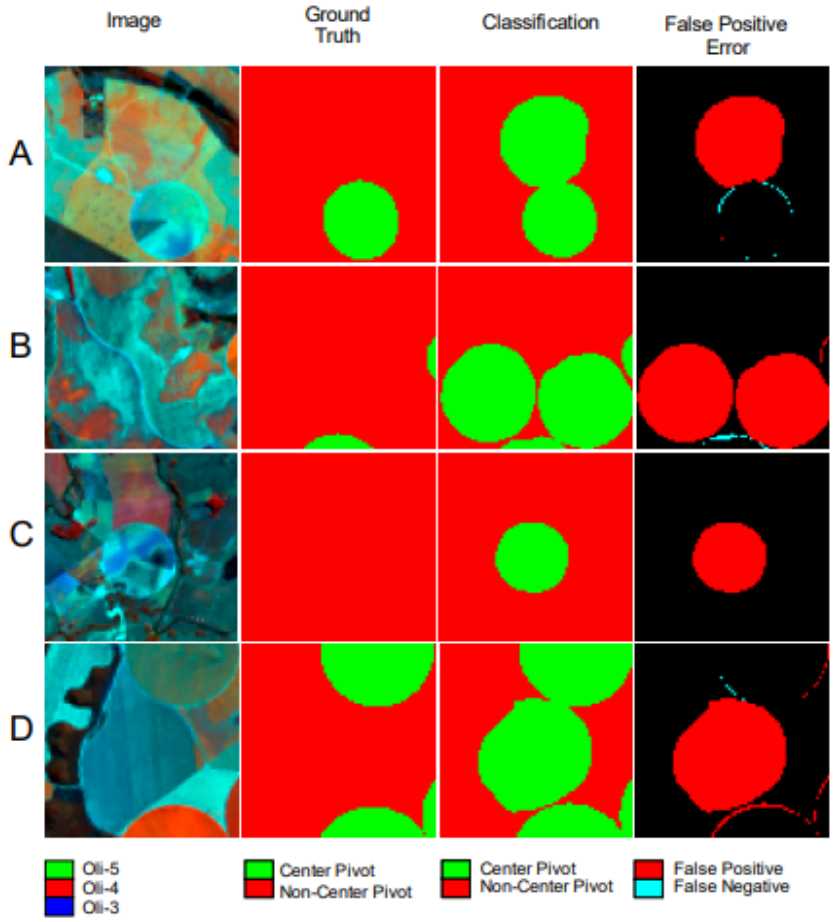

Figure II.14 Examples of false negatives (A–D) using the U-net, where detected central pivots do not correspond to terrestrial truth.

II.2.4 Discussion

The present research shows state-of-the-art image segmentation results with high accuracy for CPIS detection in all deep learning models analyzed. This approach has a significant contribution to faster CPIS identification when compared to visual interpretation mapping. The vast majority of CPIS inventories consist of visual interpretation of circular shapes from satellite images. Rundquist et al. [19] systematized 14 years of CPIS inventory in Nebraska. The authors found that dry conditions in Nebraska's state promoted a marked growth of CPIS during the period studied. Schmidt et al. [34] carried out the mapping of the CPIS for Brazil's southeastern region in 2002. The research found a total of 4134 CPIS, considering an error greater than 5% due to cloud interference and lack of contrast between the irrigated area and its surroundings. Sano et al. [33] assessed the growth of CPIS in the Federal District of Brazil in the period 1992–2002 to estimate water demand. In the 20 years, the number of center pivots grew from 55 to 104. Ferreira et al. [32] mapped 3781 CPIS in the State of Minas Gerais (Brazil) for the year 2008 using images from the China-Brazil Earth-Resources Satellite 2B / Couple Charged Device (CBERS2B / CCD) satellite. The most significant survey was conducted by the National Water Agency [3], which mapped the entire Brazilian territory in 2004, the data used in this survey.

U-net had slightly better metrics for our target compared to Deep ResUnet, contrasting with other segmentation studies with different targets [48,57,77]. De Bem et al. [48] compared these networks in deforest change detection and obtained better Kappa results for ResUnet (0.94) over U-net (0.91). In urban building detection, Yi et al. [57] also had better Kappa results for Deep ResUnet (0.9176) over U-net (0.8709). Zhang et al. [77] in road extraction analysis used precision-recall breakeven points to evaluate the performance of the models, obtaining closer values between Deep ResUnet (0.9187) and U-net (0.9053). Similarities between Deep ResUnet and U-net results in the present research are probably associated with the trained data. Differences in our data include seven-channel imagery and circular-shaped targets, which can provide simpler structures, showing the similarity between the methods. Even though SharpMask brings the worst accuracy performance, one advantage when compared to the other two networks is the faster training period.

The verified errors occur mostly in different border areas: (a) At the edge of the entire classification due to a smaller amount of overlapping pixels; (b) at the edge of the frames, because the geometric shape of the center pivots only appears partially; and (c) along the circumference of the center pivot, because there are small divergences in the manual labels and

the classified image. Previous research in the large image segmentation used the overlapping pixel values from the sliding window to attenuate frame edge errors [48,57]. A methodological novelty was a quantitative analysis by ROC and AUC to analyze the improvement in accuracy with the increase of the overlap area. We also proposed an index for the overlap data, considering the proportion of times the value was greater than 70%. In future research, errors of a semantic nature, such as the classification of abandoned center pivots, can be minimized with the use of a time series due to the ability to detect phenological changes in plantations.

II.2.5 Conclusions

This research focused on the detection of center pivots from three study areas in central Brazil, considering (a) the development of an extensive center pivot database that encompasses different environments in central Brazil and seasonal changes; (b) evaluation of three models based on CNN architecture; and (c) assessment of the procedure for image reconstruction, considering different variations of overlapping ranges. The results achieved state-of-the-art metrics, with the identification of nearly all center pivots. The training and test dataset had 5000 frames that used ground truth information from visual interpretation of the images, which guaranteed quality information and enriched the model's quality. The classification methods using U-net, Deep ResUnet, and SharpMask reached high values for the different accuracy metrics (total accuracy > 0.97, F-Score > 0.93, Recall > 0.90, Precision > 0.96, Kappa > 0.92, and IoU > 0.87). U-net had a slight advantage over Deep ResUnet. A significant contribution of this research was the image reconstruction proposition for large images, considering different stride values for the moving window, allowing several classified image overlays and a better pivot estimation per pixel. This procedure enables improvements in the final image. The results show that moving windows with little or lower overlapping pixels have significant errors at the edges of the frames, but also we identified a significant tradeoff when considering the execution time: No overlapping pixels is a 30 s task while using a large number of overlapping pixels is a task that takes nearly 9 h. This performance could be improved using better GPU processors. Although we already expected better results with stride reduction, the present research conducted a quantitative analysis of this improvement. Classification using deep semantic segmentation is essential, as it replaces manual labor and increases speed. Another crucial information in this research was the seasonal analysis, which is evidence that the best time to identify the presence of center pivots is at the beginning of the dry season since it shows greater

contrast with its surroundings, identifying nearly all center pivots present in the scene. This information has implications for agrarian and water management, energy consumption, and land use planning. Future studies should include the development of specific neural networks and test images of different sizes to see if the frame's training size has an impact on the result.

References

1. Alexandridis, T. K., Zalidis, G. C., & Silleos, N. G. (2008). Mapping irrigated area in Mediterranean basins using low cost satellite Earth Observation. *Computers and Electronics in Agriculture*, *64*(2), 93–103. https://doi.org/10.1016/j.compag.2008.04.001
2. Althoff, D., & Rodrigues, L. N. (2019). The expansion of center-pivot irrigation in the Cerrado biome. *IRRIGA*, *1*(1), 56–61. https://doi.org/10.15809/irriga.2019v1n1p56-61
3. ANA, A. N. de Á. (2016). Levantamento da Agricultura Irrigada por Pivôs Centrais no Brasil - 2014: *Relatório Síntese*; Agência Naciona de Águas (ANA): Brasília, BRasil, 2016; ISBN 978-85-8210-034-9.
4. Alexandratos, N.; Bruinsma, J. World Agriculture towards 2030/2050: (2012). The 2012 Revision; No. 12-03, ESAWorking Paper; FAO, Agricultural Development Economics Division: Rome, Italy.
5. Siebert, S., & Döll, P. (2010). Quantifying blue and green virtual water contents in global crop production as well as potential production losses without irrigation. *Journal of Hydrology*, *384*(3–4), 198–217. https://doi.org/10.1016/j.jhydrol.2009.07.031
6. Crist, E., Mora, C., & Engelman, R. (2017). The interaction of human population, food production, and biodiversity protection. *Science*, *356*(6335), 260–264. https://doi.org/10.1126/science.aal2011
7. Aznar-Sánchez, J. A., Belmonte-Ureña, L. J., Velasco-Muñoz, J. F., & Manzano-Agugliaro, F. (2018). Economic analysis of sustainable water use: A review of worldwide research. *Journal of Cleaner Production*, *198*, 1120–1132. https://doi.org/10.1016/j.jclepro.2018.07.066
8. Mancosu, N.; Snyder, R.L.; Kyriakakis, G.; Spano, D. (2015). Water scarcity and future challenges for food production. *Water*, 7, 975–992.
9. Velasco-Muñoz, J. F., Aznar-Sánchez, J. A., Batlles-delaFuente, A., & Fidelibus, M. D. (2019). Sustainable Irrigation in Agriculture: An Analysis of Global Research. *Water*, *11*(9), 1758.

https://doi.org/10.3390/w11091758

10. Velasco-Muñoz, J. F., Aznar-Sánchez, J.A.; Batlles-delaFuente, A.; Fidelibus, M.D.(2018) Advances in water use efficiency in agriculture: A bibliometric analysis. *Water*, 10, 377. https://doi.org/10.3390/w10040377
11. Velasco-Muñoz, J., Aznar-Sánchez, J., Belmonte-Ureña, L., & Román-Sánchez, I. (2018). Sustainable Water Use in Agriculture: A Review of Worldwide Research. *Sustainability*, *10*(4), 1084. https://doi.org/10.3390/su10041084
12. Cotterman, K. A., Kendall, A. D., Basso, B., & Hyndman, D. W. (2018). Groundwater depletion and climate change: future prospects of crop production in the Central High Plains Aquifer. *Climatic Change*, *146*(1–2), 187–200. https://doi.org/10.1007/s10584-017-1947-7
13. Myers, S. S., Smith, M. R., Guth, S., Golden, C. D., Vaitla, B., Mueller, N. D., Dangour, A. D., & Huybers, P. (2017). Climate Change and Global Food Systems: Potential Impacts on Food Security and Undernutrition. *Annual Review of Public Health*, *38*(1), 259–277. https://doi.org/10.1146/annurev-publhealth-031816-044356
14. Ambast, S. K., Keshari, A. K., & Gosain, A. K. (2002). Satellite remote sensing to support management of irrigation systems: concepts and approaches. *Irrigation and Drainage*, *51*(1), 25–39. https://doi.org/10.1002/ird.26
15. Ozdogan, M., Yang, Y., Allez, G., & Cervantes, C. (2010). Remote Sensing of Irrigated Agriculture: Opportunities and Challenges. *Remote Sensing*, *2*(9), 2274–2304. https://doi.org/10.3390/rs2092274
16. Thenkabail, P., Hanjra, M., Dheeravath, V., & Gumma, M. (2010). A Holistic View of Global Croplands and Their Water Use for Ensuring Global Food Security in the 21st Century through Advanced Remote Sensing and Non-remote Sensing Approaches. *Remote Sensing*, *2*(1), 211–261. https://doi.org/10.3390/rs2010211
17. Davis, K. F., Rulli, M. C., Seveso, A., & D'Odorico, P. (2017). Increased food production and reduced water use through optimized crop distribution. *Nature Geoscience*, *10*(12), 919–924. https://doi.org/10.1038/s41561-017-0004-5
18. Heller, R.C.; Johnson, K.A. (1979). Estimating irrigated land acreage from Landsat imagery. Photogramm. *Eng. Remote Sens*., 45, 1379–1386.
19. Rundquist, D.C.; Hoffman, R.O.; Carlson, M.P.; Cook, A.E. (1989). The Nebraska Center-Pivot Inventory: An example of operational satellite remote sensing on a long-term basis.

Photogramm. *Eng. Remote Sens*, 55, 587–590.

20. Chen, Yaoliang, Lu, D., Luo, L., Pokhrel, Y., Deb, K., Huang, J., & Ran, Y. (2018). Detecting irrigation extent, frequency, and timing in a heterogeneous arid agricultural region using MODIS time series, Landsat imagery, and ancillary data. *Remote Sensing of Environment*, *204*, 197–211. https://doi.org/10.1016/j.rse.2017.10.030
21. Ozdogan, M., & Gutman, G. (2008). A new methodology to map irrigated areas using multi-temporal MODIS and ancillary data: An application example in the continental US. *Remote Sensing of Environment*, *112*(9), 3520–3537. https://doi.org/10.1016/j.rse.2008.04.010
22. Pervez, M. S., & Brown, J. F. (2010). Mapping Irrigated Lands at 250-m Scale by Merging MODIS Data and National Agricultural Statistics. *Remote Sensing*, *2*(10), 2388–2412. https://doi.org/10.3390/rs2102388
23. Shahriar Pervez, M., Budde, M., & Rowland, J. (2014). Mapping irrigated areas in Afghanistan over the past decade using MODIS NDVI. *Remote Sensing of Environment*, *149*, 155–165. https://doi.org/10.1016/j.rse.2014.04.008
24. Bazzi, H., Baghdadi, N., Ienco, D., El Hajj, M., Zribi, M., Belhouchette, H., Escorihuela, M. J., & Demarez, V. (2019). Mapping Irrigated Areas Using Sentinel-1 Time Series in Catalonia, Spain. *Remote Sensing*, *11*(15), 1836. https://doi.org/10.3390/rs11151836
25. Bazzi, H., Baghdadi, N., El Hajj, M., Zribi, M., Minh, D. H. T., Ndikumana, E., Courault, D., & Belhouchette, H. (2019). Mapping Paddy Rice Using Sentinel-1 SAR Time Series in Camargue, France. *Remote Sensing*, *11*(7), 887. https://doi.org/10.3390/rs11070887
26. Bousbih, S., Zribi, M., El Hajj, M., Baghdadi, N., Lili-Chabaane, Z., Gao, Q., & Fanise, P. (2018). Soil Moisture and Irrigation Mapping in A Semi-Arid Region, Based on the Synergetic Use of Sentinel-1 and Sentinel-2 Data. *Remote Sensing*, *10*(12), 1953. https://doi.org/10.3390/rs10121953
27. Gao, Q., Zribi, M., Escorihuela, M., Baghdadi, N., & Segui, P. (2018). Irrigation Mapping Using Sentinel-1 Time Series at Field Scale. *Remote Sensing*, *10*(9), 1495. https://doi.org/10.3390/rs10091495
28. Demarez, V., Helen, F., Marais-Sicre, C., & Baup, F. (2019). In-Season Mapping of Irrigated Crops Using Landsat 8 and Sentinel-1 Time Series. *Remote Sensing*, *11*(2), 118. https://doi.org/10.3390/rs11020118

29. Fieuzal, R., Duchemin, B., Jarlan, L., Zribi, M., Baup, F., Merlin, O., Hagolle, O., & Garatuza-Payan, J. (2011). Combined use of optical and radar satellite data for the monitoring of irrigation and soil moisture of wheat crops. *Hydrology and Earth System Sciences*, *15*(4), 1117–1129. https://doi.org/10.5194/hess-15-1117-2011

30. Hadria, R., Duchemin, B., Jarlan, L., Dedieu, G., Baup, F., Khabba, S., Olioso, A., & Le Toan, T. (2010). Potentiality of optical and radar satellite data at high spatio-temporal resolutions for the monitoring of irrigated wheat crops in Morocco. *International Journal of Applied Earth Observation and Geoinformation*, *12*, S32–S37. https://doi.org/10.1016/j.jag.2009.09.003

31. Martins, J. D., Bohrz, I. S., Tura, E. F., Fredrich, M., Veronez, R. P., & Kunz, G. A. (2018). Levantamento da área irrigada por pivô central no Estado do Rio Grande do Sul. *IRRIGA*, *21*(2), 300. https://doi.org/10.15809/irriga.2016v21n2p300-311

32. Ferreira, E., Toledo, J. H. D. E., Dantas, A. A. A., & Pereira, R. M. (2011). Cadastral Maps of Irrigated Areas By Center Pivots in the State of. *Engenharia Agrícola*, *31*(4), 771–780.

33. Sano, E.E.; Lima, J.E.; Silva, E.M.; Oliveira, E.C. (2005). Estimative variation in the water demand for irrigation by center pivot in Distrito Federal-Brazil, between 1992 and 2002. *Eng. Agríc*., 25, 508–515.

34. Schmidt, W., Coelho, R. D., Jacomazzi, M. A., & Antunes, M. A. H. (2004). Distribuição espacial de pivôs centrais no Brasil: I - região sudeste. *Revista Brasileira de Engenharia Agrícola e Ambiental*, *8*(2–3), 330–333. https://doi.org/10.1590/s1415-43662004000200026

35. Garcia-Garcia, A., Orts-Escolano, S., Oprea, S., Villena-Martinez, V., & Garcia-Rodriguez, J. (2017). A Review on Deep Learning Techniques Applied to Semantic Segmentation. http://arxiv.org/abs/1704.06857

36. Garcia-Garcia, A., Orts-Escolano, S., Oprea, S., Villena-Martinez, V., Martinez-Gonzalez, P., & Garcia-Rodriguez, J. (2018). A survey on deep learning techniques for image and video semantic segmentation. *Applied Soft Computing*, *70*, 41–65. https://doi.org/10.1016/j.asoc.2018.05.018

37. Guo, Y., Liu, Y., Georgiou, T., & Lew, M. S. (2018). A review of semantic segmentation using deep neural networks. *International Journal of Multimedia Information Retrieval*, *7*(2), 87–93. https://doi.org/10.1007/s13735-017-0141-z

38. Guo, Y.; Liu, Y.; Oerlemans, A.; Lao, S.; Wu, S.; Lew, M.S. (2016). Deep learning for visual

understanding: A review. *Neurocomputing*, 187, 27–48. https://doi.org/10.1016/j.neucom.2015.09.116

39. Ma, L., Liu, Y., Zhang, X., Ye, Y., Yin, G., & Johnson, B. A. (2019). Deep learning in remote sensing applications: A meta-analysis and review. *ISPRS Journal of Photogrammetry and Remote Sensing*, *152*, 166–177. https://doi.org/10.1016/j.isprsjprs.2019.04.015
40. Carranza-García, M., García-Gutiérrez, J., & Riquelme, J. (2019). A Framework for Evaluating Land Use and Land Cover Classification Using Convolutional Neural Networks. *Remote Sensing*, *11*(3), 274. https://doi.org/10.3390/rs11030274
41. Kussul, N., Lavreniuk, M., Skakun, S., & Shelestov, A. (2017). Deep Learning Classification of Land Cover and Crop Types Using Remote Sensing Data. *IEEE Geoscience and Remote Sensing Letters*, *14*(5), 778–782. https://doi.org/10.1109/LGRS.2017.2681128
42. Li, M., Wang, L., Wang, J., Li, X., & She, J. (2020). Comparison of land use classification based on convolutional neural network. *Journal of Applied Remote Sensing*, *14*(01), 1. https://doi.org/10.1117/1.JRS.14.016501
43. Scott, G. J., England, M. R., Starms, W. A., Marcum, R. A., & Davis, C. H. (2017). Training Deep Convolutional Neural Networks for Land–Cover Classification of High-Resolution Imagery. *IEEE Geoscience and Remote Sensing Letters*, *14*(4), 549–553. https://doi.org/10.1109/LGRS.2017.2657778
44. Li, Wenmei, Liu, H., Wang, Y., Li, Z., Jia, Y., & Gui, G. (2019). Deep Learning-Based Classification Methods for Remote Sensing Images in Urban Built-Up Areas. *IEEE Access*, *7*, 36274–36284. https://doi.org/10.1109/ACCESS.2019.2903127
45. Huang, B., Zhao, B., & Song, Y. (2018). Urban land-use mapping using a deep convolutional neural network with high spatial resolution multispectral remote sensing imagery. *Remote Sensing of Environment*, *214*, 73–86. https://doi.org/10.1016/j.rse.2018.04.050
46. Xu, Y., Wu, L., Xie, Z., & Chen, Z. (2018). Building Extraction in Very High Resolution Remote Sensing Imagery Using Deep Learning and Guided Filters. *Remote Sensing*, *10*(1), 144. https://doi.org/10.3390/rs10010144
47. Wagner, F., Dalagnol, R., Tarabalka, Y., Segantine, T., Thomé, R., & Hirye, M. (2020). U-Net-Id, an Instance Segmentation Model for Building Extraction from Satellite Images—Case Study in the Joanópolis City, Brazil. *Remote Sensing*, *12*(10), 1544. https://doi.org/10.3390/rs12101544
48. de Bem, P., de Carvalho Junior, O., Fontes Guimarães, R., & Trancoso Gomes, R. (2020).

Change Detection of Deforestation in the Brazilian Amazon Using Landsat Data and Convolutional Neural Networks. *Remote Sensing*, *12*(6), 901. https://doi.org/10.3390/rs12060901

49. Ma, W., Xiong, Y., Wu, Y., Yang, H., Zhang, X., & Jiao, L. (2019). Change Detection in Remote Sensing Images Based on Image Mapping and a Deep Capsule Network. *Remote Sensing*, *11*(6), 626. https://doi.org/10.3390/rs11060626
50. Peng, D., Zhang, Y., & Guan, H. (2019). End-to-End Change Detection for High Resolution Satellite Images Using Improved UNet++. *Remote Sensing*, *11*(11), 1382. https://doi.org/10.3390/rs11111382
51. Zhang, W., & Lu, X. (2019). The Spectral-Spatial Joint Learning for Change Detection in Multispectral Imagery. *Remote Sensing*, *11*(3), 240. https://doi.org/10.3390/rs11030240
52. Chen, Yang, Fan, R., Bilal, M., Yang, X., Wang, J., & Li, W. (2018). Multilevel Cloud Detection for High-Resolution Remote Sensing Imagery Using Multiple Convolutional Neural Networks. *ISPRS International Journal of Geo-Information*, *7*(5), 181. https://doi.org/10.3390/ijgi7050181
53. Jeppesen, J. H., Jacobsen, R. H., Inceoglu, F., & Toftegaard, T. S. (2019). A cloud detection algorithm for satellite imagery based on deep learning. *Remote Sensing of Environment*, *229*, 247–259. https://doi.org/10.1016/j.rse.2019.03.039
54. Li, Z., Shen, H., Cheng, Q., Liu, Y., You, S., & He, Z. (2019). Deep learning based cloud detection for medium and high resolution remote sensing images of different sensors. *ISPRS Journal of Photogrammetry and Remote Sensing*, *150*, 197–212. https://doi.org/10.1016/j.isprsjprs.2019.02.017
55. Xie, F., Shi, M., Shi, Z., Yin, J., & Zhao, D. (2017). Multilevel Cloud Detection in Remote Sensing Images Based on Deep Learning. *IEEE Journal of Selected Topics in Applied Earth Observations and Remote Sensing*, *10*(8), 3631–3640. https://doi.org/10.1109/JSTARS.2017.2686488
56. Zhang, C., Yue, P., Di, L., & Wu, Z. (2018). Automatic Identification of Center Pivot Irrigation Systems from Landsat Images Using Convolutional Neural Networks. *Agriculture*, *8*(10), 147. https://doi.org/10.3390/agriculture8100147
57. Yi, Y., Zhang, Z., Zhang, W., Zhang, C., Li, W., & Zhao, T. (2019). Semantic Segmentation of Urban Buildings from VHR Remote Sensing Imagery Using a Deep Convolutional Neural

Network. *Remote Sensing*, *11*(15), 1774. https://doi.org/10.3390/rs11151774

58. De Oliveira Hessel, F., De Carvalho Junior, O. A., Gomes, R. A. T., De Souza Martins, E., & Guimarães, R. F. (2012). Dinâmica e sucessão dos padrões da paisagem agrícola no município de Cocos (Bahia). *RAE GA - O Espaco Geografico Em Analise*, *26*(26), 128–156. https://doi.org/10.5380/raega.v26i0.30153

59. Oliveira, S. N. De, Abílio, O., Júnior, D. C., Arnaldo, R., Gomes, T., Guimarães, R. F., & Martins, É. D. S. (2014). Land-use and land-cover change detection using post-classification method in the agricultural frontier of Western Bahia over the Urucuia Group during the period 1988-2011. *Revista Brasileira de Cartografia (2014)*, *66*(5), 1157–1176.

60. de Oliveira, S. N., de Carvalho Júnior, O. A., Gomes, R. A. T., Guimarães, R. F., & McManus, C. M. (2017). Landscape-fragmentation change due to recent agricultural expansion in the Brazilian Savanna, Western Bahia, Brazil. *Regional Environmental Change*, *17*(2), 411–423. https://doi.org/10.1007/s10113-016-0960-0

61. Nunes de Oliveira, S., Abílio de Carvalho Júnior, O., Trancoso Gomes, R. A., Fontes Guimarães, R., & McManus, C. M. (2017). Deforestation analysis in protected areas and scenario simulation for structural corridors in the agricultural frontier of Western Bahia, Brazil. *Land Use Policy*, *61*, 40–52. https://doi.org/10.1016/j.landusepol.2016.10.046

62. Menke, A.B.; Carvalho Júnior, O.A.; Gomes, R.A.T.; Martins, E.S.; Oliveira, S.N. (2009). Análise das mudanças do uso agrícola da terra a partir de dados de sensoriamento remoto multitemporal no município de Luís Eduardo Magalhães (BA–Brasil). *Soc. Nat*. 21, 315–326.

63. Pousa, R., Costa, M. H., Pimenta, F. M., Fontes, V. C., Brito, V. F. A. de, & Castro, M. (2019). Climate Change and Intense Irrigation Growth in Western Bahia, Brazil: The Urgent Need for Hydroclimatic Monitoring. *Water*, *11*(5), 933. https://doi.org/10.3390/w11050933

64. Brunckhorst, A.; Bias, E. Aplicação de SIG na gestão de conflitos pelo uso da água na porção goiana da bacia hidrográfica do rio São Marcos, município de Cristalina–GO. *Geociências* 2014, 33, 228–243.

65. Pinhati, F.S.C. Simulações de ampliações da irrigação por Pivô Central na Bacia do Rio São Marcos. Master's Thesis, *University of Brasília, Brasília,* Brazil, 2018.

66. Sano, E.E.; Lima, J.E.F.W.; Silva, E.M.; Oliveira, E.C. (2005). Estimativa da Variação na Demanda de Água para Irrigação por Pivô-Central no Distrito Federal entre 1992 e 2002. *Eng. Agríc,* 25, 508–515.

67. Silva, L. M. D. C., & Da Hora, M. D. A. G. M. (2014). Conflito pelo uso da água na bacia hidrográfica do rio São Marcos: o estudo de caso DA UHE Batalha. *Engevista*, *17*(2), 166. https://doi.org/10.22409/engevista.v17i2.633

68. Galford, G. L., Mustard, J. F., Melillo, J., Gendrin, A., Cerri, C. C., & Cerri, C. E. P. (2008). Wavelet analysis of MODIS time series to detect expansion and intensification of row-crop agriculture in Brazil. *Remote Sensing of Environment*, *112*(2), 576–587. https://doi.org/10.1016/j.rse.2007.05.017

69. Arvor, D., Jonathan, M., Meirelles, M. S. P., Dubreuil, V., & Durieux, L. (2011). Classification of MODIS EVI time series for crop mapping in the state of Mato Grosso, Brazil. *International Journal of Remote Sensing*, *32*(22), 7847–7871. https://doi.org/10.1080/01431161.2010.531783

70. Bernardes, T., Adami, M., Formaggio, A. R., Moreira, M. A., França, D. de A., & de Novaes, M. R. (2011). Imagens mono e multitemporais Modis para estimativa da área com soja no Estado de Mato Grosso. *Pesquisa Agropecuaria Brasileira*, *46*(11), 1530–1537. https://doi.org/10.1590/S0100-204X2011001100015

71. Gusso, A., Arvor, D., Ricardo Ducati, J., Veronez, M. R., & Da Silveira, L. G. (2014). Assessing the modis crop detection algorithm for soybean crop area mapping and expansion in the Mato Grosso state, Brazil. *The Scientific World Journal*, *2014*(1). https://doi.org/10.1155/2014/863141

72. Agência Nacional de Águas (ANA). (2019). Levantamento da agricultura irrigada por pivôs centrais no Brasil/Agência Nacional de Águas, Embrapa Milho e Sorgo, 2nd ed.; Brasília, Brazil.

73. Vermote, E., Justice, C., Claverie, M., & Franch, B. (2016). Preliminary analysis of the performance of the Landsat 8/OLI land surface reflectance product. *Remote Sensing of Environment*, *185*, 46–56. https://doi.org/10.1016/j.rse.2016.04.008

74. Abade, N., Júnior, O., Guimarães, R., & de Oliveira, S. (2015). Comparative Analysis of MODIS Time-Series Classification Using Support Vector Machines and Methods Based upon Distance and Similarity Measures in the Brazilian Cerrado-Caatinga Boundary. *Remote Sensing*, *7*(9), 12160–12191. https://doi.org/10.3390/rs70912160

75. Carvalho Júnior, Osmar Abílio de, Sampaio, C. da S., Silva, N. C. da, Couto Júnior, A. F., Gomes, R. A. T., Carvalho, A. P. F. de, & Shimabukuro, Y. E. (2008). Classificação de

padrões de savana usando assinaturas temporais NDVI do sensor MODLS no Parque Nacional Chapada dos Veadeiros. *Revista Brasileira de Geofísica*, *26*(4), 505–517. https://doi.org/10.1590/s0102-261x2008000400010

76. Ronneberger, O., Fischer, P., & Brox, T. (2015). U-Net: Convolutional Networks for Biomedical Image Segmentation. http://arxiv.org/abs/1505.04597
77. Zhang, Z., Liu, Q., & Wang, Y. (2018). Road Extraction by Deep Residual U-Net. *IEEE Geoscience and Remote Sensing Letters*, *15*(5), 749–753. https://doi.org/10.1109/LGRS.2018.2802944
78. Pinheiro, P.O.; Lin, T.Y.; Collobert, R.; Dollár, P. (2016). Learning to Refine Object Segments. In Lecture Notes in Computer Science, Proceedings of the Computer Vision–ECCV 2016, Amsterdam, The Netherlands, 11–14 October 2016; Leibe, B., Matas, J., Sebe, N., Welling, M., Eds.; Springer: Cham, Switzerland; v. 9905; pp. 75–91.
79. He, H., Yang, D., Wang, S., Wang, S., & Li, Y. (2019). Road Extraction by Using Atrous Spatial Pyramid Pooling Integrated Encoder-Decoder Network and Structural Similarity Loss. *Remote Sensing*, *11*(9), 1015. https://doi.org/10.3390/rs11091015
80. Feng, W., Sui, H., Huang, W., Xu, C., & An, K. (2019). Water Body Extraction From Very High-Resolution Remote Sensing Imagery Using Deep U-Net and a Superpixel-Based Conditional Random Field Model. *IEEE Geoscience and Remote Sensing Letters*, *16*(4), 618–622. https://doi.org/10.1109/LGRS.2018.2879492
81. Li, Weijia, He, C., Fang, J., Zheng, J., Fu, H., & Yu, L. (2019). Semantic Segmentation-Based Building Footprint Extraction Using Very High-Resolution Satellite Images and Multi-Source GIS Data. *Remote Sensing*, *11*(4), 403. https://doi.org/10.3390/rs11040403
82. Cui, B., Fei, D., Shao, G., Lu, Y., & Chu, J. (2019). Extracting Raft Aquaculture Areas from Remote Sensing Images via an Improved U-Net with a PSE Structure. *Remote Sensing*, *11*(17), 2053. https://doi.org/10.3390/rs11172053
83. Ding, K., Yang, Z., Wang, Y., & Liu, Y. (2019). An Improved Perceptual Hash Algorithm Based on U-Net for the Authentication of High-Resolution Remote Sensing Image. *Applied Sciences*, *9*(15), 2972. https://doi.org/10.3390/app9152972
84. Liu, Z.; Feng, R.; Wang, L.; Zhong, Y.; Cao, L. (2019). D-Resunet: Resunet and Dilated Convolution for High Resolution Satellite Imagery Road Extraction. In Proceedings of the 2019 IEEE International Geoscience and Remote Sensing Symposium—I*GARSS 2019*, Yokohama, Japan, 28 July–2 August 2109; pp. 3927–3930.

85. Diakogiannis, F. I., Waldner, F., Caccetta, P., & Wu, C. (2020). ResUNet-a: A deep learning framework for semantic segmentation of remotely sensed data. *ISPRS Journal of Photogrammetry and Remote Sensing*, *162*, 94–114. https://doi.org/10.1016/j.isprsjprs.2020.01.013

86. Congalton, R.G.; Oderwald, R.G.; Mead, R.A. (1983). Assessing Landsat classification accuracy using discrete multivariate analysis statistical techniques. Photogramm. *Eng. Remote Sensing*, 49, 1671–1678.

87. Foody, G. M. (2002). Status of land cover classification accuracy assessment. *Remote Sensing of Environment*, *80*(1), 185–201. https://doi.org/10.1016/S0034-4257(01)00295-4

88. Everingham, M., Van Gool, L., Williams, C. K. I., Winn, J., & Zisserman, A. (2010). The Pascal Visual Object Classes (VOC) Challenge. *International Journal of Computer Vision*, *88*(2), 303–338. https://doi.org/10.1007/s11263-009-0275-4

89. Hoiem, D.; Chodpathumwan, Y.; Dai, Q. (2012). Diagnosing error in object detectors. In Proceedings of the 12th European Conference on Computer Vision—Volume Part III (ECCV'12), Florence, Italy, 7–13 October 2012; Fitzgibbon, A., Lazebnik, S., Perona, P., Sato, Y., Schmid, C., Eds.; *Springer*: Berlin/Heidelberg, Germany; pp. 340–353.

90. Russakovsky, O., Deng, J., Su, H., Krause, J., Satheesh, S., Ma, S., Huang, Z., Karpathy, A., Khosla, A., Bernstein, M., Berg, A. C., & Fei-Fei, L. (2015). ImageNet Large Scale Visual Recognition Challenge. *International Journal of Computer Vision*, *115*(3), 211–252. https://doi.org/10.1007/s11263-015-0816-y

91. Stehman, S. V., & Wickham, J. D. (2011). Pixels, blocks of pixels, and polygons: Choosing a spatial unit for thematic accuracy assessment. *Remote Sensing of Environment*, *115*(12), 3044–3055. https://doi.org/10.1016/j.rse.2011.06.007

92. Ye, S., Pontius, R. G., & Rakshit, R. (2018). A review of accuracy assessment for object-based image analysis: From per-pixel to per-polygon approaches. *ISPRS Journal of Photogrammetry and Remote Sensing*, *141*, 137–147. https://doi.org/10.1016/j.isprsjprs.2018.04.002

93. Carvalho Júnior, Osmar A., Guimarães, R. F., Gillespie, A. R., Silva, N. C., & Gomes, R. A. T. (2011). A New Approach to Change Vector Analysis Using Distance and Similarity Measures. *Remote Sensing*, *3*(11), 2473–2493. https://doi.org/10.3390/rs3112473

CAPÍTULO

III. INSTANCE SEGMENTATION OF CENTER PIVOT IRRIGATION SYSTEMS USING MULTI-TEMPORAL SENTINEL-1 SAR IMAGES

Resumo

O mapeamento de Sistemas de Irrigação por Pivô Central (SIPC) é essencial para a gestão de recursos agrícolas e hídricos. Nesse contexto, métodos baseados em *Deep Learning* (DL) alcançaram o estado da arte na classificação de imagens de sensoriamento remoto. Porém, o mapeamento do SIPC com DL ainda se restringe a imagens ópticas com limitações em ambientes tropicais devido à extensa cobertura de nuvens por longos períodos. A presente pesquisa propõe a detecção de CPIS usando segmentação de instância de imagens de SAR multi-temporais que estão livres de nuvens. A pesquisa desenvolveu um banco de dados SIPC para o bioma Cerrado baseado em interpretação visual, totalizando 3675 instâncias no formato de anotação *Common Objects in Context* (COCO). O treinamento utilizou o *Mask-RCNN* com o *backbone* ResNeXt-101-32x8d considerando diferentes arranjos de dados: (a) variação no número de imagens temporais Sentinel-1 com intervalo de 12 dias (de 1 a 11 imagens), e (b) comparação das polarizações VV, VH e VV + VH. O mapeamento da área de estudo em grande dimensão utilizou a técnica do mosaico a partir de janela deslizante. Os resultados mostram uma melhora da precisão com o aumento do número de imagens temporais, chegando a uma diferença maior que 15% AP ao comparar uma única imagem e o conjunto de imagens com a pontuação máxima no VV (oito imagens), VH (dez imagens) e polarizações VV + VH (nove imagens). O uso combinado das duas polarizações (VV + VH) teve resultados ligeiramente melhores (75% AP, 91% AP50 e 86% AP75) do que os outros. No entanto, a polarização VV pode ter uma vantagem, obtendo resultados próximos com menos imagem e custo computacional. A segmentação por instância proporciona uma classificação diferente para cada objeto pertencente a uma mesma classe, favorecendo a contagem total do SIPC e o cálculo do tamanho.

Palavras-chave: Máscara R – CNN, *Deep Learning*, Pivô central, Imagens SAR, Séries Temporais.

Artigo publicado na revista *Remote Sensing Applications: Society and Environment*, 2021. DOI: 10.1016/j.rsase.2021.100537

Abstract

The mapping of Center Pivot Irrigation Systems (CPIS) is essential for agricultural and water resource management. In this context, methods based on Deep Learning (DL) have reached state-of-the-art in the classification of remote sensing images. However, the mapping of CPIS with DL is still restricted to optical images with limitations in tropical environments due to the extensive cloud cover for long periods. The present research proposes the detection of CPIS using instance segmentation from multitemporal SAR images that are cloud-free. The research developed a CPIS database for the Cerrado biome based on visual interpretation, totaling 3675 instances in the Common Objects in Context (COCO) annotation format. The training used the Mask-RCNN with the ResNeXt-101-32x8d backbone considering different data arrangements: (a) variation in the number of Sentinel-1 temporal images with an interval of 12 days (from 1 to 11 images), and (b) comparison of VV, VH, and VV + VH polarizations. The study area mapping with a large dimension used the mosaic technique from a sliding window. The results show an accuracy improvement with the increase in the number of temporal images, reaching a difference greater than 15% AP when comparing a single image and the set of images with the maximum score in the VV (eight images), VH (ten images) and VV + VH (nine images) polarizations. The combined use of the two polarizations (VV + VH) had slightly better results (75% AP, 91% AP50, and 86% AP75) than the others. However, VV polarization may have an advantage, obtaining close results from less image and computational cost. The segmentation by instance provides a different classification for each object belonging to the same class, favoring the total CPIS count and the size calculation.

Keywords: Mask R-CNN Deep learning, Center pivot SAR imagery Time series.

III.1 Introduction

The projection of world population growth until 2100 estimates an increase of 3.9 billion more than the current population (7.7 billion people) (ONU Department of Economic and Social Affairs, 2019) makes the agricultural production strategies fundamental to guarantee food security (Godfray et al., 2010; Pollice et al., 2018). Nevertheless, the agricultural area's indiscriminate expansions have adverse effects on the environmental equilibriums, and the viable solution is to intensify the agricultural productivity to achieve an environmental balance (Beltran-Pea et al., 2020; Foley et al., 2011; Tilman et al., 2011). The intensification of land production requires technologies (irrigation and fertilization) to obtain cropping systems that maximize crop yields (reaching three harvests/year) and improved water use efficiency (Cao et al., 2018; Rosa et al., 2020).

Irrigation includes various technologies, practices, and management to optimize agricultural systems (Gebbers and Adamchuk, 2010). Among the different technologies, Center Pivot Irrigation Systems (CPIS) is one of the most advanced techniques, containing water sprinklers rotating on its axis that guarantees the water distribution evenly in crops. Water consumption for agriculture is essential to ensure sustainable development (Siebert and Döll, 2010).

In Brazil, the National Water Agency (ANA) is responsible for evaluating water availability to the diverse national demands, aiming to use the resources efficiently. Between 1985 and 2017, the number of CPISs in Brazil went from less than 1000 to almost 25,000, increasing the area by 14,000,000 ha (Agência Nacional de). The ANA performs the CPIS mapping based on visual interpretation of optical remote sensing data, containing unmapped areas due to the lack of cloud cover-free images. Even though there was a substantial rise of this technology, visual interpretation remained as one of the most used methods to identify CPIS since the 80s (Heller and Johnson, 1979; Rundquist et al., 1989) up until this decade (Agência Nacional de Águas, 2016, 2019), which is laborious and time-consuming. Thus, automated CPIS detection processes allow quick, frequent, and low-cost surveys, increasing public managers' decision-making capacity.

Deep Learning (DL) is an up-and-coming field for detecting different targets, enabling the processing of low and high-level features in multidimensional arrays (Lecun et al., 2015). Different DL applications use the convolutional neural network (CNN) in images, but the most common remote sensing approach is classification, object detection, semantic segmentation, and instance segmentation (Ma et al., 2019). The most straightforward approach is image

classification, where for a given input image, the output is a label. Object detection establishes bounding boxes around the objects of interest. Semantic segmentation is a pixel-wise classification where all pixels of a given image receive a label. Instance segmentation outputs bounding boxes and pixel-wise segmentation masks on the objects of interest. The DL processing in remote sensing images presents additional complexities, requiring different databases for the various sensors (optical and SAR) with specific spatial and spectral resolutions. Moreover, the sizeable remote sensing image requires cropping tiles in particular sizes for training and segmentation and, consequently, an image reconstruction procedure through sliding windows with overlapping pixels to mitigate frame edge errors (de Bem et al., 2020; Yi et al., 2019).

CPIS is a suitable target for the use of Deep Learning (DL) in remote sensing images due to the following factors: (1) large dimensions, which are visible through a wide variety of sensors and resolutions; (2) round shapes; and (3) many samples, which are essential for training DL networks. Recently, studies addressed CPIS monitoring using DL. Zhang et al. (2018) were pioneers using classification, but other works tried more complex methods such as semantic segmentation (de Albuquerque et al., 2020; Saraiva et al., 2020), object detection (Tang et al., 2021a, 2021b), and instance segmentation (Carvalho et al., 2021). Nevertheless, despite the relevant studies and good results, all used optical imagery with cloud-cover limitations. An alternative is the use of a Synthetic Aperture Radar (SAR) image capable of penetrating clouds and smoke, has no shadow interference, and acquires data night and day.

Besides, the availability of dense SAR time series data opens perspectives for improving CPIS detection. The CPIS areas have a complex temporal dynamic, with different plantations, cropping systems, crop rotation, tillage practice, and irrigation management. Thus, different center pivots may have similar characteristics with their surroundings at any given time. However, with a more extended period, the possibilities of delimiting the shapes increase, and speckle noise interference decreases. Therefore, a sequence of multitemporal SAR images can improve the CPIS detection with an invariant shape but with complex and diversified agricultural activities over time. This approach differs from DL applications with multitemporal SAR images: (a) change detection using supervised (Iino et al., 2018; Jaturapitpornchai et al., 2020; Liu et al., 2017; Zhang et al., 2020) or unsupervised methods (Cui et al., 2019; Gao et al., 2017; Li et al., 2019; Luo et al., 2019); and (b) phenology-based mapping to crops (de Castro Filho et al., 2020; Jo et al., 2020; Ndikumana et al., 2018). Some DL studies integrate multitemporal radar and optical images in target detection (Feng et al., 2019; Liao et al., 2020).

The present study aims to detect center pivots using Sentinel-1 time series and instance segmentation. The secondary objectives are: (1) evaluate differences between VV, VH, and VV + VH polarizations; (2) estimate the best number of temporal images to improve segmentation accuracy; and (3) apply mosaicking using a sliding window to classify large areas.

III.2 Material and Methods

The present research had the following methodological steps: (2.1) dataset; (2.2) model configurations; (2.3) model evaluation; and (2.4) practical applications (**Figure III.1**).

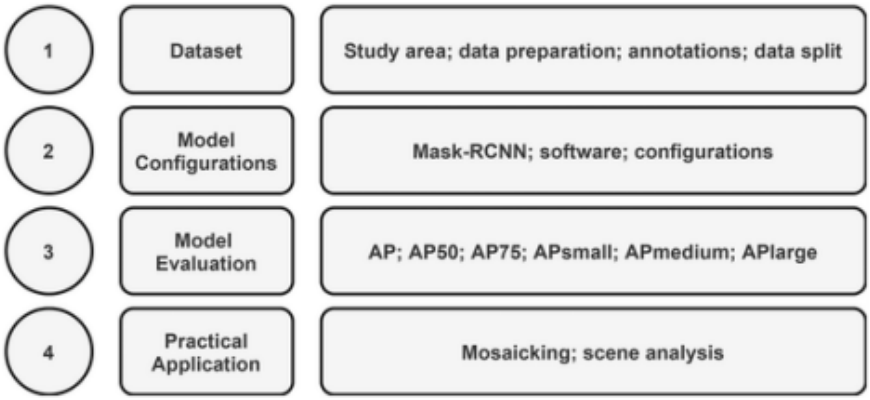

Figure III.1 Methodological flowchart.

III.2.1 Dataset

III.2.1.1 Study area

The Cerrado biome is the main irrigation area in the Brazilian territory, containing about 73% of all center pivots and playing a crucial role in the region's socio-economic development (Althoff and Rodrigues, 2019). However, water scarcity in the region causes conflicts over the multiple uses of water resources (Pousa et al., 2019), making CPIS growth monitoring essential for sustainable development. In the Cerrado biome, the region close to the Federal District has the highest center pivots density. The study area has 3675 pivots (**Figure III.2**).

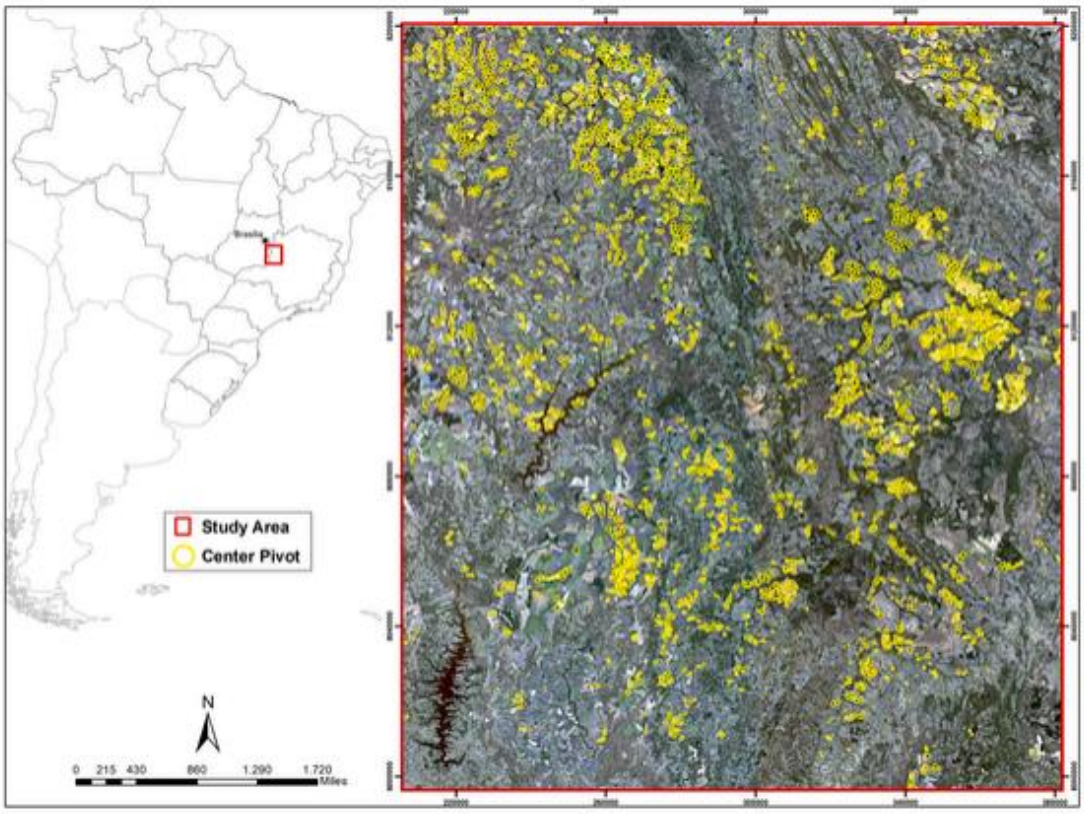

Figure III.2 Study Area located at Central Brazil in the Cerrado biome.

III.2.1.2 Data preparation

The European Space Agency (ESA) SAR Sentinel-1 mission has a constellation of two polar-orbiting satellites launched in 2014 and 2016, having a revisit time of twelve days with a single satellite and six days with both. The Sentinel-1 sensors operate in the C band (5.4 GHz) in VV (Vertical transmitting, Vertical receiving) and VH (Vertical transmitting, Horizontal receiving) polarizations. The Sentinel-1 images are available free of charge (https://scihub.copernicus.eu/dhus/#/home). In the present study, we acquired eleven Sentinel-1 temporal images relative to the Ground Range Detected (GRD) product in Interferometric Wide Swath mode, with a 10-m resolution image and interval of 12 days that result in a four-month period that avoids the creation or disappearance of center pivots. The dense time series allows accurate mapping of agricultural activities. In the pre-processing of SAR images, we perform the following procedures using the Sentinel Application Platform (SNAP) software (Filipponi, 2019): apply orbit file; calibration (a procedure that converts digital pixel values to radiometrically calibrated SAR backscatter); a range-Doppler terrain correction by utilizing the Shuttle Radar Topography Mission (SRTM) data; and linear conversion in decibels (dB).

Figure III.3 shows the same location in the 11 different time frames with the center

pivots highlighted in black. The identification of center pivots using only a frame can be challenging, even for specialists. However, the combination of temporal images minimizes SAR noise and emphasizes the center pivot's limits by small changes in planting, favoring the DL model. **Figure III.4** demonstrates an RGB composition with three SAR channels relative to times 1, 6, and 11 using the VV polarization, clearly highlighting the center pivot's presence.

III.2.1.3 Ground truth annotations

Image annotation is critical for supervised DL tasks. Conventional annotation formats increase interoperability due to compatibility with a wide variety of algorithms. The Common Objects in Context (COCO) annotation format (Lin et al., 2014) is one of the most used, having compatibility with diverse software, such as Detectron2 (Wu et al., 2019). Usually, ground truth annotations in remote sensing studies use vector data from digital image processing software and geographic information system (GIS), which are not immediately compatible with the DL annotation format. Thus, an initial challenge is to convert vector data to the COCO annotation format.

The first step was to annotate all center pivots in the Goiás/Minas region using ArcGIS software. The center pivots' vectorization used visual interpretation on a computer screen from cloud-free Sentinel-2 optical images within the study period. Optical images allow for better visual distinction as they have less noise interference and more significant spectral difference. As instance segmentation models require a unique distinction among objects belonging to the same class, we attributed a value from 1 to N to each polygon (i.e., center pivots), resulting in the ground truth (GT) image.

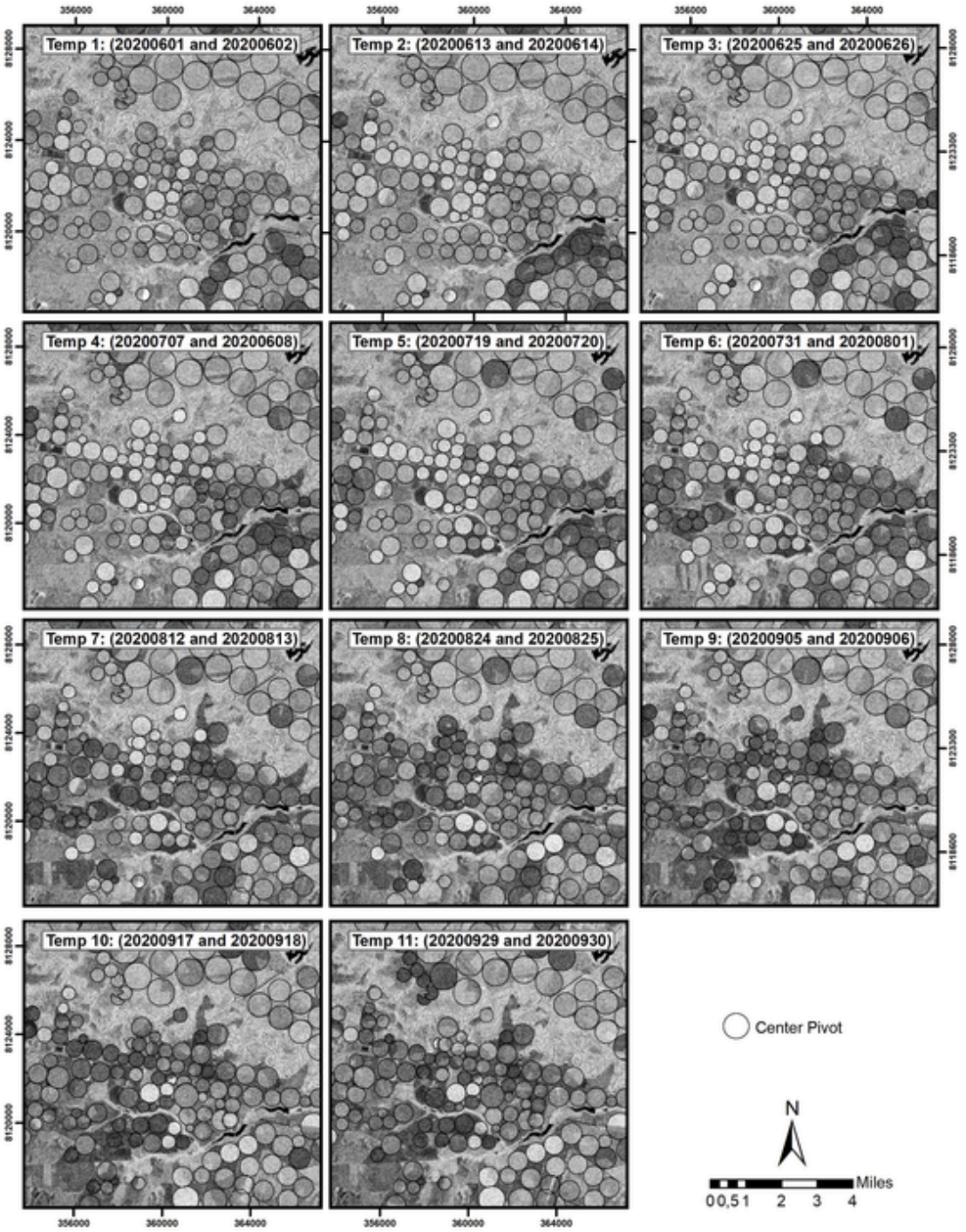

Figure III.3 Representation of a cropped image from each of the time frames from 1 to 11, with the center pivots highlighted in black contours.

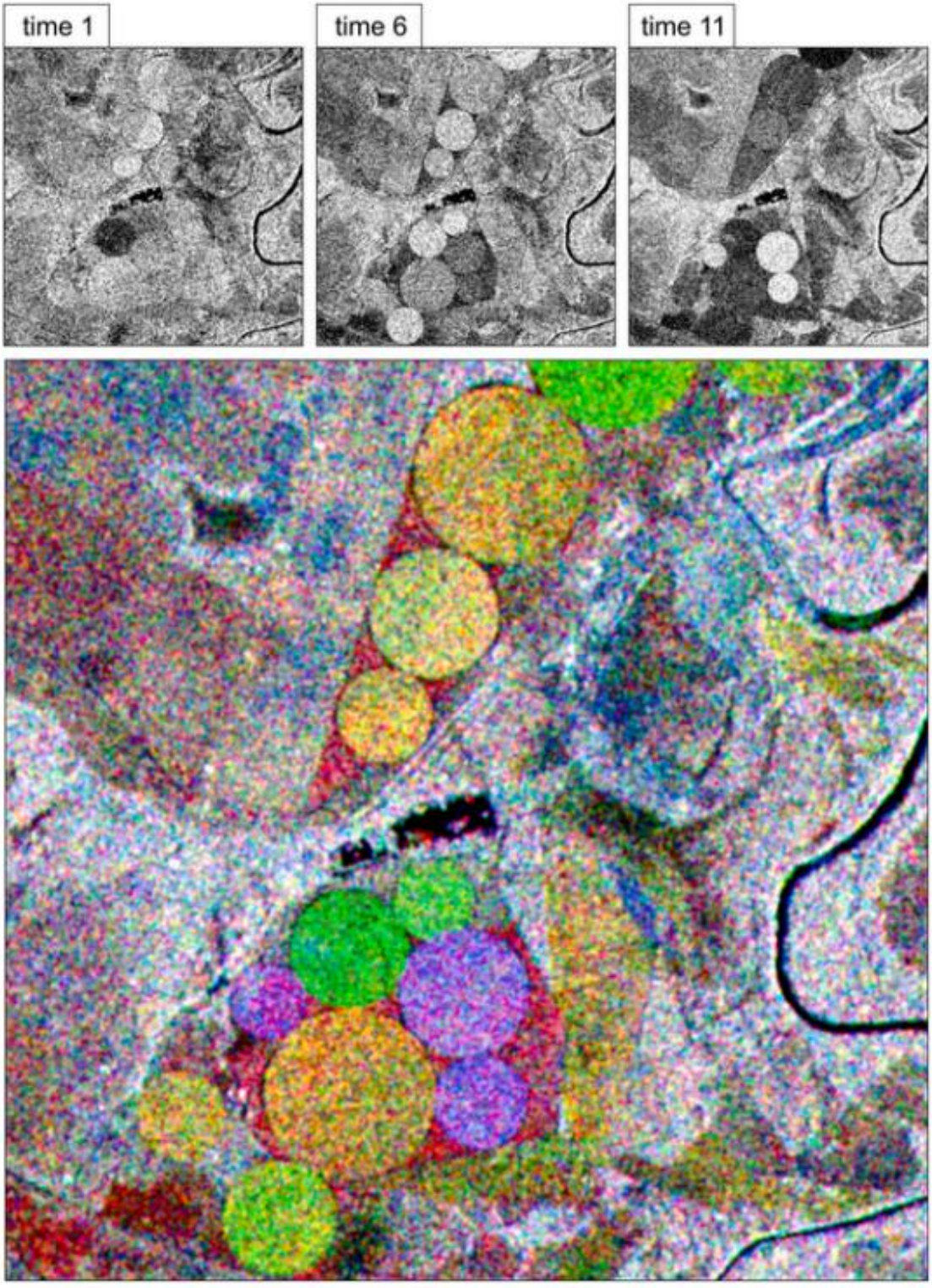

Figure III.4 Three-time frames (1, 6, and 11) and their corresponding RGB composition, in which the targets become much more visible.

2.1.4. Data split

The original and GT images have 20262x19657 pixels, which is too large. Thus, we developed a program that crops tiles with a size of our choice and simultaneously creates a

JSON file in the COCO annotation format. The program requires three files: (1) the original image; (2) the GT image; and (3) a shapefile containing points in the original image as the center of the crop. The manual choice of shapefile points considered the three different files (training, validation, and testing). When executing the program, it generates cropped tiles from the image, ground truth, and a JSON file in the COCO annotation format compatible with the Detectron2 software. In this research, we chose crops with sizes of 512x512 pixels. **Table III.1** lists the number of images and instances used in the training, validation, and test sets.

Table III-1 Data split in training (Train), validation (Val), and testing (Test) sets, with the respective number of512x512 frames (Number of images), and instances (Number of instances).

	# images	# instances
Train	534	5318
Val	151	1660
Test	138	1500

III.2.2 Model configurations

III.2.2.1 Mask-RCNN

The Mask R–CNN (**Figure III.5**) (He et al., 2017) has three objectives: (1) generate bounding boxes for each object; (2) classify each bounding box; and (3) generate a segmentation mask on the objects of interest. The method is an evolution from Faster-RCNN (Girshick, 2015), with an additional branch for segmentation for each region of interest (ROI). The algorithm uses a CNN to extract features from the input image, allowing to explore architectures with different complexity (e.g., ResNets (He et al., 2016), ResNeXt (Xie et al., 2017)), depths, (e.g., 34 layers, 50 layers, 101 layers), and scale resolutions (e.g., FPN (Lin et al., 2017)).

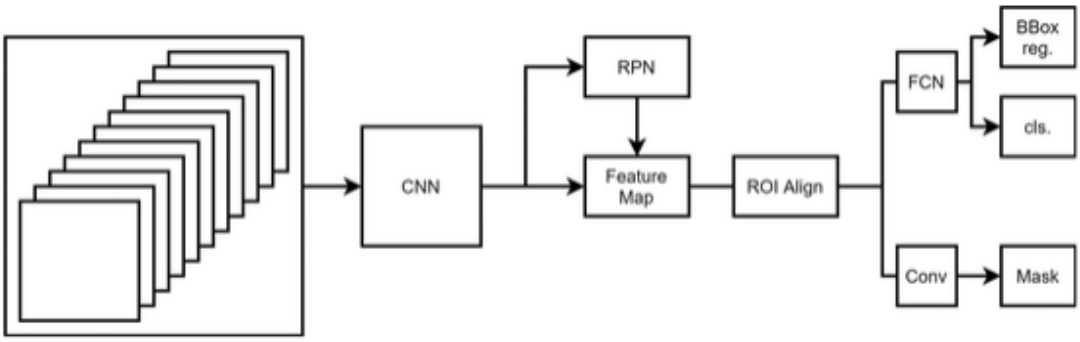

Figure III.5 Mask-RCNN architecture.

With the feature maps, a region proposal network (RPN) proposes bounding boxes in strategic regions. The generated bounding boxes on the feature maps pass through an ROI align process to maintain spatial cohesion in the image, and from the ROI align, the architecture divides into two branches: (1) fully connected layers for classes and bounding box regression; and (2) convolutional layers for segmentation mask.

The algorithm uses a loss function that is the sum of the three losses for each objective:

$$Total\ Loss = classification_{loss} + bounding\ box_{loss} + mask_{loss}$$

In which

$classification_{loss}$ and $mask_{loss}$: cross-entropy loss;

$bounding\ box_{loss}$: L1 loss.

III.2.2.2 Software adaptation

Detectron2 (Wu et al., 2019) is currently one of the best software for object detection and instance segmentation, proposed by Facebook Artificial Intelligence Research (FAIR). The software uses the Pytorch framework. Despite the high efficiency, there are some adaptations for the application of remote sensing imagery, e.g., the original code use libraries that do not consider georeferenced data and have limitations for applying multichannel imagery in TIFF format. Thus, we applied changes similar to the proposed by de Carvalho et al. (2021).

III.2.2.3 Configurations

Table III.2 lists the hyperparameters and configurations used in the Detectron2 software (elements not listed remained as default). Image processing used Nvidia GeForce RTX 2080 TI GPU with 11 GB memory and z-score normalization for a faster converging process separately for the VV and VH configurations:

$$z = \frac{x - \mu}{\sigma}$$

In which:

z: the standardized pixel value; x: the actual pixel value;

μ: the average pixel value among the entire sample;

σ: the standard deviation among the entire sample.

Table III-2 . Detectron2 configurations.

Parameters/configurations	Values
μ (VV)	-16.93, -17.07, -17.22, -17.73, -18.26, -18.49, -18.96, -19.36, -19.80, -19.93, -20.15
μ (VH)	-10.18, -10.42, -10.52, -11.07, -11.46, -11.65, -12.08, -12.40, -12.57, -12.73, -12.84
σ (VV)	3.11, 3.24, 3.33, 3.56, 3.69, 3.89, 4.15, 4.16, 4.52, 4.64, 4.75
σ (VH)	2.94, 3.02, 3.18, 3.26, 3.31, 3.34, 3.46, 3.47, 3.50, 3.56, 3.70
Anchor sizes	[8, 12, 16, 24, 32, 64, 128, 256]
number of iterations	3000
warmup iterations	500
Learning rate	0.001
Gamma	0.01
Evaluation steps	500
ROIS per image	128
Images per batch	1
freeze at	0
Pretrained weights	Imagenet (Deng et al., 2009)
Backbone	ResNeXt-101-32x8d (X-101)
Augmentations	Random vertical flip, random horizontal flip, random rotation

III.2.3 Model evaluation

The bounding boxes on object detection and instance segmentation tasks may result in three categories: (1) true positives (TP) (correct predictions), (2) false positives(FP) (wrong prediction), and (3) false negative (FN) (missing prediction). From these categories, we calculated precision (P) and recall (R):

$$P = \frac{TP}{TP + \mathrm{FP}},$$
$$R = \frac{TP}{TP + \mathrm{FN}}.$$

The P informs how many predictions were correct among all the predictions made, and the R how many predictions were correct among all elements supposed to have a prediction. From those two metrics, we may also obtain the average precision (AP):

$$AP = \int_0^1 P(R)dR.$$

The AP is also known as the area under the precision-recall curve. Nonetheless, these metrics do not consider the quality of the bounding box. Thus, many algorithms also consider the intersection over union (IoU):

$$IoU = \frac{Area\ of\ Overlap}{Area\ of\ Union}$$

The IoU enables the analyses of how well overlapped the predictions are (0 is no overlap, and 1 is perfect overlap). In this regard, COCO metrics (Lin et al., 2014) are the most common approaches, in which the COCO AP is the main metric for evaluation. The COCO AP score considers 10 IoU thresholds, starting at 0.5 up to 0.95 with 0.05 steps (0.50: 0.05: 0.95). Secondary metrics AP_{50}, AP_{75}, AP_{small} , AP_{medium}, and AP_{large}. AP_{50} and AP_{75} metrics use a single IoU value, which brings good insights into how the model considers a permissive and a stricter threshold. AP_{small} , AP_{medium}, and AP_{large} consider the target sizes. COCO defines the sizes considering the number of pixels of each object in three categories: (1) small object (area < 32^2 pixels); (2) medium object (32^2 pixels < area < 96^2 pixels); and (3) large object (area > 96^2 pixels).

III.2.4 Mosaicking and scene analysis

The images used in the model evaluation had 512x512-pixel spatial dimensions, which is far from the size of remote sensing images. Thus, a way to solve this problem is to apply mosaicking using sliding windows. However, merely applying mosaicking of consecutive frames is not enough to prevent the errors since adjacent frames may present errors located on their edges. **Figure III.6** shows the three possible errors due to border effects, in which: (A) adjacent frames horizontally; (B) adjacent frames vertically; and (C) adjacent frames horizontal and vertical wise. Therefore, we applied a sliding window with four stages (Carvalho et al., 2021): (1) base application (classifies all elements even if partially) considering adjacent frames (x_{start} = 0, y_{start} = 0, step = 512); (2) adjacent vertical classification (x_{start} = 256, y_{start} = 0, step = 512); adjacent horizontal classification (x_{start} = 0, y_{start} = 256, step = 512); and double edge classification (x_{start} = 256, y_{start} = 256, step = 512).

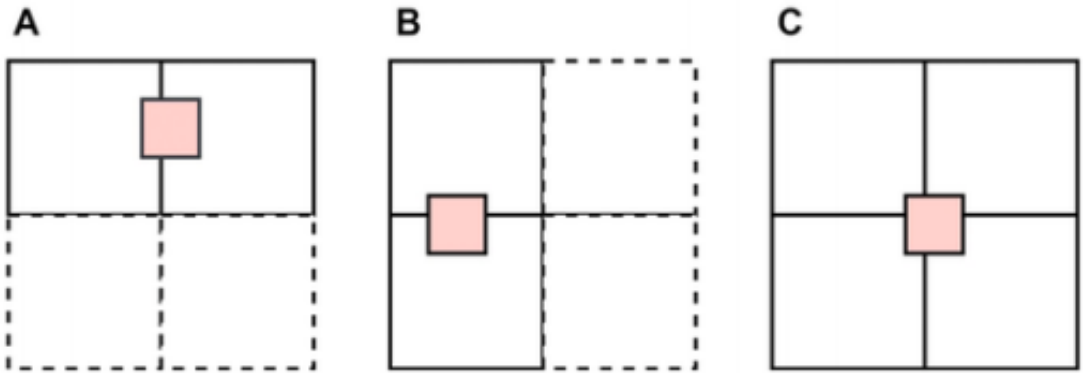

Figure III.6 The three scenarios that provide additional errors.

Only the base classification needs to classify all elements to avoid excessive and

unnecessary computational cost. The other three classifications on adjacent frames consider only elements in the borders. Furthermore, each classification at the edges can have multiple predictions (for example, two from two consecutive frames and one for the entire object classification). The best prediction selection considers the largest bounding box using a non-maximum suppression algorithm sorted by area. The algorithm considers overlapping bounding boxes and eliminates the smaller boxes, remaining only with the most extensive and correct prediction. This robust mosaicking procedure establishes a correct instance segmentation in a large-scale study area

III.3 Results

III.*3.1. Metric evaluation*

Table III.3 lists the COCO metrics results (AP, AP50, AP75, APs, APm, APl) using the X-101 backbone for bounding boxes and masks for the VV, VH, and VV+VH polarizations. The best results for VV, VH, and VV+VH are marked in green, terracotta, and blue, respectively. The VV+VH combination presented the highest value in all metrics apart from APsmall, in which VV consistently presented better results than VH, showing that using both images may not benefit the VV+VH model. Despite the better results, VV+VH presents higher computational cost when compared to VV and VH alone since they use two channels for each temporal frame.

Table III-3 Box Metrics and Mask metrics regarding AP, AP50, AP75, APs, APm, and AP large

for VV, VH and VV+VH images, considering 1 to 11 temporal images.

#t	Type	Box						Mask					
		AP	AP_{50}	AP_{75}	AP_s	AP_m	AP_l	AP	AP_{50}	AP_{75}	AP_s	AP_m	AP_l
1	VV	55.05	73.53	62.80	11.87	54.26	72.37	54.92	73.10	62.72	10.62	53.25	74.04
	VH	48.15	69.33	57.12	6.97	46.82	65.99	48.61	69.21	57.07	6.01	46.38	68.82
	VVVH	60.21	79.92	69.98	15.05	60.66	75.88	60.70	79.48	70.55	14.44	60.90	77.23
2	VV	62.92	82.22	74.26	16.66	63.87	78.01	63.78	82.42	73.75	14.49	64.42	80.53
	VH	58.40	78.79	67.71	10.22	58.54	75.87	58.52	78.85	67.79	9.01	58.20	78.22
	VVVH	66.71	85.34	77.89	20.70	67.79	81.04	66.95	84.94	78.01	18.19	67.81	87.73
3	VV	68.72	86.29	79.83	22.08	69.87	82.84	69.33	86.61	79.43	20.28	70.07	85.03
	VH	65.26	83.16	76.11	17.39	65.87	80.77	65.87	83.20	76.75	15.91	66.20	82.73
	VVVH	68.84	85.73	80.34	21.95	70.40	83.23	69.86	85.59	79.75	21.19	71.01	85.63
4	VV	70.59	88.10	81.98	23.06	72.35	84.33	70.80	88.23	81.83	22.04	72.04	86.10
	VH	67.53	85.15	78.63	18.36	68.54	82.96	67.78	85.14	78.31	15.59	68.47	85.06
	VVVH	69.64	87.15	81.36	20.20	71.31	83.56	70.75	87.23	81.27	19.26	71.90	86.68
5	VV	70.61	88.91	83.45	24.37	72.32	83.41	71.44	88.99	82.77	22.90	72.60	86.45
	VH	69.68	87.11	81.00	20.93	71.20	84.90	69.49	87.06	81.15	19.73	70.53	86.38
	VVVH	72.93	89.48	84.23	24.97	75.08	85.84	73.96	89.86	85.040	23.98	75.57	88.95
6	VV	72.94	90.17	84.03	26.57	75.18	85.06	73.26	89.64	83.43	26.27	74.98	86.92
	VH	71.69	89.47	83.59	24.93	72.74	85.89	72.30	89.56	82.68	23.36	73.29	87.37
	VVVH	72.77	90.49	84.81	26.92	74.46	86.35	73.37	90.08	84.86	25.54	74.73	88.71
7	VV	74.36	90.66	85.08	32.71	75.22	86.77	75.25	90.72	85.97	31.53	75.86	88.42
	VH	72.05	89.20	82.80	25.01	73.74	85.07	72.70	89.48	83.25	24.47	74.16	86.68
	VVVH	74.74	90.87	85.19	31.97	76.47	86.87	75.56	91.03	85.92	30.20	76.81	89.66
8	VV	74.62	91.00	86.39	**33.21**	76.63	85.11	74.85	91.17	85.98	30.96	76.30	86.97
	VH	73.22	90.39	84.36	29.13	74.47	85.47	74.02	90.60	83.75	27.66	74.86	87.90
	VVVH	74.29	91.49	86.07	31.04	75.82	86.76	75.09	90.98	85.85	30.29	76.39	88.69
9	VV	74.05	90.58	85.53	30.55	75.76	86.51	74.86	90.67	85.73	29.44	76.12	88.60
	VH	73.27	90.35	84.62	29.85	74.73	85.32	73.73	89.84	83.70	28.16	74.92	87.21
	VVVH	**75.32**	91.19	86.46	33.04	76.83	87.19	76.00	91.32	85.87	31.48	77.37	89.24
10	VV	73.35	91.17	85.74	33.00	74.63	85.36	74.05	90.72	85.41	30.45	75.26	87.69
	VH	74.66	90.95	85.36	29.45	76.08	86.99	75.02	91.12	84.77	27.82	76.09	89.33
	VVVH	74.34	91.22	**86.62**	31.84	75.58	86.62	75.28	91.45	86.14	30.99	76.338	89.17
11	VV	73.90	90.83	85.42	32.09	75.28	86.37	74.64	90.91	85.42	32.40	75.53	88.87
	VH	74.32	90.59	85.71	29.64	75.92	86.59	74.40	90.77	85.67	28.46	75.56	88.40
	VVVH	75.10	**91.83**	86.38	32.80	**76.93**	**87.72**	**76.05**	**91.81**	**86.82**	**32.44**	**77.53**	**89.65**

The most significant performance increase occurs between 1 and 2 temporal frames, with a difference of 7% (VV), 10% (VH), and 6% (VV+VH) in the AP metric. The values progressively increase afterward with smaller differences. The best AP values occur with a different number of temporal images for the VV (eight), VH (ten), and VV+VH (nine) time series. In the COCO's primary metric (AP), the distinctions between the best VV+VH, VV, and VH results are less than 1%, reaching minimal differences (0.04%) when comparing VV and VH. The best model choice requires a more in-depth analysis of factors, such as computational

cost and better metrics. VV polarization images have a lower computational cost due to fewer image requests to obtain similar results, providing a slight advantage over VH and a considerable improvement over VV+VH. However, VV+VH images represent a more appropriate choice considering the predictive power.

Regarding the IoU's, the AP50 showed results above 91% AP, demonstrating significant predictive power. The AP75 showed results above 85%, which is also a relevant result considering a more rigid IoU. Analysis of object sizes shows that smaller pivots have worse results than medium and large ones. The small object problem is relevant in the computer vision community, and the use of SAR images may be more difficult due to the noisy elements.

III.*3.2. Mosaicking results*

Figure III.7 shows the mosaicking results on a 2048x2048-pixel image (dimensions four times larger than the training procedure's images) using the VV+ VH polarization with nine temporal frames, considering: (1) the final prediction; (2) the final prediction with white background; (3) the deleted predictions; (4) the deleted predictions with white background; and three zoomed areas (A, B, and C) (54 deleted predictions).

The mosaicking presented no discontinuity on any parts of the mosaic, demonstrating great effectiveness of the method. Fig. 7A, B, and C show zoomed areas with corrections made by the algorithm horizontal-wise, vertical-wise, and horizontal and vertical-wise. **Table III.4** lists the characteristics of the CPISs: number, average size, median size, smallest, largest, and standard deviation. The selected area with dimensions 2048x2048 pixels presents 80 CPISs with high variability in sizes, ranging from 940 pixels to 15,405 pixels, expressed by a significant standard deviation value (4459.67).

Table III-4 Object information.

Pivot Count	Avg CPIS size	Median CPIS size	Smallest CPIS	Largest CPIS	Std CPIS
80	7,151 pixels	6,208 pixels	940 pixels	15,405 pixels	4459.67 pixels

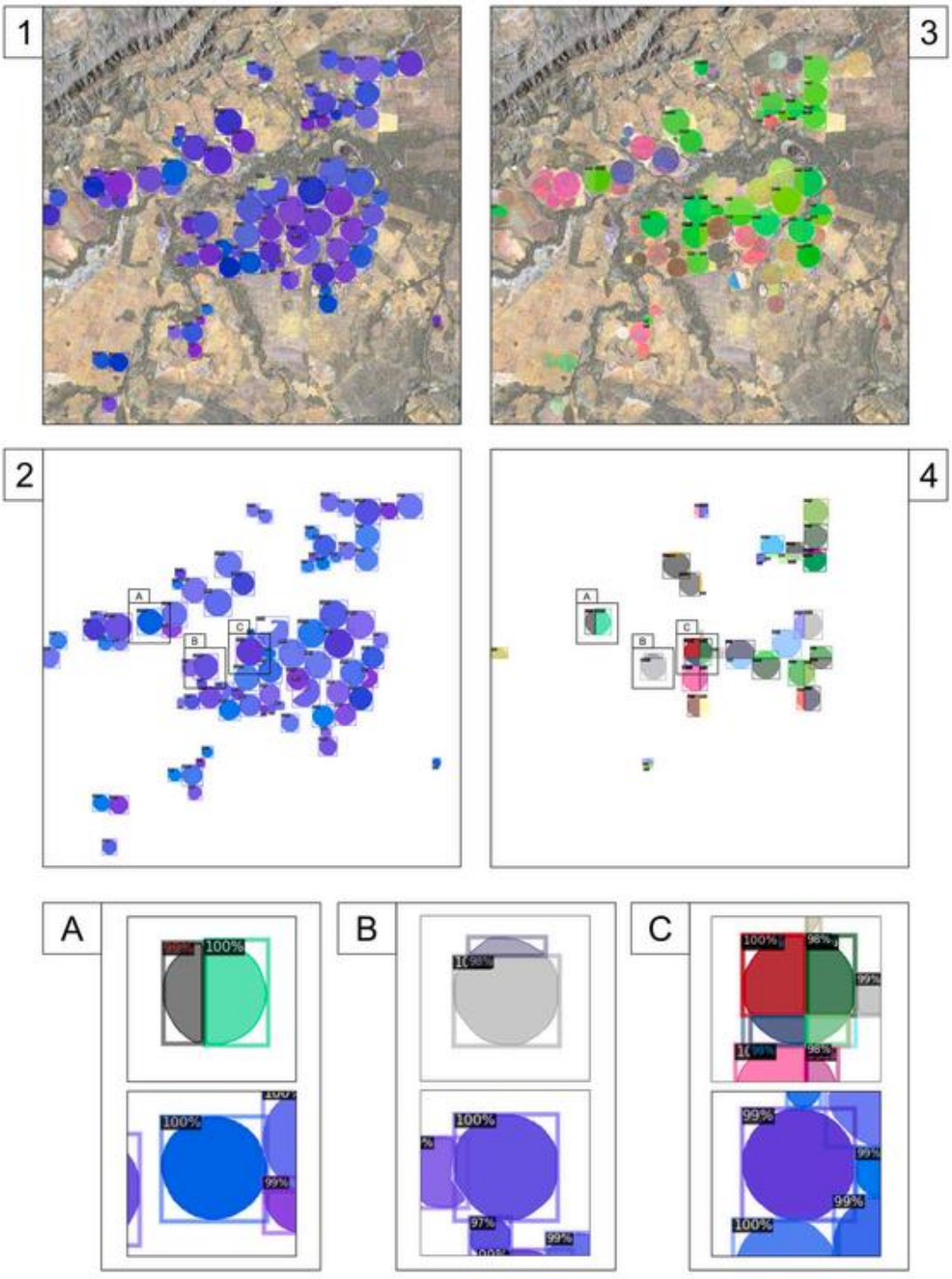

Figure III.7 Mosaic classification on VV + VH polarization with nine-time frames, where: (1) predicted image; (2) predicted image with white background; (3) deleted predictions; (4) deleted predictions with white background; and three zoomed areas (A, B, and C).

III.4 Discussion

In Brazil, CPIS mapping considers optical images' visual interpretation, causing problems resulting from the high volume of work and mapping's impossibility due to lack of a

cloudless image. This research seeks to solve these problems using SAR time series and DL methods for CPIS detection. In tropical regions, cloud cover occurs over long periods of the year, making SAR data the viable alternative for land use and land cover studies (La Rosa, 2019).

DL techniques achieve high precision prediction and fast results for image segmentation. However, DL applications in center pivot detection used only optical images, evidencing a gap with radar images. Zhang et al. (2018) were the pioneers in CPIS mapping with deep learning, using three-channel (RGB) images with dimensions of 34x34 pixels and an architecture based on LeNet. The investigation did not perform segmentation, only identified the center point of the CPIS from the variation-based approach, and demarcated a fixed-size square from this point. Nevertheless, there are more sophisticated methods. In semantic segmentation studies, Saraiva et al. (2020) used Planet imagery with four spectral bands in the Mato Grosso region, applying the traditional U-net architecture, achieving 99% precision 88% recall (pixel-wise). De Albuquerque et al. (2020) compared CPIS detection in the dry and rainy season using semantic segmentation from the three models (U-net, ResUnet, and Sharpmask). This research achieved 98% precision and 94% recall and highlighted that the dry season is easier to identify center pivots due to more considerable differences with the background. Tang et al. (2021a) combined the PVANET method and Hough transform to CPIS detection. Tang et al. (2021b) compared PVANET and YOLOv4 in the CPIS detection using Sentinel-2 True Color Image (TCI) added from edge detection images (Canny, Sobel, Laplacian, Holistically-Nested Edge Detection and Dense Extreme Inception Network for Edge Detection) to improve the performance. De Carvalho et al. (2021) proposed the first instance segmentation model for multi-channel imagery using Mask-RCNN using a center pivot dataset and Landsat imagery, reaching 77% AP and 92% AP50 using seven channels and 74% and 89% AP50 using three channels.

The high performance among the DL methods and places using optical imagery suggests studies about other limitations, such as clouds. The present research demonstrates that a multitemporal SAR image sequence enables discriminating the CPIS invariant shape and speckle noise reduction. The results had significant variations using only one image and a time series, increasing the AP values by more than 10%. This approach differs from other studies with SAR multitemporal images that focus on detecting change and phenological behaviors. Besides, the CPIS differs for other targets that do not have a defined shape over time, such as marine oil spills (Yekeen et al., 2020) or that move in the environment like ship and car

detection (Nie et al., 2020; Su et al., 2020; Wei et al., 2020). In our research, we obtained 3% less AP than de Carvalho et al. (2021), but only 1% less in AP50, showing that the results using SAR images present similar values, but with the advantage of being free clouds.

Mosaicking large scenes is a great interest in DL, especially when dealing with vast areas, such as agricultural fields. In this context, de Albuquerque et al. (2020) applied mosaicking using overlapping pixels in semantic segmentation tasks for center pivot detection, showing significant improvement when applying more overlapping pixels but a large increase in computational cost. Other works using semantic segmentation also provided overlapping pixels to attenuate border errors (Audebert et al., 2018). Besides, the instance segmentation mosaicking provided good results, as shown in other similar works (de Carvalho et al., 2021).

III.5 Conclusion

This research presents an innovative approach to CPIS detection using temporal SAR data and instance segmentation models. SAR images have the advantage of not containing clouds, which is a significant limitation in mapping the center pivot in a continental-size country such as Brazil. Studies of DL application in multitemporal SAR images mainly address phenological factors (for example, in agricultural studies) or change detection. Temporal SAR images as different channels in DL models demonstrated efficiency in CPIS detection with invariant shapes and high variation in backscatter values overtime. We evaluated the Detectron2 Mask-RCNN algorithm, which is one of the best currently using the X101 backbone. A single channel, which would be the traditional approach to detecting objects in SAR images, produced dramatically worse results than using more channels. Besides, we compared the VV, VH, and VV+VH polarizations, in which VV+VH presented the best metrics (75% AP, 91% AP50, and 86% AP75). The instance segmentation for individualizing the CPISs allows a quick calculation of the total number of units and area extraction, essential factors in territorial management. Nevertheless, the best model choice requires a more in-depth analysis of other vital issues present in practical applications (e.g., computational cost). In this regard, the VV image presented very close results (74%AP, 90%AP50, and 85%AP75), with much fewer channels. Also, we have proven that this algorithm is also appropriate in the classification of large images. Thus, we applied a mosaicking algorithm in an image with 2048x2048-pixel dimensions. This analysis provides useful insights such as counting and estimating the object areas, which is valuable for public managers and farmers, especially for automatic monitoring.

References

Agência Nacional de Águas (ANA). (2019). Levantamento da agricultura irrigada por pivôs centrais no Brasil (1985-2017). Agência Nacional de Águas (ANA), Brasília, Brasil.

Agência Nacional de Águas (ANA). (2016). Levantamento da Agricultura Irrigada por Pivôs Centrais no Brasil - 2014: *Relatório Síntese*. Agência Naciona de Águas (ANA): Brasília, Brasil, ISBN 978-85-8210-034-9.

Althoff, D., & Rodrigues, L. N. (2019). THE EXPANSION OF CENTER-PIVOT IRRIGATION IN THE CERRADO BIOME. *IRRIGA*, *1*(1), 56–61. https://doi.org/10.15809/irriga.2019v1n1p56-61

Audebert, N., Boulch, A., Randrianarivo, H., Le Saux, B., Ferecatu, M., Lefevre, S., & Marlet, R. (2017). Deep learning for urban remote sensing. *2017 Joint Urban Remote Sensing Event (JURSE)*, 1–4. https://doi.org/10.1109/JURSE.2017.7924536

Beltran-Peña, A., Rosa, L., & D'Odorico, P. (2020). Global food self-sufficiency in the 21st century under sustainable intensification of agriculture. *Environmental Research Letters*, *15*(9), 095004. https://doi.org/10.1088/1748-9326/ab9388

Cao, X., Wu, M., Zheng, Y., Guo, X., Chen, D., & Wang, W. (2018). Can China achieve food security through the development of irrigation? *Regional Environmental Change*, *18*(2), 465–475. https://doi.org/10.1007/s10113-017-1214-5

Carvalho, O. L. F. de, de Carvalho Júnior, O. A., Albuquerque, A. O. de, Bem, P. P. de, Silva, C. R., Ferreira, P. H. G., Moura, R. dos S. de, Gomes, R. A. T., Guimarães, R. F., & Borges, D. L. (2020). Instance Segmentation for Large, Multi-Channel Remote Sensing Imagery Using Mask-RCNN and a Mosaicking Approach. *Remote Sensing*, *13*(1), 39. https://doi.org/10.3390/rs13010039

Cui, B., Zhang, Y., Yan, L., Wei, J., & Wu, H. (2019). An Unsupervised SAR Change Detection Method Based on Stochastic Subspace Ensemble Learning. *Remote Sensing*, *11*(11), 1314. https://doi.org/10.3390/rs11111314

de Albuquerque, A. O., de Carvalho Júnior, O. A., Carvalho, O. L. F. de, de Bem, P. P., Ferreira, P. H. G., de Moura, R. dos S., Silva, C. R., Trancoso Gomes, R. A., & Fontes Guimarães, R. (2020). Deep Semantic Segmentation of Center Pivot Irrigation Systems from Remotely Sensed Data. *Remote Sensing*, *12*(13), 2159.

https://doi.org/10.3390/rs12132159

de Bem, P. P., de Carvalho Júnior, O. A., de Carvalho, O. L. F., Gomes, R. A. T., & Fontes Guimarães, R. (2020). Performance Analysis of Deep Convolutional Autoencoders with Different Patch Sizes for Change Detection from Burnt Areas. *Remote Sensing*, *12*(16), 2576. https://doi.org/10.3390/rs12162576

Carvalho, O. L. F. de, de Carvalho Júnior, O. A., Albuquerque, A. O. de, Bem, P. P. de, Silva, C. R., Ferreira, P. H. G., Moura, R. dos S. de, Gomes, R. A. T., Guimarães, R. F., & Borges, D. L. (2020). Instance Segmentation for Large, Multi-Channel Remote Sensing Imagery Using Mask-RCNN and a Mosaicking Approach. *Remote Sensing*, *13*(1), 39. https://doi.org/10.3390/rs13010039

Crisóstomo de Castro Filho, H., Abílio de Carvalho Júnior, O., Ferreira de Carvalho, O. L., Pozzobon de Bem, P., dos Santos de Moura, R., Olino de Albuquerque, A., Rosa Silva, C., Guimarães Ferreira, P. H., Fontes Guimarães, R., & Trancoso Gomes, R. A. (2020). Rice Crop Detection Using LSTM, Bi-LSTM, and Machine Learning Models from Sentinel-1 Time Series. *Remote Sensing*, *12*(16), 2655. https://doi.org/10.3390/rs12162655

Deng, J., Dong, W., Socher, R., Li, L.-J., Kai Li, & Li Fei-Fei. (2009). ImageNet: A large-scale hierarchical image database. *2009 IEEE Conference on Computer Vision and Pattern Recognition*, 248–255. https://doi.org/10.1109/CVPR.2009.5206848

Feng, Q., Yang, J., Zhu, D., Liu, J., Guo, H., Bayartungalag, B., & Li, B. (2019). Integrating Multitemporal Sentinel-1/2 Data for Coastal Land Cover Classification Using a Multibranch Convolutional Neural Network: A Case of the Yellow River Delta. *Remote Sensing*, *11*(9), 1006. https://doi.org/10.3390/rs11091006

Filipponi, F. (2019). Sentinel-1 GRD Preprocessing Workflow. *3rd International Electronic Conference on Remote Sensing*, 11. https://doi.org/10.3390/ECRS-3-06201

He, K., Zhang, X., Ren, S., & Sun, J. (2016). Deep Residual Learning for Image Recognition. *2016 IEEE Conference on Computer Vision and Pattern Recognition (CVPR)*, 770–778. https://doi.org/10.1109/CVPR.2016.90

Foley, J. A., Ramankutty, N., Brauman, K. A., Cassidy, E. S., Gerber, J. S., Johnston, M., Mueller, N. D., O'Connell, C., Ray, D. K., West, P. C., Balzer, C., Bennett, E. M., Carpenter, S. R., Hill, J., Monfreda, C., Polasky, S., Rockström, J., Sheehan, J., Siebert,

S., … Zaks, D. P. M. (2011). Solutions for a cultivated planet. *Nature*, *478*(7369), 337–342. https://doi.org/10.1038/nature10452

Gao, F., Liu, X., Dong, J., Zhong, G., & Jian, M. (2017). Change Detection in SAR Images Based on Deep Semi-NMF and SVD Networks. *Remote Sensing*, *9*(5), 435. https://doi.org/10.3390/rs9050435

Gebbers, R., & Adamchuk, V. I. (2010). Precision Agriculture and Food Security. *Science*, *327*(5967), 828–831. https://doi.org/10.1126/science.1183899

Girshick, R. (2015). Fast R-CNN. *2015 IEEE International Conference on Computer Vision (ICCV)*, 1440–1448. https://doi.org/10.1109/ICCV.2015.169

Godfray, H. C. J., Beddington, J. R., Crute, I. R., Haddad, L., Lawrence, D., Muir, J. F., Pretty, J., Robinson, S., Thomas, S. M., & Toulmin, C. (2010). Food Security: The Challenge of Feeding 9 Billion People. *Science*, *327*(5967), 812–818. https://doi.org/10.1126/science.1185383

He, K., Gkioxari, G., Dollar, P., & Girshick, R. (2017). Mask R-CNN. *2017 IEEE International Conference on Computer Vision (ICCV)*, 2980–2988. https://doi.org/10.1109/ICCV.2017.322

Heller, R. C., & Johnson, K. A. (1979). Estimating irrigated land acreage from Landsat imagery. *Photogrammetric Engineering and Remote Sensing*, *45*(10), 1379–1386.

Iino, S., Ito, R., Doi, K., Imaizumi, T., & Hikosaka, S. (2018). CNN-based generation of high-accuracy urban distribution maps utilising SAR satellite imagery for short-term change monitoring. *International Journal of Image and Data Fusion*, *9*(4), 302–318. https://doi.org/10.1080/19479832.2018.1491897

Jaturapitpornchai, R., Rattanasuwan, P., Matsuoka, M., & Nakamura, R. (2020). CORN: An Alternative Way to Utilize Time-Series Data of SAR Images in Newly Built Construction Detection. *Remote Sensing*, *12*(6), 990. https://doi.org/10.3390/rs12060990

Jo, H.-W., Lee, S., Park, E., Lim, C.-H., Song, C., Lee, H., Ko, Y., Cha, S., Yoon, H., & Lee, W.-K. (2020). Deep Learning Applications on Multitemporal SAR (Sentinel-1) Image Classification Using Confined Labeled Data: The Case of Detecting Rice Paddy in South Korea. *IEEE Transactions on Geoscience and Remote Sensing*, *58*(11), 7589–7601. https://doi.org/10.1109/TGRS.2020.2981671

LeCun, Y., Bengio, Y., & Hinton, G. (2015). Deep learning. *Nature*, *521*(7553), 436–444.

https://doi.org/10.1038/nature14539

Li, W., Liu, H., Wang, Y., Li, Z., Jia, Y., & Gui, G. (2019). Deep Learning-Based Classification Methods for Remote Sensing Images in Urban Built-Up Areas. *IEEE Access*, *7*, 36274–36284. https://doi.org/10.1109/ACCESS.2019.2903127

Liao, C., Wang, J., Xie, Q., Baz, A. Al, Huang, X., Shang, J., & He, Y. (2020). Synergistic Use of Multi-Temporal RADARSAT-2 and VENμS Data for Crop Classification Based on 1D Convolutional Neural Network. *Remote Sensing*, *12*(5), 832. https://doi.org/10.3390/rs12050832

Lin, T.-Y., Dollar, P., Girshick, R., He, K., Hariharan, B., & Belongie, S. (2017). Feature Pyramid Networks for Object Detection. *2017 IEEE Conference on Computer Vision and Pattern Recognition (CVPR)*, 936–944. https://doi.org/10.1109/CVPR.2017.106

Lin, T.-Y., Maire, M., Belongie, S., Hays, J., Perona, P., Ramanan, D., Dollár, P., & Zitnick, C. L. (2014). *Microsoft COCO: Common Objects in Context* (pp. 740–755). https://doi.org/10.1007/978-3-319-10602-1_48

Liu, T., Li, Y., Cao, Y., & Shen, Q. (2017). Change detection in multitemporal synthetic aperture radar images using dual-channel convolutional neural network. *Journal of Applied Remote Sensing*, *11*(04), 1. https://doi.org/10.1117/1.JRS.11.042615

Luo, B., Hu, C., Su, X., & Wang, Y. (2019). Differentially Deep Subspace Representation for Unsupervised Change Detection of SAR Images. *Remote Sensing*, *11*(23), 2740. https://doi.org/10.3390/rs11232740

Ma, L., Liu, Y., Zhang, X., Ye, Y., Yin, G., & Johnson, B. A. (2019). Deep learning in remote sensing applications: A meta-analysis and review. *ISPRS Journal of Photogrammetry and Remote Sensing*, *152*, 166–177. https://doi.org/10.1016/j.isprsjprs.2019.04.015

Ndikumana, E., Ho Tong Minh, D., Baghdadi, N., Courault, D., & Hossard, L. (2018). Deep Recurrent Neural Network for Agricultural Classification using multitemporal SAR Sentinel-1 for Camargue, France. *Remote Sensing*, *10*(8), 1217. https://doi.org/10.3390/rs10081217

Nie, X., Duan, M., Ding, H., Hu, B., & Wong, E. K. (2020). Attention Mask R-CNN for Ship Detection and Segmentation From Remote Sensing Images. *IEEE Access*, *8*, 9325–9334. https://doi.org/10.1109/ACCESS.2020.2964540

ONU Department of Economic and Social Affairs, 2019. World Population Prospects 2019,

World Population Prospects 2019: Highlights 2019 (ST/ESA/SER. A/423). United Nations, Department of Economic and Social Affairs, Population Division, New York, NY, USA.

Pollice, F., Albanese, V., & Urso, G. (2018). *Food Security: A Challenge for a Global Governance* (pp. 217–227). https://doi.org/10.1007/978-3-319-75196-2_13

Pousa, R., Costa, M. H., Pimenta, F. M., Fontes, V. C., Brito, V. F. A. de, & Castro, M. (2019). Climate Change and Intense Irrigation Growth in Western Bahia, Brazil: The Urgent Need for Hydroclimatic Monitoring. *Water*, *11*(5), 933. https://doi.org/10.3390/w11050933

Rosa, L., Chiarelli, D. D., Rulli, M. C., Dell'Angelo, J., & D'Odorico, P. (2020). Global agricultural economic water scarcity. *Science Advances*, *6*(18). https://doi.org/10.1126/sciadv.aaz6031

Rundquist, D.C., Hoffman, R.O., Carlson, M.P., Cook, A.E. (1989). Nebraska center-pivot inventory: an example of operational satellite remote sensing on a long-term basis. *Photogramm. Eng. Rem. Sens*. 55, 587-590.

Saraiva, M., Protas, É., Salgado, M., & Souza, C. (2020). Automatic Mapping of Center Pivot Irrigation Systems from Satellite Images Using Deep Learning. *Remote Sensing*, *12*(3), 558. https://doi.org/10.3390/rs12030558

Siebert, S., & Döll, P. (2010). Quantifying blue and green virtual water contents in global crop production as well as potential production losses without irrigation. *Journal of Hydrology*, *384*(3–4), 198–217. https://doi.org/10.1016/j.jhydrol.2009.07.031

Su, H., Wei, S., Liu, S., Liang, J., Wang, C., Shi, J., & Zhang, X. (2020). HQ-ISNet: High-Quality Instance Segmentation for Remote Sensing Imagery. *Remote Sensing*, *12*(6), 989. https://doi.org/10.3390/rs12060989

Tang, J., Arvor, D., Corpetti, T., & Tang, P. (2021). Mapping Center Pivot Irrigation Systems in the Southern Amazon from Sentinel-2 Images. *Water*, *13*(3), 298. https://doi.org/10.3390/w13030298

Tang, J., Zhang, Z., Zhao, L., & Tang, P. (2021). Increasing Shape Bias to Improve the Precision of Center Pivot Irrigation System Detection. *Remote Sensing*, *13*(4), 612. https://doi.org/10.3390/rs13040612

Tilman, D., Balzer, C., Hill, J., & Befort, B. L. (2011). Global food demand and the sustainable intensification of agriculture. *Proceedings of the National Academy of Sciences*, *108*(50),

20260–20264. https://doi.org/10.1073/pnas.1116437108

Wei, S., Zeng, X., Qu, Q., Wang, M., Su, H., & Shi, J. (2020). HRSID: A High-Resolution SAR Images Dataset for Ship Detection and Instance Segmentation. *IEEE Access*, *8*, 120234–120254. https://doi.org/10.1109/ACCESS.2020.3005861

Y. Wu A. Kirillov F. Massa W.-Y. (2019). Girshick Detectron2 [WWW document] https://github.com/facebookresearch/detectron2. S3 march 2021.

Xie, S., Girshick, R., Dollar, P., Tu, Z., & He, K. (2017). Aggregated Residual Transformations for Deep Neural Networks. *2017 IEEE Conference on Computer Vision and Pattern Recognition (CVPR)*, 5987–5995. https://doi.org/10.1109/CVPR.2017.634

Temitope Yekeen, S., Balogun, A., & Wan Yusof, K. B. (2020). A novel deep learning instance segmentation model for automated marine oil spill detection. *ISPRS Journal of Photogrammetry and Remote Sensing*, *167*, 190–200. https://doi.org/10.1016/j.isprsjprs.2020.07.011

Yi, Y., Zhang, Z., Zhang, W., Zhang, C., Li, W., & Zhao, T. (2019). Semantic Segmentation of Urban Buildings from VHR Remote Sensing Imagery Using a Deep Convolutional Neural Network. *Remote Sensing*, *11*(15), 1774. https://doi.org/10.3390/rs11151774

Zhang, C., Yue, P., Di, L., & Wu, Z. (2018). Automatic Identification of Center Pivot Irrigation Systems from Landsat Images Using Convolutional Neural Networks. *Agriculture*, *8*(10), 147. https://doi.org/10.3390/agriculture8100147

Zhang, X., Liu, G., Zhang, C., Atkinson, P. M., Tan, X., Jian, X., Zhou, X., & Li, Y. (2020). Two-Phase Object-Based Deep Learning for Multi-Temporal SAR Image Change Detection. *Remote Sensing*, *12*(3), 548. https://doi.org/10.3390/rs12030548

CAPÍTULO

IV. DEALING WITH CLOUDS AND SEASONAL CHANGES FOR CENTER PIVOT IRRIGATION SYSTEMS DETECTION USING INSTANCE SEGMENTATION IN SENTINEL-2 TIME SERIES

Resumo

A detecção automática de Sistemas de Irrigação por Pivô Central (SIPC) é fundamental para o estabelecimento de políticas públicas, principalmente em países com perspectiva de crescimento dessa tecnologia, como o Brasil. Estudos anteriores para detectar SIPC usando *Deep Learning* (DL) usaram imagens ópticas de data única, contendo limitações devido a mudanças sazonais e cobertura de nuvens. Portanto, esta pesquisa teve como objetivo detectar CPIS utilizando imagens multitemporais Sentinel-2 (contendo seis datas) e segmentação de instâncias, considerando variações sazonais e diferentes proporções de imagens nubladas, generalizando os modelos para detectar SIPC em diversas situações. Usamos uma nova estratégia de aumento, na qual, para cada iteração, seis imagens foram selecionadas aleatoriamente da série temporal (de um total de 11 datas) em ordem aleatória. Avaliamos o modelo *Mask RCNN* com o *backbone* ResNext-101 considerando as métricas COCO em seis conjuntos de teste com diferentes proporções de imagens sem nuvens (<20%) e nubladas (> 75%), de 6 imagens sem nuvens e imagens nulas (6: 0) até uma imagem sem nuvens e cinco imagens nubladas (1: 5). Descobrimos que o uso de seis imagens sem nuvens forneceu as melhores métricas (80% de precisão média (AP), 93% AP50), mas os resultados foram semelhantes (74% AP, 88% AP50), mesmo em cenários extremos com presença de nuvem abundante (1: 5 Razão). Nosso método fornece uma maneira mais adaptativa e automática de mapear o SIPC a partir de séries temporais, reduzindo significativamente a interferência, como cobertura de nuvens, efeitos atmosféricos, sombra, dados ausentes e falta de contraste com a vegetação circundante.

Termos do Índice: Série Temporal, Nuvem, Mask R-CNN, Deep Learning.

Artigo publicado na revista *Journal of Selected Topics in Applied Earth Observations and Remote Sensing*, 2021. DOI: 10.1109/JSTARS.2021.3104726

Abstract

The automatic detection of Center Pivot Irrigation Systems (CPIS) is fundamental for establishing public policies, especially in countries with a growth perspective in this technology, like Brazil. Previous studies to detect CPIS using Deep Learning (DL) used single-date optical images, containing limitations due to seasonal changes and cloud cover. Therefore, this research aimed to detect CPIS using Sentinel-2 multitemporal images (containing six dates) and instance segmentation, considering seasonal variations and different proportions of cloudy images, generalizing the models to detect CPIS in diverse situations. We used a novel augmentation strategy, in which, for each iteration, six images were randomly selected from the time series (from a total of 11 dates) in random order. We evaluated the Mask-RCNN model with the ResNext-101 backbone considering the COCO metrics on six testing sets with different ratios of cloudless (< 20%) and cloudy images (> 75%), from 6 cloudless images and zero cloudy images (6:0) up to one cloudless image and five cloudy images (1:5). We found that using six cloudless images provided the best metrics (80% Average Precision (AP), 93% AP50), but results were similar (74% AP, 88% AP50) even in extreme scenarios with abundant cloud presence (1:5 ratio). Our method provides a more adaptive and automatic way to map CPIS from time series, significantly reducing interference such as cloud cover, atmospheric effects, shadow, missing data, and lack of contrast with the surrounding vegetation.

Index Terms: Time Series, Cloud, Mask R-CNN, Deep Learning

IV.1 Introduction

Strategies for technological advances in agricultural production are essential to feed the world's growing population [1], [2]. The technology-driven intensification with the increase in yield (production/area) is a viable solution to guarantee world food security and avoid expanding agricultural regions over natural environments [3], [4], [5]. Among the intensification procedures, irrigation plays a fundamental role in increasing agricultural productivity and decreasing costs and manual labor, being essential for crops in arid and semiarid regions. Despite the benefits of irrigation for agriculture, it also negatively affects soil and water resources, such as reducing surface water and groundwater sources [6], [7], soil salinization [8], [9] erosion [10], [11] and ecological damage [12]. Besides, conflicts over water use increases, requiring governmental agencies to balance the diverse demands from hydroelectric production, irrigation, domestic and industrial use. In the context of fast-growing water demand in the agriculture, constant irrigated area monitoring is crucial to predict and minimize current and potential conflicts. The main alternative for assessing the spatial distribution and estimating irrigated areas is the remote sensing monitoring because of its speed, periodicity, cost-effectiveness, and reliable data acquisition. Therefore, consistent remote sensing information on irrigation areas contributes to water management, anticipating necessary changes and negative impacts.

Among the various irrigation systems, the Center Pivot Irrigation System (CPIS) is one of the most advanced techniques consisting of water sprinklers in a suspended structure along a radius that rotates throughout the circular area, ensuring a uniform water distribution in the crops. The main advantages of the CPIS are efficient water and energy consumption, less workforce, easy operation, long-distance irrigation, and application of different types of fertilizers.

CPIS is the predominant irrigation technology in Central Brazil (Cerrado biome) due to the favorable environmental conditions with extensive flat topography and surface and underground water availability. The Cerrado biome has aproximately 80% of all Brazilian CPIS [13]. However, the growing number of CPIS has led to intensified conflicts over water use and the need for governance of water resources [14]. In this context, the National Water Agency (ANA – Agência Nacional de Águas) performs the annual CPIS mapping based on remote sensing and visual interpretation images [15], [16]. In the quest to automate CPIS detection, methods based on Deep Learning (DL) have achieved results with metrics over 90% [17], [18], [19], [20]. This approach allows for several advantages such as lower costs, faster, and more

accurate surveying when compared to visual interpretation and traditional machine learning methods.

DL acts in solving problems in different areas of knowledge, including image, video, speech, and audio recognition [21]. Besides, DL models offers the opportunity to automate systems with high performance in processing large data sets by using computers with high storage and processing capacity and GPUs. Therefore, DL has promoted notable advances recently in the field of computer vision, allowing a high learning power of complex, subtle, and abstract representations directly from the data [22]. DL's extraordinary progress has had significant repercussions for the remote sensing community, with an expressive increase in the number of papers after 2014 [23]. In a short period, different review articles focused on DL in remote sensing, considering the different applications [24]; digital image processing (image fusion, image registration, classification, change detection, object detection, and segmentation) [23], [25], [26], [27], [28], [29]; environmental processes (land cover, vegetation parameters, agricultural yield prediction, air temperature, aerosol, particulate matter, precipitation, soil moisture, snow cover, evapotranspiration, radiation parameters, ocean color parameters) [30], status and perspectives [31], types of images (hyperspectral, multispectral, SAR, PolSAR, high spatial resolution, multimodal data fusion, 3-D reconstruction) [32], [33], [34], [35], [36].

Convolutional Neural Networks (CNNs)-based models lead remote sensing studies due to the impressive accuracy in object recognition [28]. The CNN application in remote sensing images is more complex than in traditional Red, Green, and Blue images. It requires geospatial systems, labeled data considering the different sensors and high image dimensionality (spatial, spectral, and temporal), clipping frames in specific sizes for training and segmentation, and image reconstruction procedure through sliding windows with overlapping pixels [37], [38].

There are three main difficulties associated with the mapping of center pivots using the optical image and deep learning: (1) seasonal planting variation that eventually merges with the surrounding areas (see **Figure IV.1**); (2) cloud cover that prevents the detection of the Earth's surface; and (3) large-scale automated processing. The previous studies for CPIS detection using DL on optical images considered a single time frame, requiring a specialist to identify the best dates in which the CPIS are more visible, and depending on the dates, the accuracy metrics may vary due to the seasonal changes which makes the CPIS very similar to their surroundings [18].

The present research aims to develop a procedure to annually inventory the center pivots using Sentinel-2 multitemporal images and a distinct semantic identification for each CPIS,

seeking to circumvent ambiguities due to the inter-annual variability in the crop stage and the presence of cloud cover or shadows. To this end, we developed a multitemporal database considering different planting stages and with different proportions of cloud cover. The control of the cloud-cover proportion used an algorithm that randomly introduced images with a high percentage of cloud cover in the time series. Therefore, the methodology assesses the learning ability of CNN architectures to detect targets without having complete information over time. Besides, the CNN model combined spatial-temporal–spectral information.

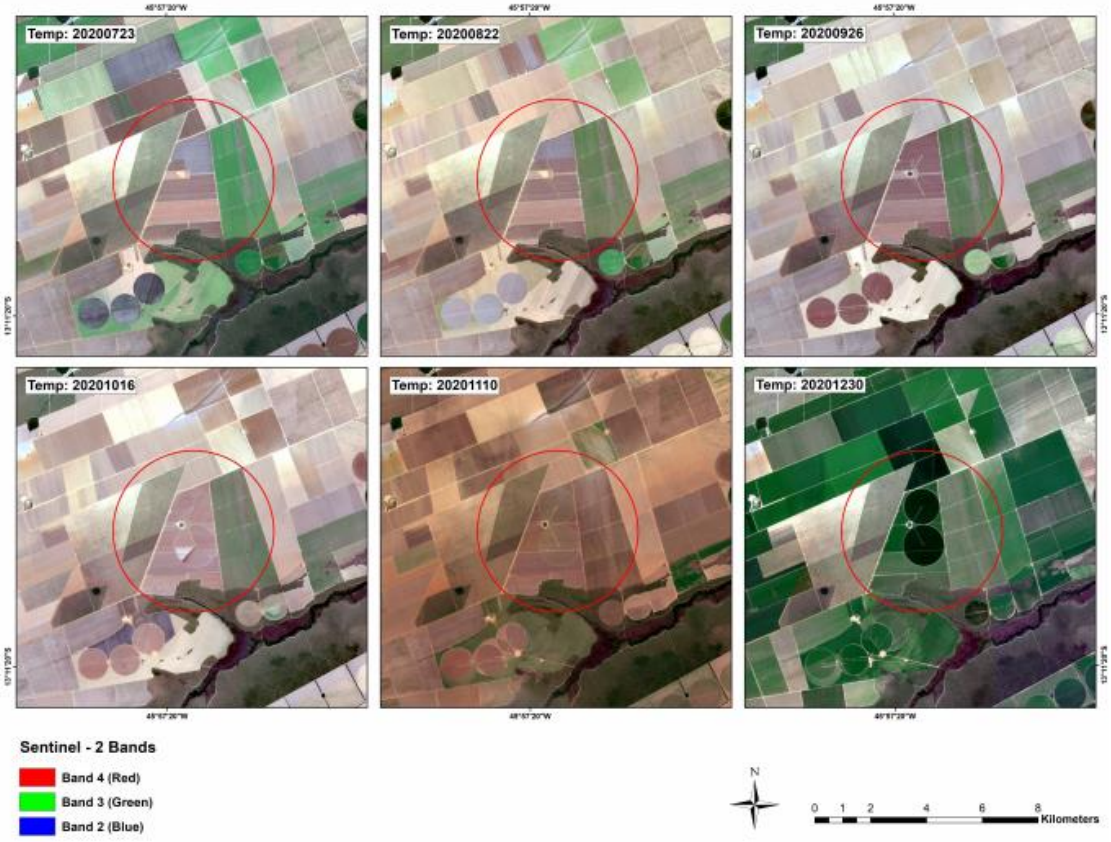

Figure IV.1 Representation of the seasonal variations among center pivots in a Sentinel-2 image using the Red, Green, and Blue spectral bands.

IV.2 Related Works

The governmental interest in CPIS's water and energy consumption and agricultural production caused an increase in remote sensing studies for their detection. Although the circular shape of the center pivot is very characteristic, its automatic detection has limitations for traditional image classification methods [39]. The CPIS do not have uniform spatial and temporal behavior internally, containing different plantings (with subdivision of the area or intercropped) and diversity for the surrounding CPIS (with different agricultural crops and crop

production cycles) [18]. These peculiarities make the pixel-based classifications considering the spectral response, vegetation indices, or temporal signatures very deficient. The inclusion of spatial attributes to consider center-pivot shape presents a challenge for remote sensing studies that have only recently been overcome. Therefore, different approaches to center pivot mapping by remote sensing have been used, such as (a) visual interpretation, (b) Hough transform, (c) Geographic object-based image analysis (GEOBIA), and (d) Deep Learning (DL) methods.

The first studies of CPIS mapping in the 70s and 80s used the visual interpretation of circular features [40], [41], which is still a widely used method [42], [43], [44], [45]. Despite the precise results with a visual interpretation, the process is laborious and time consuming.

Although the Hough Transform (HT) is a technique for automatically detecting circles, with a promising perspective for detecting center pivots, few studies are on its application [46], [19]. The main limitations of the HT method are complex parameter setting, low precision, long computational time, and difficulty in situations with incomplete circles [47], [20].

GEOBIA combines segmentation methods which partition images into objects and a set of rules that allow intuitive step-by-step classification. This object-based approach can have advantages over pixel-based approaches, incorporating spatial attributes derived from the object's shape, hierarchical multi-scale information, texture, and class-related characteristics [48], [49], [50]. The GEOBIA studies for detecting CPIS consider variations in the methodological sequence and attributes used [51], [52], [53]. Yan and Roy [52] established three stages in the mapping of center pivots using GEOBIA: (a) object-based approach (active geometric contour based on the variational region); (b) segmentation method (watershed algorithm); and (c) geometry-based algorithm to detect rectangular, circular, and irregularly shaped fields. Johansen et al. [51] describe four steps in center pivot detection: (a) generation of the annual maximum image of the Normalized Difference Vegetation Index (NDVI) and the annual panchromatic band, (b) segmentation, (c) classification using the shape such as the center pivot field length), length-width ratio, and elliptical adjustment; and (d) the rule-set definition.

However, several studies demonstrate an overall superiority of Deep Learning (DL) to GEOBIA regarding different factors: (a) greater precision and efficiency; (b) less human supervision; (c) reuse of knowledge due to the high capacity for transferability to other regions or scenarios considering the various attributes of the object (light, color, background, size, and shape); and (d) less interference by salt and pepper noise [54], [55], [56].

Recently, the CPIS has been a constant target for DL studies using Convolutional Neural Networks (CNN) with different approaches: (a) detection of the core point of the center pivot [47]; (b) object detection with the establishment of bounding boxes around CPIS [20], [57]; (c) semantic segmentation that performs a pixel-wise classification where all CPIS pixels receive a label [18], [58], [59]; and (d) instance segmentation that produces bounding boxes and pixel-wise segmentation masks on CPIS [17].

Among the CNNs-based models applied in CPIS, the instance segmentation approach is the most complex and advantageous. It allows extracting individual instance for each CPIS in an image and acquiring more information such as the total number of CPIS and area per unit. Besides, instance segmentation has a greater ability to separate overlapping objects of the same class. The most used instance segmentation methods are FCIS [60] and Mask-RCNN [61], which first performs the instance step and then performs the segmentation and classification in parallel.

In contrast to the above methods for center pivot detection, the proposed method searches greater discrimination of the center pivot by incorporating the temporal data to overcome the influences of the images altered by the cloud cover or periods of similar behavior between the pivot and the surrounding area.

IV.3 Materials and Methods

We applied the following methodology: (A) Study Area; (B) Image Acquisition; (C) Annotations; (D) Instance segmentation approach; and (E) large image classification.

IV.3.1 Study Area

The study areas are located in Central Brazil, containing the country's highest CPIS concentrations due to the flat terrain and water potential that allows mechanization and irrigation. The Central Brazil region is most used in studies with deep learning to CPIS detection (**Table IV.I**). The low rainfall between May and September prevents several crops, which becomes viable with irrigation. This research considered two main CPIS concentrations within Central Brazil: (a) Western Bahia and (b) region between the states of Minas Gerais and Goiás close to the Federal District (see **Figure IV.2**). Western Bahia presents a significant growth in mechanized agriculture [63], [64] and an intensification of center pivots, ranging from 9 in 1985 to 1550 in 2016 [65]. The Goiás/Minas Gerais region contains hundreds of CPIS, resulting in

an intensification of the water use conflicts due to the competition between irrigation, human consumption, and hydroelectric power generation [14].

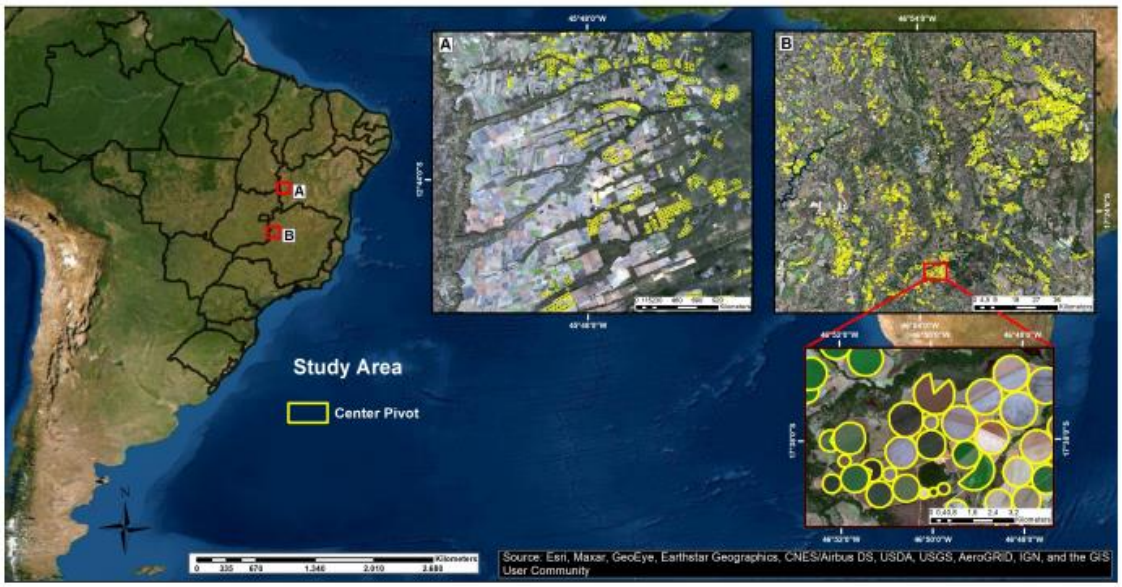

Figure IV.2 Study Area.

Table IV-1 Previous studies on Center Pivot Irrigation Systems Detection, and their corresponding region, satellite, method, model and bands.

Paper	Region	Satellite	Method	Model	Bands
[47]	Colorado, USA	TM-Landsat 5	Central point detection	LeNet-5, AlexNet, VGGNet	RGB
[58]	Central Brazil Texas, USA	PlanetScope	Semantic	U-Net	RGB-NIR
[59]	Duero, Spain South Africa	Sentinel-2	Semantic	U-Net	4 bands/ 3 PCAs
[19]	Central Brazil	Sentinel-2	object detection	PVANET-Hough	RGB
[20]	Central Brazil	Sentinel-2	object detection	PVANET, YOLOv4	RBG+filters
[18]	Central Brazil	Landsat-8	semantic	U-net, Deep ResUnet, SharpMask	7 bands
[17]	Central Brazil	Landsat-8	instance	Mask-RCNN (7 backbone structures)	RGB/7 bands
[62]	Central Brazil	Sentinel-1	instance	Mask-RCNN	Multitemporal (10 times)

IV.3.2 Image acquisition and time series construction

The Sentinel-2 mission developed by the European Space Agency (ESA) under the European Union's Copernicus program acquires high spatial resolution multispectral optical images [66]. This research uses images with 10m-spatial resolution corresponding to the spectral bands at 490 nm, 560nm, 665nm, and 842nm. The images acquired in Level 1C have radiometric processing and geometric correction. In the Sentinel Application Platform (SNAP) software developed by ESA, we carry out the pre-processing steps.

In order to assess the seasonal and cloud interference, the elaboration of the time series encompassed eleven different dates, considering the dry and rainy periods and different percentages of cloud images. We predetermined the percentage of cloud coverage in the time series, selecting and combining two image time series (cloudless and total cloud coverage). Therefore, we chose 11 temporal frames for each region, in which six times the criteria were less than 20% clouds and five times the criteria were more than 75% clouds (see **Figure IV.3**). In addition, each temporal image contained four spectral bands (Red, Green, Blue and near infra-red). Thus, the final stacked image for each region presented a shape with 512(height) × 512(width) × 44(bands).

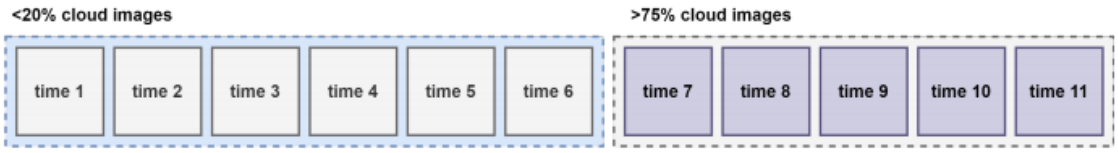

Figure IV.3 Representation of the constructed time series, in which the first six temporal frames (temp) are images with less than 20% of cloud cover and from time 7 to time 11, the images contain more than 75% of cloud cover.

IV.3.3 Annotations and split

Since the main objective of this research is to identify CPIS throughout a specified period, the ground truth elaboration carefully analyzed each temporal frame within the time series. If a CPIS appeared at least once in any of the temporal frames, we annotated it using the ArcGIS software. The basis for the annotations was the vector data of the National Water Agency (ANA), duly corrected considering the visual interpretation. However, Detectron2's Mask-RCNN algorithm requires labels in the COCO annotation format [67], in which each image tile needs a JSON file with the corresponding annotations. Thus, we applied the method used by de Carvalho et al. [17] to convert polygonal GIS data into the instance segmentation annotation format. Each object acquired a unique value from 1 to N, with N being the total number of CPIS.

The software automatically generates a folder with the cropped images and the annotations for each image in the COCO annotation format. We distribute the image tiles in training, validation, and test sets, considering MG/GO area (2018 and 2020) as training data, Western Bahia area of 2020 for validation, and 2018 for testing. We selected 500 points for each MG/GO area image for training, totaling 1000 images. Table IV.2 shows the distribution regarding the number of images and the number of instances in each set.

Table IV-2 Number of images and instances within the training (Train), validation (Val), and testing (Test) sets.

Set	# of images	# of instances
Train	1000	7071
Val 1, 2, 3, 4, 5, and 6	300	2480
Test 1, 2, 3, 4, 5, and 6	300	2480

1) Training images: From each MG/GO region image (2018 and 2020), we selected 500 training samples (totaling 1000 samples). Even though the temporal series presents 11 dates, the input model considered only six dates. In the training procedure we used a novel augmentation technique that selects six temporal events (from the eleven total bands) in a shuffled order, corresponding to an image with the following dimensions: 512 (width) × 512 (height) × 24 (spectral-temporal bands). The selection among six cloudless images and five cloudy images ensured that the training sample had at least one cloudless event, preventing the algorithm from having only cloudy events, which would yield only errors. Furthermore, random selection helps avoid overfitting, and in a practical application, there is no concern with the order of images.

2) Validation and Test images: The test stage used the image of Western Bahia 2018, and the validation stage used Western Bahia 2020. Unlike the training examples in which the order of the images does the shuffling in each iteration, the test and validation examples consider combinations with different percentages of cloud events to assess their influence. Thus, we evaluated the trained model in six configurations with the following cloudless: cloud ratios (1) 6:0; (2) 5:1; (3) 4:2; (4) 3:3; (5) 2:4; and (6) 1:5. Furthermore, we made five random combinations for each selected sampling area to increase the number of the samples and avoid possible bias. In this sense, the selection of the test and validation samples considered 60 areas, resulting in 300 samples with a different ordering.

IV.3.4 Instance segmentation approach

Among the instance segmentation models, the Mask-RCNN is the most common approach. The Mask-RCNN algorithm has three objectives: (a) identify the bounding box for a given object, (b) classify that bounding box according to the object's class, and (c) perform pixel-wise binary segmentation mask on the object. For this reason, the total loss function is given by the sum of the bounding box loss ($Loss_{bbox}$), mask loss ($Loss_{mask}$), and classification loss ($Loss_{class}$): $Loss_{total} = Loss_{mask} + Loss_{class} + Loss_{bbox}$, where $Loss_{mask}$ and $Loss_{class}$ are log loss function, and $Loss_{bbox}$ is L1 loss.

Detectron2 [68] is one of the most efficient instance segmentation frameworks, introduced by the Facebook Artificial Intelligence Research (FAIR), powered by Pytorch. This architecture, usually applied to traditional RGB imagery, requires adjustments to be compatible with the remote sensing data [17]. Hence, we use the Detectron2 software from the Pytorch library with some adaptations to suit our purposes. The software uses some standard settings for traditional DL datasets, such as COCO and Cityscapes. However, for remote sensing images, some changes are necessary for a better adjustment of the models. We need to change the number of input channels on the network (since the most common approach uses only RGB channels). Consequently, the input network increased to 24 channels since the analysis used six temporal events, in which each event contains four channels (red, green, blue, and near-infrared).

1) Model Configurations: To train the Mask-RCNN model, we made the necessary source code changes for compatibility reasons. Since one of our main objectives was to evaluate cloud occlusion, all experiments considered the same backbone structure, the ResNeXt-101-32x8d (X-101) [69]. As augmentation strategies to avoid overfitting, we applied the random choice of temporal images for each iteration, random horizontal flip, and random vertical flip.

Furthermore, this procedure broke the dependence of temporal structures, i.e., the order of images in the temporal structure becomes irrelevant.

Regarding hyperparameters, we applied: (a) Adam optimizer with a learning rate of 0.0005; (b) 256 ROIs per image; (c) thirty thousand iterations; anchor boxes with 16, 32, 64, 128, 256. The other parameters were used as default. We used Nvidia GeForce RTX 2080 TI GPU with 11GB memory to process and train the model.

IV.3.5 Accuracy Analysis

The model evaluation considered the COCO metrics [67] Average Precision (AP), AP50, AP75, APs, APm, and APl. These metrics are the most widely used in instance segmentation problems and have proven to be satisfactory to evaluate different models, including the original Mask-RCNN paper [61] and other influential papers on the subject [70], [71], [72], [73]. The AP is a ranking metric that considers the area under the precision-recall curve. However, the COCO AP also considers ten Intersection over Union thresholds (IoU) (from 0.5 to 0.95 with 0.05 steps). AP50 and AP75 scores consider a fixed threshold of 0.5 (more permissive) and 0.75 (stricter). Moreover, APsmall, APmedium, and APlarge consider the sizes of the different objects, in which small objects have areas of 32^2 or lower, medium objects have areas between 32^2 and 96^2 , and large objects have areas larger than 96^2 .

IV.4 Results

IV.4.1 Cloud Interference and Performance Metrics

Table IV.3 lists the detection (Box) and segmentation (Mask) results with different ratios of cloudless and cloudy images using the X-101 backbone. The main metric (AP) decreases with the increase of cloudy images proportion in the time series for both the bounding box and the mask predictions. The maximum difference between the AP values (6:0 - 1:5) is not expressive, reaching 5.93 for the bounding box and 5.32 for the mask prediction. Moreover, the box and mask results are similar, mainly because of the CPIS round shape, which yields similar IoU results for the boxes and segmentation masks. This result demonstrates the ability of the DL method to detect features even under conditions of little information (low presence of cloudless images) in the time series. The most extensive ranges of variation are between time series with the lowest cloudless image ratio (1:5 and 2:4). In contrast, time series containing high cloudless image rates maintain high values and close to each other. This behavior is

predictable, where the smaller proportion of cloudless images increases the seasonal effect and the probability of not obtaining adequate images to detect center pivots.

Table IV-3 Results for the bounding box and mask predictions on the different test sets with different ratios of cloudless and cloudy images in the time series.

Ratio	Box						Mask					
(cloudless:cloudy)	AP	AP50	AP75	APs	APm	APl	AP	AP50	AP75	APs	APm	APl
6:0	80.10	93.71	91.09	18.43	78.39	86.20	80.21	93.75	90.58	16.91	78.21	86.98
5:1	79.83	92.97	91.08	17.86	78.45	86.06	79.98	93.85	90.56	16.68	78.31	86.59
4:2	79.50	92.83	90.75	17.77	77.95	85.90	79.53	92.94	89.76	16.60	77.63	86.37
3:3	79.12	92.14	90.10	18.51	76.41	85.91	79.20	92.17	89.73	17.43	76.21	86.29
2:4	77.85	91.13	88.14	17.23	75.32	84.45	78.04	91.04	88.05	16.68	74.55	85.24
1:5	74.17	88.26	85.36	14.66	70.57	81.78	74.89	88.20	85.31	14.41	70.17	82.69

The other precision measures (AP50, AP75, APsmall, APmedium, and APlarge) tend to show the same general behavior of decreasing values with an increasing proportion of cloudless images. The only exception was the APm, which had a position inversion between the 6:0 and 5:1 ratios, despite the very close values. This experiment shows scenarios with a very extreme cloud image in the time series, still showing good results.

Among the metrics evaluated, APs had the worst results. The main factor for the poor performance of small objects is that they represent partial forms of CPIS positioned on the edges of the frame, which in the sample cut became incomplete and small. Therefore, the sample edges are more susceptible to detection errors, which can be minimized with the application of the moving window mosaic [17].

Figure IV.4 shows the prediction of the same region with different ratios of cloud presence in the time series. The result demonstrates that even in the most extreme scenarios, with five cloudy images and only one cloudless image, the instance segmentation obtained correct predictions. The modifications identified between the different predictions concentrated on minor variations in the center pivot design. Besides, there are inaccuracies in detecting a small part of a center pivot cut in the left corner of the third alignment of the CPISs. As the proportion of clouds increases, the small slice of a center pivot disappears.

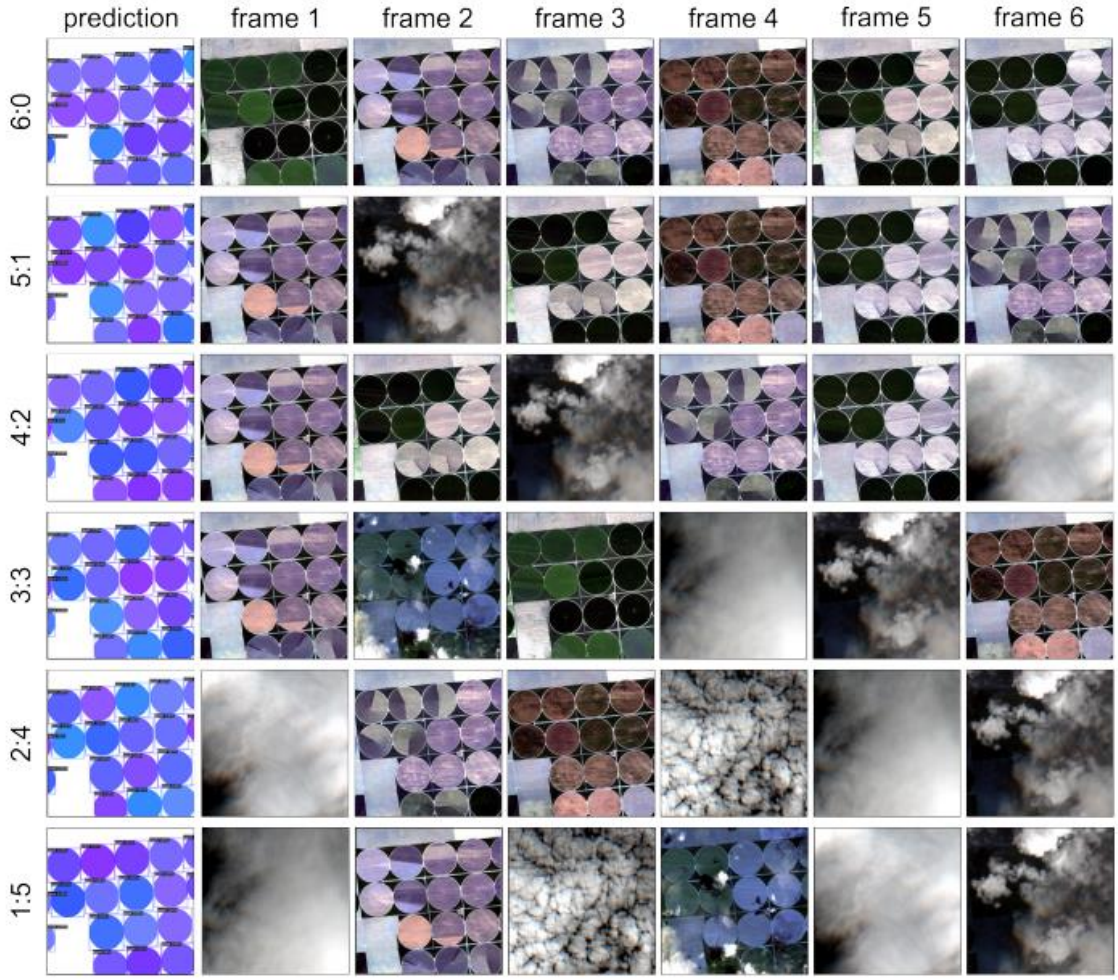

Figure IV.4 Representation of the predictions of a given region using the different ratios of cloud presence, in which each bounding box with the segmentation mask represent a different instance of center pivots.

IV.4.2 Seasonal interference

Eventually, the CPIS patterns fades with the surrounding areas, and detection is not possible. The use of multitemporal images guarantees the acquisition of data in the different planting stages that evidence the presence of CPIS. **Figure IV.5** presents nine examples containing instance segmentation results and the color compositions of the six temporal images used as input.

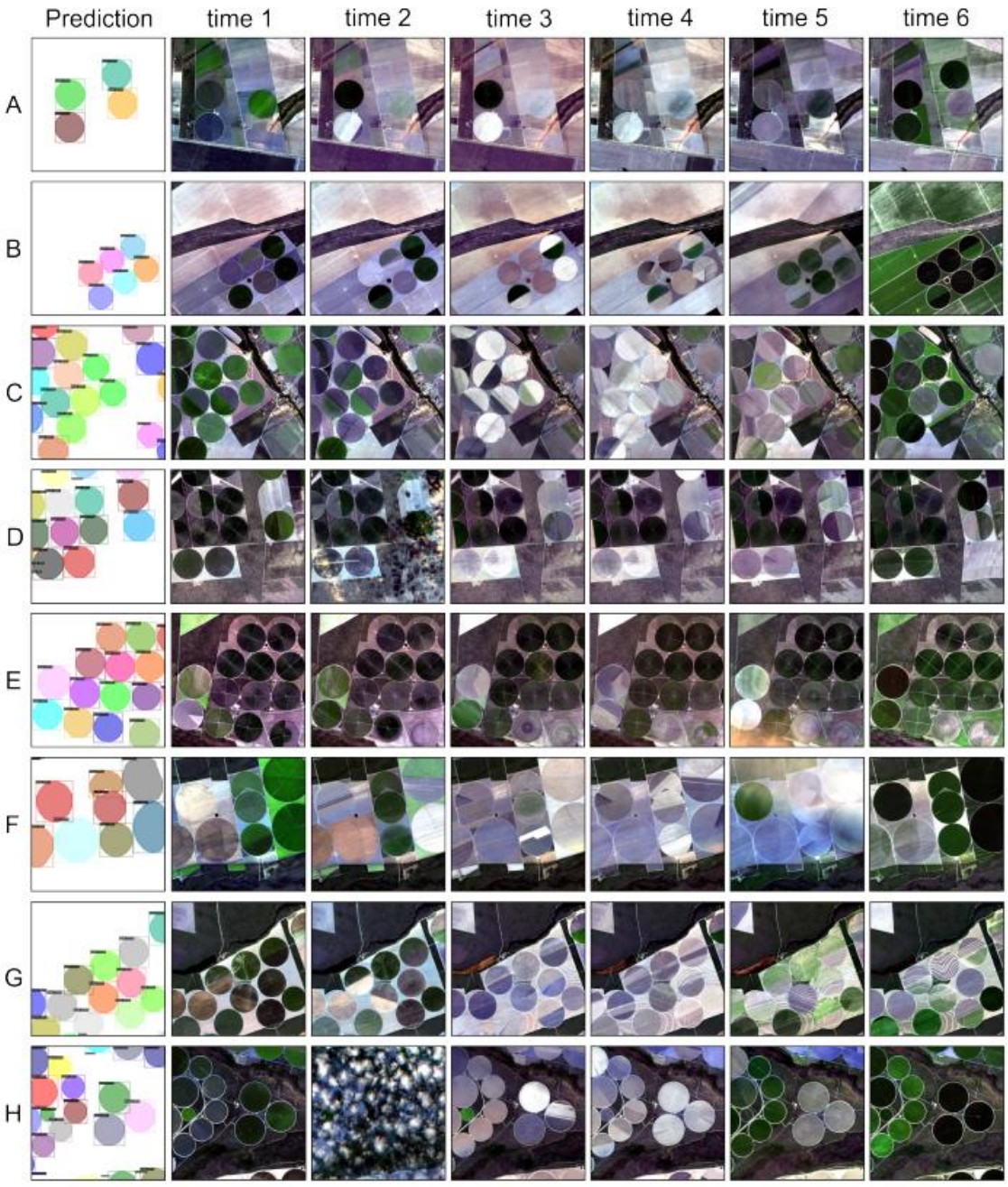

Figure IV.5 Representation of nine predictions and their respective cloudless (< 20% cloud cover) time series. Note that even with this percentage, there is still a chance of having cloudy frames, as shown in F and H.

The Sentinel-2 images correspond to images with a percentage of clouds below 25%. This condition would be a viable criterion to compose the six multitemporal images, allowing to obtain a vast predominance of free-cloud images, different phases of the planting cycle, and a viable set for automation with good precision. The temporal sequence demonstrates that some center pivots practically disappear in specific periods, becoming very similar to their surroundings, making their detection very difficult even by visual interpretation. A clear

example is the images of row A, where some images (frames 1-2-3) are visible only three center pivots, despite the existence of 4 CPIS as evidenced by the last image (frame 6). The other images present CPIS with behavior like the background in a certain period.

Therefore, the different behaviors of CPIS over time make it difficult to generalize a DL model to a single date. The model with multitemporal data allows high generalizability and a precise classification, even in cases where the CPIS becomes imperceptible or in the presence of clouds in a temporal interval.

IV.5 Discussion

All DL models applied to optical imaging for center pivot detection reported training and applications for single-time imaging [47], [20], [57], [18], [58], [59], [17]. The main problems from only one date are clouds and visualizing the center pivot in particular planting stages. De Albuquerque et al. [18] showed that there are periods of the year that are easier to identify CPIS due to seasonal changes. According to the authors, the end of the drought and rainy seasons in Central Brazil present more significant difficulties. The best period is the onset of drought when the natural environment has non-photosynthetically active vegetation, and the irrigated pivots have photosynthetically active vegetation.

Therefore, a viable solution to overcome the problems described is developing DL models adapted to a set of temporal images. Recently, a study using Sentinel-1 radar images used DL models of time series to detect center pivots [62]. Although radar data is free from cloud interference, research has shown that increasing the number of images has improved instance segmentation accuracy.

This multitemporal approach with DL algorithms allows a more generalized learning that captures the uniform shape of the center pivot, disregarding the images with the presence of clouds and variations in the plantations. Furthermore, the model presents efficiency independent of the temporal order of the images. This approach of looking for an invariant shape over a period differs from studies that distinguish the types of crops that depend on the phenological cycle, and the chronological sequence [74], [75]. In this context, we developed a new strategy to increase the number of samples and reduce the chances of overfitting, randomly selecting the order of images in the time series. Training and evaluation considered different cloud proportions and the image ordering allows for a greater flexibility in data acquisition and automation.

The proposed methodology represents a robust alternative to the CPIS surveys carried out by the Brazilian government based on the visual interpretation of images [15], [16]. The procedure has significant advantages in terms of speed and consideration of multitemporal images, not limited to a specific date. Furthermore, the present DL approach with multitemporal optical images can be effectively applied to other objects with a fixed format within a time interval of interest, such as buildings and solar panels.

IV.6 Conclusion

The present study proposed a new DL approach for CPIS detection using time series, including different cloud occlusion scenarios and seasonal behavior, problems of great interest in the study of optical images. Unlike single-date data, multitemporal data offers more opportunities to observe center pivots by overcoming optical imaging issues such as cloud cover, atmospheric effects, shadow, missing data, and lack of contrast to surrounding vegetation. In addition, time-series satellite images reduce ambiguities arising from the phenological stage and the spatial boundary of the CPIS.

We proposed a new augmentation strategy for time series analysis in which we randomly select images from the time series, introducing different percentages of cloudy images. The procedure forces the neural network to learn with the presence of images containing atmospheric interference and spectral similarity between the center pivot and the surrounding areas. However, this procedure only applies to objects that present similar structures over time, as is the case with CPIS.

Predictably, we found that results were better when using a time series with images with a low cloud presence. Nonetheless, results kept steady even in more extreme scenarios, demonstrating a good generalization capability. Furthermore, this approach to targets with spectral variation over time within a fixed shape favors the generalization of the model, as it captures different scenarios of the same object and increases the predictive power. The results show an excellent perspective for practical application, obtaining good results from six images without a rigorous selection for better detection. The algorithm returns a very precise classification result. This model favors automation of CPIS detection with cost savings, agility and avoids large consumption of labor.

References

1. Godfray, H. C. J., Beddington, J. R., Crute, I. R., Haddad, L., Lawrence, D., Muir, J. F., Pretty, J., Robinson, S., Thomas, S. M., & Toulmin, C. (2010). Food Security: The Challenge of Feeding 9 Billion People. *Science*, *327*(5967), 812–818. https://doi.org/10.1126/science.1185383

2. Prosekov, A. Y., & Ivanova, S. A. (2018). Food security: The challenge of the present. *Geoforum*, *91*, 73–77. https://doi.org/10.1016/j.geoforum.2018.02.030

3. Beltran-Pea, A., Rosa, L., & D'Odorico, P. (2020). Global food self-sufficiency in the 21st century under sustainable intensification of agriculture. *Environmental Research Letters*, *15*(9). https://doi.org/10.1088/1748-9326/ab9388

4. Foley, J. A., Ramankutty, N., Brauman, K. A., Cassidy, E. S., Gerber, J. S., Johnston, M., Mueller, N. D., O'Connell, C., Ray, D. K., West, P. C., Balzer, C., Bennett, E. M., Carpenter, S. R., Hill, J., Monfreda, C., Polasky, S., Rockström, J., Sheehan, J., Siebert, S., Zaks, D. P. M. (2011). Solutions for a cultivated planet. *Nature*, *478*(7369), 337–342. https://doi.org/10.1038/nature10452

5. Kopittke, P. M., Menzies, N. W., Wang, P., McKenna, B. A., & Lombi, E. (2019). Soil and the intensification of agriculture for global food security. *Environment International*, *132*, 105078. https://doi.org/10.1016/j.envint.2019.105078

6. Yang, G., He, X. L., Li, X. L., Long, A. H., & Xue, L. Q. (2017). Transformation of surface water and groundwater and water balance in the agricultural irrigation area of the Manas River Basin, China. *International Journal of Agricultural and Biological Engineering*, *10*(4), 107–118. https://doi.org/10.25165/j.ijabe.20171004.3461

7. Essaid, H. I., & Caldwell, R. R. (2017). Evaluating the impact of irrigation on surface water – groundwater interaction and stream temperature in an agricultural watershed. *Science of The Total Environment*, *599–600*, 581–596. https://doi.org/10.1016/j.scitotenv.2017.04.205

8. Wang, Z., Fan, B., & Guo, L. (2019). Soil salinization after long-term mulched drip irrigation poses a potential risk to agricultural sustainability. *European Journal of Soil Science*, *70*(1), 20–24. https://doi.org/10.1111/ejss.12742

9. Tomaz, A., Palma, P., Fialho, S., Lima, A., Alvarenga, P., Potes, M., Costa, M. J., & Salgado,

R. (2020). Risk Assessment of Irrigation-Related Soil Salinization and Sodification in Mediterranean Areas. *Water*, *12*(12), 3569. https://doi.org/10.3390/w12123569

10. R. Sojka. (2018). “Understanding and managing irrigation-induced erosion,” in Advances in soil and water conservation. *Routledge*, 2018, pp. 21–37.

11. Abu-Hashim, M., Sayed, A., Zelenakova, M., Vranayová, Z., & Khalil, M. (2021). Soil Water Erosion Vulnerability and Suitability under Different Irrigation Systems Using Parametric Approach and GIS, Ismailia, Egypt. *Sustainability*, *13*(3), 1057. https://doi.org/10.3390/su13031057

12. Zhang, Q., Zhang, Z., Shi, P., Singh, V. P., & Gu, X. (2018). Evaluation of ecological instream flow considering hydrological alterations in the Yellow River basin, China. *Global and Planetary Change*, *160*, 61–74. https://doi.org/10.1016/j.gloplacha.2017.11.012

13. Althoff, D., & Rodrigues, L. N. (2019). The expansion of center-pivot irrigation in the cerrado biome. *Irriga*, *1*(1InovagriSpecialEdition), 56–61. https://doi.org/10.15809/irriga.2019v1n1p56-61

14. Silva, L. M. D. C., & Da Hora, M. D. A. G. M. (2014). conflito pelo uso da água na bacia hidrográfica do rio São Marcos: o estudo de caso da UHE Batalha. *Engevista*, *17*(2), 166. https://doi.org/10.22409/engevista.v17i2.633

15. Agência Nacional de Águas (ANA). (2016). Levantamento da agricultura irrigada por pivôs centrais no Brasil – 2014: *Relatório Síntese*, Agência Nacional de Águas (ANA), Ed., Brasília, Brasil.

16. Agência Nacional de Águas (ANA). (2019). Levantamento da agricultura irrigada por pivôs centrais no Brasil (1985-2017).: Agência Nacional de Águas (ANA), Brasília, Brasil.

17. Carvalho, O. L. F. de, de Carvalho Júnior, O. A., Albuquerque, A. O. de, Bem, P. P. de, Silva, C. R., Ferreira, P. H. G., Moura, R. dos S. de, Gomes, R. A. T., Guimarães, R. F., & Borges, D. L. (2020). Instance Segmentation for Large, Multi-Channel Remote Sensing Imagery Using Mask-RCNN and a Mosaicking Approach. *Remote Sensing*, *13*(1), 39. https://doi.org/10.3390/rs13010039

18. de Albuquerque, A. O., de Carvalho Júnior, O. A., Carvalho, O. L. F. de, de Bem, P. P., Ferreira, P. H. G., de Moura, R. dos S., Silva, C. R., Trancoso Gomes, R. A., & Fontes Guimarães, R. (2020). Deep Semantic Segmentation of Center Pivot Irrigation Systems

from Remotely Sensed Data. *Remote Sensing*, *12*(13), 2159. https://doi.org/10.3390/rs12132159

19. J. Tang, D. Arvor, T. Corpetti, and P. Tang. (2020). "Pvanet-hough: Detection and location of center pivot irrigation systems from sentinel-2 images," ISPRS Annals of Photogrammetry, *Remote Sensing and Spatial Information Sciences,* vol. 3, pp. 559–564.

20. Tang, J., Zhang, Z., Zhao, L., & Tang, P. (2021). Increasing Shape Bias to Improve the Precision of Center Pivot Irrigation System Detection. *Remote Sensing*, *13*(4), 612. https://doi.org/10.3390/rs13040612

21. Liu, W., Wang, Z., Liu, X., Zeng, N., Liu, Y., & Alsaadi, F. E. (2017). A survey of deep neural network architectures and their applications. *Neurocomputing*, *234*, 11–26. https://doi.org/10.1016/j.neucom.2016.12.038

22. Liu, L., Ouyang, W., Wang, X., Fieguth, P., Chen, J., Liu, X., & Pietikäinen, M. (2020). Deep Learning for Generic Object Detection: A Survey. *International Journal of Computer Vision*, *128*(2), 261–318. https://doi.org/10.1007/s11263-019-01247-4

23. Cheng, G., Xie, X., Han, J., Guo, L., & Xia, G.-S. (2020). Remote Sensing Image Scene Classification Meets Deep Learning: Challenges, Methods, Benchmarks, and Opportunities. *IEEE Journal of Selected Topics in Applied Earth Observations and Remote Sensing*, *13*, 3735–3756. https://doi.org/10.1109/JSTARS.2020.3005403

24. Ball, J. E., Anderson, D. T., & Chan, C. S. (2017). Comprehensive survey of deep learning in remote sensing: theories, tools, and challenges for the community. *Journal of Applied Remote Sensing*, *11*(04), 1. https://doi.org/10.1117/1.JRS.11.042609

25. Hoeser, T., Bachofer, F., & Kuenzer, C. (2020). Object Detection and Image Segmentation with Deep Learning on Earth Observation Data: A Review—Part II: Applications. *Remote Sensing*, *12*(18), 3053. https://doi.org/10.3390/rs12183053

26. Khelifi, L., & Mignotte, M. (2020). Deep Learning for Change Detection in Remote Sensing Images: Comprehensive Review and Meta-Analysis. *IEEE Access*, *8*, 126385–126400. https://doi.org/10.1109/ACCESS.2020.3008036

27. Li, Y., Zhang, H., Xue, X., Jiang, Y., & Shen, Q. (2018). Deep learning for remote sensing image classification: A survey. *WIREs Data Mining and Knowledge Discovery*, *8*(6). https://doi.org/10.1002/widm.1264

28. Ma, L., Liu, Y., Zhang, X., Ye, Y., Yin, G., & Johnson, B. A. (2019). Deep learning in remote

sensing applications: A meta-analysis and review. *ISPRS Journal of Photogrammetry and Remote Sensing*, *152*, 166–177. https://doi.org/10.1016/j.isprsjprs.2019.04.015

29. Zhang, L., Zhang, L., & Du, B. (2016). Deep Learning for Remote Sensing Data: A Technical Tutorial on the State of the Art. *IEEE Geoscience and Remote Sensing Magazine*, *4*(2), 22–40. https://doi.org/10.1109/MGRS.2016.2540798

30. Yuan, Q., Shen, H., Li, T., Li, Z., Li, S., Jiang, Y., Xu, H., Tan, W., Yang, Q., Wang, J., Gao, J., & Zhang, L. (2020). Deep learning in environmental remote sensing: Achievements and challenges. *Remote Sensing of Environment*, *241*, 111716. https://doi.org/10.1016/j.rse.2020.111716

31. Li, J., Huang, X., & Gong, J. (2019). Deep neural network for remote-sensing image interpretation: status and perspectives. *National Science Review*, *6*(6), 1082–1086. https://doi.org/10.1093/nsr/nwz058

32. Paoletti, M. E., Haut, J. M., Plaza, J., & Plaza, A. (2019). Deep learning classifiers for hyperspectral imaging: A review. *ISPRS Journal of Photogrammetry and Remote Sensing*, *158*, 279–317. https://doi.org/10.1016/j.isprsjprs.2019.09.006

33. Parikh, H., Patel, S., & Patel, V. (2020). Classification of SAR and PolSAR images using deep learning: a review. *International Journal of Image and Data Fusion*, *11*(1), 1–32. https://doi.org/10.1080/19479832.2019.1655489

34. Signoroni, A., Savardi, M., Baronio, A., & Benini, S. (2019). Deep Learning Meets Hyperspectral Image Analysis: A Multidisciplinary Review. *Journal of Imaging*, *5*(5), 52. https://doi.org/10.3390/jimaging5050052

35. Vali, A., Comai, S., & Matteucci, M. (2020). Deep Learning for Land Use and Land Cover Classification Based on Hyperspectral and Multispectral Earth Observation Data: A Review. *Remote Sensing*, *12*(15), 2495. https://doi.org/10.3390/rs12152495

36. Zhu, X. X., Tuia, D., Mou, L., Xia, G.-S., Zhang, L., Xu, F., & Fraundorfer, F. (2017). Deep Learning in Remote Sensing: A Comprehensive Review and List of Resources. *IEEE Geoscience and Remote Sensing Magazine*, *5*(4), 8–36. https://doi.org/10.1109/MGRS.2017.2762307

37. de Bem, P. P., de Carvalho Júnior, O. A., de Carvalho, O. L. F., Gomes, R. A. T., & Fontes Guimarães, R. (2020). Performance Analysis of Deep Convolutional Autoencoders with Different Patch Sizes for Change Detection from Burnt Areas. *Remote Sensing*, *12*(16),

2576. https://doi.org/10.3390/rs12162576

38. Yi, Y., Zhang, Z., Zhang, W., Zhang, C., Li, W., & Zhao, T. (2019). Semantic Segmentation of Urban Buildings from VHR Remote Sensing Imagery Using a Deep Convolutional Neural Network. *Remote Sensing*, *11*(15), 1774. https://doi.org/10.3390/rs11151774

39. Ozdogan, M., Yang, Y., Allez, G., & Cervantes, C. (2010). Remote Sensing of Irrigated Agriculture: Opportunities and Challenges. *Remote Sensing*, *2*(9), 2274–2304. https://doi.org/10.3390/rs2092274

40. Heller, R. C., & Johnson, K. A. (1979). Estimating irrigated land acreage from Landsat imagery. *Photogrammetric Engineering and Remote Sensing*, *45*(10), 1379–1386.

41. M. P. Carlson. (1989).“The nebraska center-pivot inventory: An example of operational satellite remote sensing on a long-term basis,” Photogramm. Eng. Remote Sens, vol. 55, pp. 587–590.

42. Demarqui, E. N., & Demarqui, L. M. B. (2020). Análise espaço-temporal da ocorrência de sistemas de irrigação por pivô central em regiões agrícolas no Estado de Mato Grosso. *Nativa*, *8*(3), 344–351. https://doi.org/10.31413/nativa.v8i4.8931

43. Ferreira, E., Toledo, J. H. D. E., Dantas, A. A. A., & Pereira, R. M. (2011). Cadastral Maps of Irrigated Areas By Center Pivots in the State of. *Engenharia Agrícola*, *31*(4), 771–780.

44. Martins, J. D., Bohrz, I. S., Tura, E. F., Fredrich, M., Veronez, R. P., & Kunz, G. A. (2018). Levantamento da área irrigada por pivô central no Estado do Rio Grande do sul. *IRRIGA*, *21*(2), 300. https://doi.org/10.15809/irriga.2016v21n2p300-311

45. Wenger, K., Vadjunec, J., & Fagin, T. (2017). Groundwater Governance and the Growth of Center Pivot Irrigation in Cimarron County, OK and Union County, NM: Implications for Community Vulnerability to Drought. *Water*, *9*(1), 39. https://doi.org/10.3390/w9010039

46. Rodrigues, M. L., Korting, T. S., de Queiroz, G. R., Sales, C. P., & Silva, L. A. R. da. (2020). Detecting Center Pivots In MATOPIBA Using Hough Transform And Web Time Series Service. *2020 IEEE Latin American GRSS & ISPRS Remote Sensing Conference (LAGIRS)*, 189–194. https://doi.org/10.1109/LAGIRS48042.2020.9165648

47. Zhang, C., Yue, P., Di, L., & Wu, Z. (2018). Automatic Identification of Center Pivot Irrigation Systems from Landsat Images Using Convolutional Neural Networks. *Agriculture*, *8*(10), 147. https://doi.org/10.3390/agriculture8100147

48. Blaschke, T. (2010). Object based image analysis for remote sensing. *ISPRS Journal of*

Photogrammetry and Remote Sensing, *65*(1), 2–16. https://doi.org/10.1016/j.isprsjprs.2009.06.004

49. Hossain, M. D., & Chen, D. (2019). Segmentation for Object-Based Image Analysis (OBIA): A review of algorithms and challenges from remote sensing perspective. *ISPRS Journal of Photogrammetry and Remote Sensing*, *150*, 115–134. https://doi.org/10.1016/j.isprsjprs.2019.02.009

50. Ye, S., Pontius, R. G., & Rakshit, R. (2018). A review of accuracy assessment for object-based image analysis: From per-pixel to per-polygon approaches. *ISPRS Journal of Photogrammetry and Remote Sensing*, *141*, 137–147. https://doi.org/10.1016/j.isprsjprs.2018.04.002

51. Johansen, K., Lopez, O., Tu, Y.-H., Li, T., & McCabe, M. F. (2021). Center pivot field delineation and mapping: A satellite-driven object-based image analysis approach for national scale accounting. *ISPRS Journal of Photogrammetry and Remote Sensing*, *175*, 1–19. https://doi.org/10.1016/j.isprsjprs.2021.02.019

52. Yan, L., & Roy, D. P. (2014). Automated crop field extraction from multi-temporal Web Enabled Landsat Data. *Remote Sensing of Environment*, *144*, 42–64. https://doi.org/10.1016/j.rse.2014.01.006

53. Watkins, B., & van Niekerk, A. (2019). A comparison of object-based image analysis approaches for field boundary delineation using multi-temporal Sentinel-2 imagery. *Computers and Electronics in Agriculture*, *158*, 294–302. https://doi.org/10.1016/j.compag.2019.02.009

54. Guirado, E., Tabik, S., Alcaraz-Segura, D., Cabello, J., & Herrera, F. (2017). Deep-learning Versus OBIA for Scattered Shrub Detection with Google Earth Imagery: Ziziphus lotus as Case Study. *Remote Sensing*, *9*(12), 1220. https://doi.org/10.3390/rs9121220

55. Huang, H., Lan, Y., Yang, A., Zhang, Y., Wen, S., & Deng, J. (2020). Deep learning versus Object-based Image Analysis (OBIA) in weed mapping of UAV imagery. *International Journal of Remote Sensing*, *41*(9), 3446–3479. https://doi.org/10.1080/01431161.2019.1706112

6. Liu, T., Abd-Elrahman, A., Morton, J., & Wilhelm, V. L. (2018). Comparing fully convolutional networks, random forest, support vector machine, and patch-based deep convolutional neural networks for object-based wetland mapping using images from

small unmanned aircraft system. *GIScience & Remote Sensing*, *55*(2), 243–264. https://doi.org/10.1080/15481603.2018.1426091

57. Tang, J., Arvor, D., Corpetti, T., & Tang, P. (2021). Mapping Center Pivot Irrigation Systems in the Southern Amazon from Sentinel-2 Images. *Water*, *13*(3), 298. https://doi.org/10.3390/w13030298

58. Saraiva, M., Protas, É., Salgado, M., & Souza, C. (2020). Automatic Mapping of Center Pivot Irrigation Systems from Satellite Images Using Deep Learning. *Remote Sensing*, *12*(3), 558. https://doi.org/10.3390/rs12030558

59. Graf, L., Bach, H., & Tiede, D. (2020). Semantic Segmentation of Sentinel-2 Imagery for Mapping Irrigation Center Pivots. *Remote Sensing*, *12*(23), 3937. https://doi.org/10.3390/rs12233937

60. Li, Y., Qi, H., Dai, J., Ji, X., & Wei, Y. (2017). Fully convolutional instance-aware semantic segmentation. *Proceedings - 30th IEEE Conference on Computer Vision and Pattern Recognition, CVPR 2017*, *2017-January*, 4438–4446. https://doi.org/10.1109/CVPR.2017.472

61. K. He, G. Gkioxari, P. Dollar, and R. Girshick. (2020). "Mask R-CNN," IEEE Transactions on Pattern Analysis and Machine Intelligence, vol. 42, no. 2, pp. 386–397.

62. de Albuquerque, A. O., de Carvalho, O. L. F., e Silva, C. R., de Bem, P. P., Trancoso Gomes, R. A., Borges, D. L., Guimarães, R. F., Pimentel, C. M. M., & de Carvalho Júnior, O. A. (2021). Instance segmentation of center pivot irrigation systems using multi-temporal Sentinel-1 SAR images. *Remote Sensing Applications: Society and Environment*, *23*, 100537. https://doi.org/10.1016/j.rsase.2021.100537

63. de Oliveira, S. N., de Carvalho Júnior, O. A., Gomes, R. A. T., Guimarães, R. F., & McManus, C. M. (2017). Landscape-fragmentation change due to recent agricultural expansion in the Brazilian Savanna, Western Bahia, Brazil. *Regional Environmental Change*, *17*(2), 411–423. https://doi.org/10.1007/s10113-016-0960-0

64. Nunes de Oliveira, S., Abílio de Carvalho Júnior, O., Trancoso Gomes, R. A., Fontes Guimarães, R., & McManus, C. M. (2017). Deforestation analysis in protected areas and scenario simulation for structural corridors in the agricultural frontier of Western Bahia, Brazil. *Land Use Policy*, *61*, 40–52. https://doi.org/10.1016/j.landusepol.2016.10.046

65. Pousa, R., Costa, M. H., Pimenta, F. M., Fontes, V. C., Brito, V. F. A. de, & Castro, M.

(2019). Climate Change and Intense Irrigation Growth in Western Bahia, Brazil: The Urgent Need for Hydroclimatic Monitoring. *Water*, *11*(5), 933. https://doi.org/10.3390/w11050933

66. Drusch, M., Del Bello, U., Carlier, S., Colin, O., Fernandez, V., Gascon, F., Hoersch, B., Isola, C., Laberinti, P., Martimort, P., Meygret, A., Spoto, F., Sy, O., Marchese, F., & Bargellini, P. (2012). Sentinel-2: ESA's Optical High-Resolution Mission for GMES Operational Services. *Remote Sensing of Environment*, *120*, 25–36. https://doi.org/10.1016/j.rse.2011.11.026

67. Y. Wu, A. Kirillov, F. Massa, W.-Y. Lo, and R. Girshick. (2019) "Detectron2," https://github.com/facebookresearch/detectron2.

68. T.-Y. Lin, M. Maire, S. Belongie, J. Hays, P. Perona, D. Ramanan, P. Dollar, and C. L. Zitnick. (2014) "Microsoft COCO: Common objects in context," in European conference on computer vision. Springer, pp. 740–755

69. Bolya, D., & Lee, Y. J., "Yolact: Real-time instance segmentation," in *Proceedings of the IEEE/CVF International Conference on Computer Vision*, 2019, pp. 9157–9166.

70. Bolya, D., Zhou, C., Xiao, F., & Lee, Y. J. (2022). Yolact++ Better Real-Time Instance Segmentation. *IEEE Transactions on Pattern Analysis and Machine Intelligence*, *44*(2), 1108–1121. https://doi.org/10.1109/TPAMI.2020.3014297

71. Cai, Z., & Vasconcelos, N. (2018). Cascade R-CNN: Delving into High Quality Object Detection. *Proceedings of the IEEE Computer Society Conference on Computer Vision and Pattern Recognition*, 6154–6162. https://doi.org/10.1109/CVPR.2018.00644

72. Su, H., Wei, S., Liu, S., Liang, J., Wang, C., Shi, J., & Zhang, X. (2020). HQ-ISNet: High-Quality Instance Segmentation for Remote Sensing Imagery. *Remote Sensing*, *12*(6), 989. https://doi.org/10.3390/rs12060989

73. Zhong, L., Hu, L., & Zhou, H. (2019). Deep learning based multi-temporal crop classification. *Remote Sensing of Environment*, *221*, 430–443. https://doi.org/10.1016/j.rse.2018.11.032

74. Crisóstomo de Castro Filho, H., Abílio de Carvalho Júnior, O., Ferreira de Carvalho, O. L., Pozzobon de Bem, P., dos Santos de Moura, R., Olino de Albuquerque, A., Rosa Silva, C., Guimarães Ferreira, P. H., Fontes Guimarães, R., & Trancoso Gomes, R. A. (2020). Rice Crop Detection Using LSTM, Bi-LSTM, and Machine Learning Models from

Sentinel-1 Time Series. *Remote Sensing*, *12*(16), 2655. https://doi.org/10.3390/rs12162655

CAPÍTULO

V. CONCLUSÕES

O presente trabalho obteve êxito no objetivo proposto inicialmente, de aplicar técnicas de inteligência artificial para identificação de sistemas de irrigação por pivô central em dados de sensoriamento remoto. Os métodos utilizados apresentaram grande potencial de detecção dos alvos com um elevado grau de assertividade. A utilização de diferentes áreas para treinamento, teste e validação permitiu analisar o comportamento dos modelos de *Deep Learning* qualitativamente.

A análise de precisão da pesquisa desenvolvida no segundo capítulo apresentou alto desempenho nas três arquiteturas CNN's utilizadas, e apesar de ligeira vantagem da *U-Net*, todas apresentaram altos valores de métricas. Adicionalmente, a reconstrução do mosaico através de janelas deslizantes minimizou erros que normalmente ocorrem nas bordas dos quadros e comprometem a qualidade do resultado da classificação. Esse procedimento mostrou-se eficaz em imagens de grandes áreas, uma vez que a ela precisa ser dividida em quadros menores para entrada nas arquiteturas CNN's e posteriormente existe a necessidade de voltar ao tamanho original.

O capítulo 3 apresentou diferenças metodológicas em relação ao anterior, com o uso de imagens multitemporais de radar de abertura sintética e segmentação de instâncias através de uma arquitetura CNN distinta, o Mask R-CNN. Além das dificuldades relacionadas a presença de nuvens nas imagens ópticas, ausentes nas imagens de radar, ficou evidenciado as vantagens em estudos com séries temporais, uma vez que a precisão aumentou em mais de 10%, em relação ao uso de apenas uma imagem em comparação ao uso de toda a série temporal. Além disso, foi observado que o comportamento dos pivôs ao longo dos meses apresenta grande variação, isso foi notado mesmo em intervalo menor que quatro meses, em que o pivô era detectado em apenas um dos tempos, seja no início ou no final, e o uso de séries temporais acarretam em melhorias de desempenho nesse sentido.

Em seguida, no quarto capítulo, os resultados demonstraram que o aumento de séries temporais de imagens ópticas, mesmo com presença de alto percentuais de nuvens, torna o aprendizado profundo mais eficiente, aumentando o poder preditivo das CNN. Além disso, as análises realizadas demonstraram que a utilização de dados multitemporais permite superar problemas de nuvens, sombras, efeitos atmosféricos, dados ausentes e falta de contraste com as

vegetações do entorno dos SIPC.

Considerando as metodologias utilizadas no presente estudo para aplicação prática do método, conclui-se que a identificação dos pivôs centrais utilizando interpretação visual e classificação manual das feições, pode ser substituída pelo método automático, o que torna o trabalho mais rápido e eficiente. Em geral, as técnicas aplicadas necessitam de grandes processamentos, no entanto, analisar previamente os dados a serem utilizados são determinantes para o bom desempenho das redes, como análise do tamanho da área de pesquisa, periodicidade e tipo do sensor, resolução espacial e espectral das imagens. A exemplo disso, no terceiro capítulo, os resultados obtidos utilizando apenas uma polarização (VV) das imagens radar, foram próximos aos resultados da combinação das duas polarizações (VV+VH), que teve tempo de processamento e consumo computacional muito superior.

O presente trabalho baseou-se na aplicação dos modelos em três áreas com grande concentração de pivôs centrais, porém, em trabalhos futuros, a metodologia pode ser aplicada em grandes áreas, em nível regional ou mesmo nacional. Trabalhos futuros no sentido de identificar o tipo de cultivo dentro do pivô são desafiadores, mas se mostram como de grande utilidade pro gestor público, a metodologia utilizada no presente trabalho poderia ser aplicada, com amostras rotuladas do tipo de cultivo daquele pivô central, fazendo com que a rede neural além de classificar o pivô central, identifique o tipo de cultivo do seu interior.